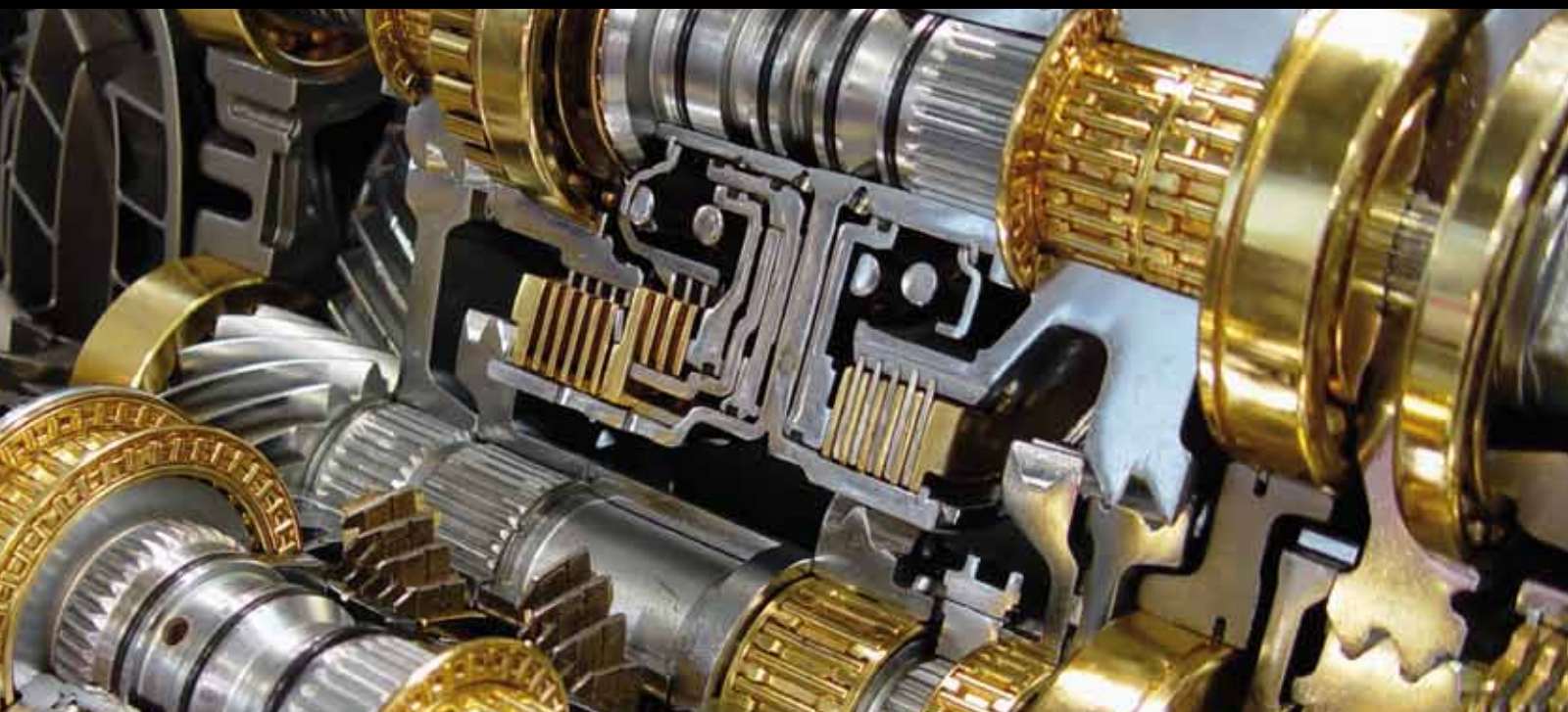


LOWER-MOBILITY PARALLEL ROBOTS: THEORY AND APPLICATIONS

GUEST EDITORS: ZHEN HUANG, FENGFENG (JEFF) XI, TIAN HUANG,
JIAN SHENG DAI, AND ROSARIO SINATRA





Lower-Mobility Parallel Robots: Theory and Applications

Advances in Mechanical Engineering

Lower-Mobility Parallel Robots: Theory and Applications

Guest Editors: Zhen Huang, Fengfeng (Jeff) Xi, Tian Huang, Jian Shang Dai, and Rosario Sinatra



Copyright © 2010 Hindawi Publishing Corporation. All rights reserved.

This is a special issue published in volume 2010 of "Advances in Mechanical Engineering." All articles are open access articles distributed under the Creative Commons Attribution License, which permits unrestricted use, distribution, and reproduction in any medium, provided the original work is properly cited.

Editorial Board

Koshi Adachi, Japan
Mehdi Ahmadian, USA
Rehan Ahmed, UK
Malcolm J. Andrews, USA
Claude Bathias, France
Adib Becker, UK
Leonardo Bertini, Italy
Liam Blunt, UK
Marco Ceccarelli, Italy
Hyung Hee Cho, South Korea
Seung Bok Choi, South Korea
Bijan K. Dutta, India
Bogdan I. Epureanu, USA
Mohammad Reza Eslami, Iran
Amir Faghri, USA
Ali Fatemi, USA
Siegfried Fouvry, France
Ian A. Frigaard, Canada
Mike Ian Friswell, UK
Yuebin Guo, USA
Zhen Huang, China

Thomas H. Hyde, UK
Jiin-Yuh Jang, Taiwan
Zhongmin Jin, UK
Essam Eldin Khalil, Egypt
Xianwen Kong, UK
Chungxiang Li, China
Jaw-Ren Lin, Taiwan
Cheng-Xian Lin, USA
Oronzio Manca, Italy
Aristide F. Massardo, Italy
Kim Choon Ng, Singapore
Cong Tam Nguyen, Canada
Hiroshi Noguchi, Japan
Andrew Ooi, Australia
Hakan F. Oztop, Turkey
Duc Pham, UK
Homer Rahnejat, UK
Subhash Rakheja, Canada
John E. Renaud, USA
Robert L. Reuben, UK
Bidyut Baran Saha, Singapore

Kazuhiro Saitou, USA
Dik J. Schipper, The Netherlands
Steven R. Schmid, USA
A. Seshadri Sekhar, India
A. A. Shabana, USA
C. S. Shin, Taiwan
Yung C. Shin, USA
Ray W. Snidle, UK
Christian Soize, France
Margaret Stack, UK
Neil Stephen, UK
Kumar K. Tamma, USA
Cho W. Solomon To, USA
Yoshihiro Tomita, Japan
Shandong Tu, China
Moran Wang, USA
Fengfeng (Jeff) Xi, Canada
Hiroshi Yabuno, Japan
Wei M. Yan, Taiwan
Byeng Youn, USA
Zhongrong Zhou, China

Contents

Lower-Mobility Parallel Robots: Theory and Applications, Zhen Huang, Fengfeng (Jeff) Xi, Tian Huang, Jian Sheng Dai, and Rosario Sinatra
Volume 2010, Article ID 927930, 1 page

Kinematic Design of a Translational Parallel Manipulator with Fine Adjustment of Platform Orientation, Masataka Tanabe and Yukio Takeda
Volume 2010, Article ID 485358, 9 pages

Optimal Design and Development of a Decoupled A/B-Axis Tool Head with Parallel Kinematics, Fugui Xie, Xin-Jun Liu, Li-Ping Wang, and Jinsong Wang
Volume 2010, Article ID 474602, 14 pages

Modeling of Configuration-Dependent Flexible Joints for a Parallel Robot, Zili Zhou, Chris K. Mechefske, and Fengfeng Xi
Volume 2010, Article ID 143961, 12 pages

Kinetostatic and Inertial Conditioning of the McGill Schönflies-Motion Generator, Alessandro Cammarata, Jorge Angeles, and Rosario Sinatra
Volume 2010, Article ID 186203, 9 pages

Kinetostatic Analysis of 4-R(CRR) Parallel Manipulator with Overconstraints via Reciprocal-Screw Theory, Zhen Huang, Yan Zhao, and Jingfang Liu
Volume 2010, Article ID 404960, 11 pages

A Compliant PKM Mesomanipulator: Kinematic and Dynamic Analyses, C. Amici, A. Borboni, and R. Faglia
Volume 2010, Article ID 706023, 9 pages

Application of the Rotation Matrix Natural Invariants to Impedance Control of Rotational Parallel Robots, L. Bruzzone and M. Callegari
Volume 2010, Article ID 284976, 9 pages

Editorial

Lower-Mobility Parallel Robots: Theory and Applications

Zhen Huang,¹ Fengfeng (Jeff) Xi,² Tian Huang,³ Jian Sheng Dai,⁴ and Rosario Sinatra⁵

¹ Robotics Research Center, Yanshan University, Qinhuangdao, Hebei 066004, China

² Department of Aerospace Engineering, Ryerson University, Toronto, ON, Canada M5B 2K3

³ School of Mechanical Engineering, Tianjin University, Tianjin 300072, China

⁴ King's College London, University of London, London WC2R 2LS, UK

⁵ Dipartimento di Ingegneria Industriale e Meccanica, Università di Catania, 95125 Catania, Italy

Correspondence should be addressed to Zhen Huang, huangz@ysu.edu.cn

Received 23 December 2009; Accepted 23 December 2009

Copyright © 2010 Zhen Huang et al. This is an open access article distributed under the Creative Commons Attribution License, which permits unrestricted use, distribution, and reproduction in any medium, provided the original work is properly cited.

In the past decades, parallel mechanisms (PMs) have attracted a lot of attention from the academic and industrial communities. Compared with the more commonly used serial manipulators, the parallel one has attractive advantages in accuracy, rigidity, capacity, and load-to-weight ratio.

In recent years, the research and application have evolved from general six-DOF PMs to lower-mobility PMs. The essential reason is that lower-mobility PMs have similar applications to general six-DOF PMs, while they are much simpler in structure and cheaper in cost. The research of lower-mobility PMs has become new hot point. A great deal of research on lower-mobility PM has been carried out all over the world, and a large number of new mechanisms, such as Delta, Tricept, medical robots, and microrobots, have been built for various applications.

This book opens a window to view the current research and development situation on lower-mobility PMs contributed by international researchers. The book consists of seven papers introducing both basic research and advanced developments. Covered topics include kinematics, dynamic analysis, optimization design, modeling, simulation, and control, and the development of some new special applications. The new algorithms and methods presented in the contributions are very effective for solving general problems in design and analysis of parallel robots.

Finally, I would like to express our deep acknowledgments to all of the authors for their contributions to this book.

*Zhen Huang
Fengfeng (Jeff) Xi
Tian Haung
Jian Sheng Dai
Rosario Sinatra*

Research Article

Kinematic Design of a Translational Parallel Manipulator with Fine Adjustment of Platform Orientation

Masataka Tanabe and Yukio Takeda

Department of Mechanical Sciences and Engineering, Tokyo Institute of Technology, 2-12-1, O-okayama, Meguro-ku, Tokyo 152-8552, Japan

Correspondence should be addressed to Yukio Takeda, takeda@mech.titech.ac.jp

Received 27 March 2009; Revised 7 August 2009; Accepted 15 September 2009

Academic Editor: Jian Sheng Dai

Copyright © 2010 M. Tanabe and Y. Takeda. This is an open access article distributed under the Creative Commons Attribution License, which permits unrestricted use, distribution, and reproduction in any medium, provided the original work is properly cited.

We present a kinematic design of a translational parallel manipulator with fine adjustment capability of platform orientation. In order to clarify possible kinematic structures for it, structural synthesis of fully decoupled mechanism and partially decoupled mechanism both with six degrees of freedom (dof) was carried out based on the synthesis results of translational and rotational parallel mechanisms with three dof. All possible kinematic structures were obtained. Of these, one partially decoupled mechanism was selected and a kinematic design of a prototype manipulator was done. Its characteristics in terms of workspace, singularity, orientation adjustment capability, and coupling characteristics between translational and rotational displacement were discussed with experimental results regarding fine adjustment capability of platform orientation.

1. Introduction

A parallel manipulator that has three degrees of freedom (dof) and outputs translational motion without changing its orientation is called a “translational parallel manipulator.” A translational parallel manipulator has potential for use in assembly, machining, and coordinate measurements. The manipulator is composed of a base, platform, and multiple connecting chains arranged in parallel between the base and platform.

Many researchers in recent years have shown interest in translational parallel manipulators and mechanisms. The kinematic conditions for the connecting chain to obtain translational motion of the platform have been investigated [1, 2]. Various kinematic structures for translational parallel manipulators have also been investigated [3, 4]. Further, optimization taking into consideration the manipulator’s workspace has been done [5–7]. Translational parallel mechanisms have been applied to medical robots [8] and micromanipulators [9].

The errors in the output pose of a manipulator caused by dimensional errors, such as these in links, can be classified

into two groups. The first group contains errors that can be compensated for by calibration or full closed-loop control. Such errors are called “compensatable errors” [10, 11]. The tolerance requirements with respect to these compensatable errors depend on calibration or the performance of the controller, and these are not usually severe. The second group contains errors that cannot be compensated for by any means, either during or prior to manipulation. Such errors are called “uncompensatable errors” [10, 11]. They depend on kinematic structures and parameters and tolerances. In designing and controlling a lower-dof parallel manipulator, such as a translational parallel manipulator, engineers must take uncompensatable error into consideration. For example, if there is a dimensional error in a link of a connecting chain of a translational parallel manipulator, the platform changes its orientation according to motion (Figure 1), and this orientation error cannot be compensated for by the input of active joints. One approach to this is to minimize uncompensatable error by determining the optimal values of kinematic constants at the design stage [11], taking tolerances into account. Another approach is to change the structure of the mechanism so that fine adjustments can be added

to the output motion to eliminate the uncompensatable error.

Taking the uncompensatable error of a translational parallel manipulator into consideration, a spatial parallel mechanism with six dof, such as a Stewart platform, can be considered as an alternative mechanism to it. However, it needs six actuators of the same capacity in operation throughout the motion though the main output motion requires three dof. Such a composition of a mechanism is inefficient from the view point of facility and energy. In order to solve such a problem, while the uncompensatable error can be compensated, a concept of mechanism structure, which has three actuators to generate the translational motion as the main output motion and three actuators to compensate for the orientation error, is proposed. Since three actuators for compensating for orientation error operate only when accurate output orientation is required, they consume less energy than the actuators do in a spatial parallel mechanism with six dof. And, since displacement and power required to these actuators for compensating for orientation error are relatively small, they can be compact, light, and inexpensive. In the present paper, following this concept, kinematic design of a translational parallel manipulator with fine adjustment capability of platform orientation (TPMFAO) is discussed. Section 2 describes the basic concept underlying the structural synthesis of TPMFAO. Sections 3 and 4 briefly review the kinematic structures for translational and rotational parallel manipulators with three dof. Section 5 discusses the derivations for the kinematic structures of TPMFAO. Section 6 discusses the design of a prototype TPMFAO and its orientation adjustment capability with theoretical and experimental results. Section 7 summarizes the conclusions.

2. Basic Concept for Structural Synthesis of Translational Parallel Manipulator with Fine Adjustment Capability of Platform Orientation

2.1. Condition of Mechanism Structure. A manipulator must have six degrees of freedom (dof) to achieve fine adjustments of the platform orientation with gross translational motion. We considered the following conditions in the structural synthesis of TPMFAO for its real applications.

- (1) It has three connecting chains.
- (2) Each connecting chain has the same structure. The joints in a connecting chain are numbered 1, 2, . . . , 6 from the base.
- (3) Revolute and prismatic joints are used to compose a connecting chain. Other joints such as a cylindrical joint are constructed by combining revolute and prismatic joints.
- (4) Each connecting chain has two active joints. One active joint is to correspond to the translational motion, as the main output motion, of the platform. These active joints are called main active joints. The other active joint in each connecting chain

is to generate rotational motion of the platform. These joints are used to make fine adjustments to the platform's orientation. These joints are called subactive joints.

- (5) The main active joints are located at the first or second joints, while any location for the subactive joints is acceptable.

Since actuators are heavy compared with links and joints, it is better to locate active joints as close to the base as possible. Since subactive joints may be constructed compact and light due to their small displacement and power, condition (5) was taken into account in our study.

If the motion of the platform generated by the subactive joints is pure rotational motion around a specific point on the platform, this mechanism is called a "fully decoupled mechanism." If this motion is rotational motion with coupled translational motion, this mechanism is called a "partially decoupled mechanism." These mechanisms are considered as the candidates for TPMFAO.

We can find many studies [12–19] on fully and partially decoupled parallel manipulators and mechanisms. Structural synthesis of partially decoupled parallel mechanism with six connecting chains has been done [18]. A procedure of structural synthesis of fully decoupled parallel manipulator, in which three connecting chains are used and active joints are located at only the first and second joints, has been presented and a kinematic design of a fully decoupled manipulator has been discussed [19]. Even though these studies were helpful in our study, all possible kinematic structures that satisfy the five conditions have not yet been clarified.

2.2. Fully Decoupled Mechanism. The main active joints in a fully decoupled mechanism generate translational motion of the platform while subactive joints generate pure rotational motion around a specific point on the platform (Figure 2). Then, the relationship between infinitesimal input displacement ($\Delta \mathbf{q}_M$: infinitesimal displacement vector of the main active joints; $\Delta \mathbf{q}_S$: infinitesimal displacement vector of the subactive joints) and infinitesimal output displacement ($\Delta \mathbf{P} = [\Delta \Theta^T \ \Delta \mathbf{p}^T]^T$, $\Delta \Theta$: infinitesimal angular displacement vector; $\Delta \mathbf{p}$: infinitesimal displacement vector) at any platform pose can be written in the following form:

$$\Delta \mathbf{P} = \begin{bmatrix} \Delta \Theta \\ \Delta \mathbf{p} \end{bmatrix} = J_{FD} \begin{bmatrix} \Delta \mathbf{q}_M \\ \Delta \mathbf{q}_S \end{bmatrix}, \quad J_{FD} = \begin{bmatrix} 0_3 & B_{FD} \\ A_{FD} & 0_3 \end{bmatrix}. \quad (1)$$

Here, J_{FD} is the 6×6 Jacobian matrix, A_{FD} and B_{FD} are 3×3 matrices, and 0_3 is the 3×3 zero matrix.

2.3. Partially Decoupled Mechanism. The main active joints in a partially decoupled mechanism generate translational motion of the platform while subactive joints generate rotational motion with coupled translational motion (Figure 3).

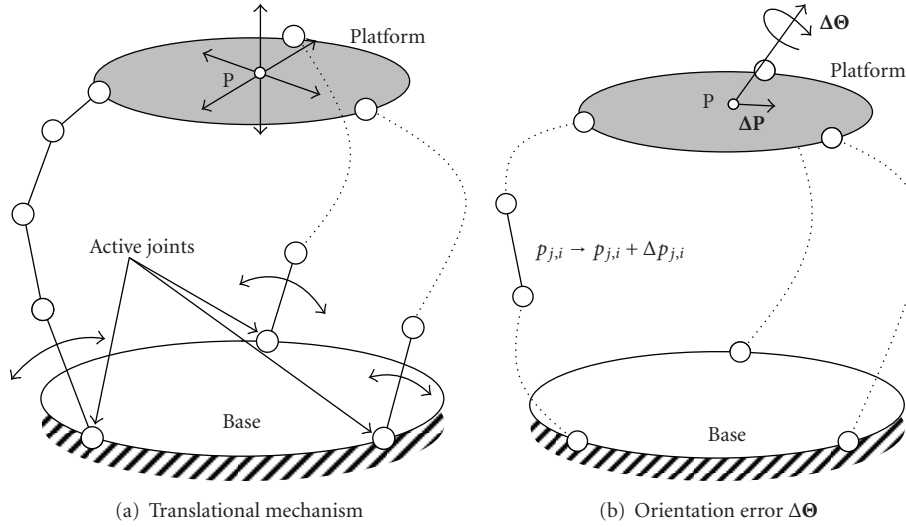


FIGURE 1: Translational parallel mechanism and its orientation error.

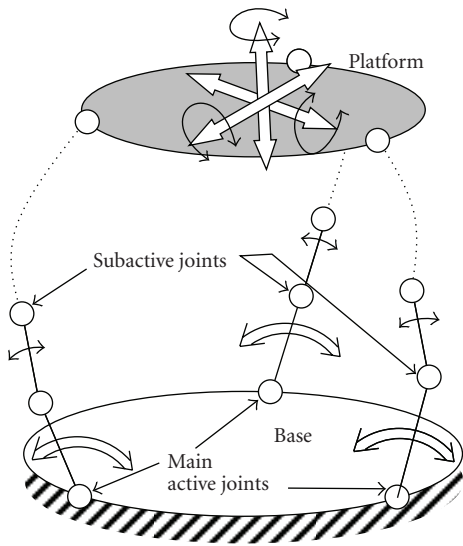


FIGURE 2: Fully decoupled parallel mechanism.

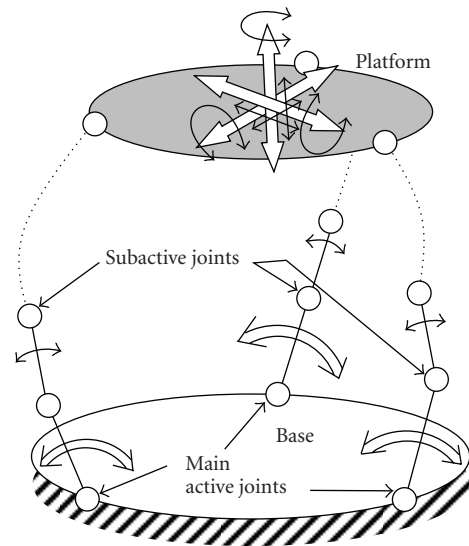


FIGURE 3: Partially decoupled parallel mechanism.

Then, the Jacobian matrix of a partially decoupled mechanism at any platform pose can be written in the following form:

$$J_{PD} = \begin{bmatrix} 0_3 & B_{PD} \\ A_{PD} & C_{PD} \end{bmatrix}. \quad (2)$$

In the above discussions on the characteristics of fully and partially decoupled mechanisms, the first-order derivatives of the relationship between the input and output displacements were used. Though such a first-order approximation of the displacement characteristics is effective to clarify the motion characteristics of a mechanism, there exist small errors between the displacements obtained by the first-order model and the real mechanism due to the effect of the second-order and higher-order terms. Therefore, in

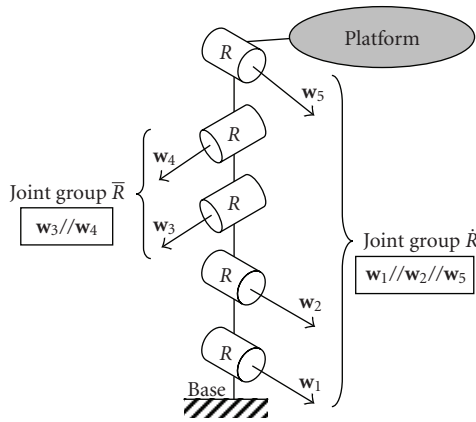
order to eliminate the uncompensatable error of a lower-dof mechanism, iterative compensation should be applied if the first-order model is used.

3. Structures for Translational Parallel Mechanism

The structures for translational parallel mechanism with three dof are shown taking into consideration the conditions for TPMFAO. Referring to a previous study [2], the structures for translational parallel mechanism with three connecting chains, each with five single-dof joints, are listed in Table 1. R and P correspond to revolute and prismatic joints. In these mechanisms, all revolute joints belong to either of two groups. Revolute-joint axes belonging to the

TABLE 1: Kinematic structures for translational parallel mechanism.

Classes	Types of connecting chains			
5R	$\dot{R}\dot{R}\dot{R}\dot{R}\dot{R}$	$\dot{R}\dot{R}\dot{R}\dot{R}\bar{R}$	$\bar{R}\bar{R}\bar{R}\bar{R}\bar{R}$	
4R1P	$\dot{R}\dot{R}\dot{R}\dot{R}P$	$\dot{R}\dot{R}\dot{R}P\bar{R}$	$\dot{R}\dot{R}P\bar{R}\bar{R}$	$\bar{R}\bar{R}\bar{R}\bar{R}P$
	$\bar{R}\bar{R}\bar{R}\bar{R}P$	$\bar{R}\bar{R}P\dot{R}\bar{R}$	$\dot{R}\dot{R}\dot{R}\dot{R}P$	$\dot{R}\dot{R}\dot{R}P\bar{R}$
	$\dot{R}\dot{R}P\dot{R}\bar{R}$	$\dot{R}P\dot{R}\dot{R}\bar{R}$	$P\dot{R}\dot{R}\dot{R}\bar{R}$	$\dot{R}\dot{R}\dot{R}\dot{R}P$
	$\dot{R}\dot{R}P\bar{R}\dot{R}$	$\dot{R}\dot{R}P\bar{R}\bar{R}$	$\dot{R}P\bar{R}\dot{R}\bar{R}$	$P\dot{R}\dot{R}\dot{R}\bar{R}$
3R2P	$\dot{R}\dot{R}\dot{R}PP$	$\dot{R}\dot{R}P\bar{R}P$	$\dot{R}P\bar{R}\dot{R}P$	$P\dot{R}\dot{R}\dot{R}P$
	$\dot{R}\dot{R}PP\bar{R}$	$\dot{R}P\bar{R}P\bar{R}$	$P\dot{R}\dot{R}P\bar{R}$	$\dot{R}PP\dot{R}\bar{R}$
	$P\dot{R}P\bar{R}\bar{R}$	$PP\dot{R}\bar{R}\bar{R}$	$\bar{R}\bar{R}\dot{R}PP$	$\dot{R}\bar{R}P\dot{R}P$
	$\dot{R}P\bar{R}\dot{R}P$	$P\bar{R}\bar{R}\dot{R}P$	$\bar{R}\bar{R}PP\dot{R}$	$\dot{R}P\bar{R}P\dot{R}$
2R3P	$\bar{R}\bar{R}PPP$	$\dot{R}P\bar{R}PP$	$P\dot{R}\bar{R}PP$	$\dot{R}PPP\bar{R}$
	$P\dot{R}P\bar{R}P$	$PP\dot{R}\bar{R}P$	$\dot{R}PPP\bar{R}$	

FIGURE 4: $\dot{R}\dot{R}\dot{R}\dot{R}\dot{R}$ connecting chain for translational mechanism.

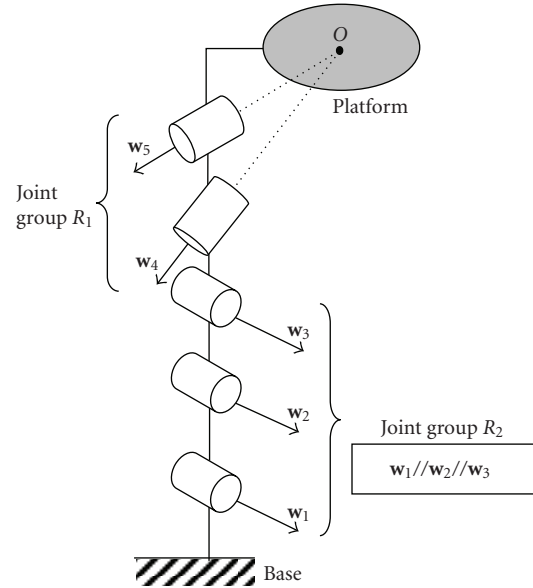
same group have the same direction. To represent the group of revolute joints with their axes in the same direction, dots and bars are used as \dot{R} and \bar{R} , as shown in Figure 4. The type of connecting chain includes the order of the joints as well as the combination of joints. Either of the joints in the left or right sides connects with the base.

4. Structures for Rotational Parallel Mechanism

The structures for pure rotational parallel mechanism with three dof are shown in this section. Referring to previous studies [20, 21], the structures for pure rotational parallel mechanism with three connecting chains, each with five single-dof joints, are listed in Table 2. In these mechanisms, all revolute joints belong to either of two groups. The axes of the revolute joints belonging to the first group pass through the center of rotation of the platform. The axes of the other revolute joints belonging to the second group are parallel and do not pass through the center of rotation. R_1 and R_2 are used to represent the joint groups of the revolute joints (R_1 : the first group; R_2 : the second group). And, the axes of the prismatic joints are perpendicular to those of the revolute joints in the second group. An example of connecting chain is shown in Figure 5, in which the revolute joint belonging to the second group connects with the base.

TABLE 2: Kinematic structures for pure rotational parallel mechanism.

Classes	Types of connecting chains		
5R	$R_2R_2R_1R_1R_1$	$R_2R_1R_2R_1R_1$	$R_2R_1R_1R_2R_1$
	$R_2R_1R_1R_1R_2$	$R_1R_2R_2R_1R_1$	$R_2R_2R_2R_1R_1$
	$R_1R_2R_2R_2R_1$		
4R1P	$PR_2R_1R_1R_1$	$R_2PR_1R_1R_1$	$R_2R_1PR_1R_1$
	$R_2R_1R_1PR_1$	$R_2R_1R_1R_1P$	$PR_1R_2R_1R_1$
	$PR_1R_1R_2R_1$	$R_1PR_2R_1R_1$	$R_1R_2PR_1R_1$
	$R_1R_2R_1PR_1$	$R_1R_2R_1R_1P$	$PR_2R_2R_1R_1$
	$R_2PR_2R_1R_1$	$R_2R_2PR_1R_1$	$R_1PR_2R_2R_1$
3R2P	$R_1R_2PR_2R_1$		
	$PPR_1R_1R_1$	$PR_1PR_1R_1$	$PR_1R_1PR_1$
	$PR_1R_1R_1P$	$R_1PPR_1R_1$	$R_1PR_1PR_1$
	$R_1PR_1R_1P$	$PPR_2R_1R_1$	$PR_2PR_1R_1$
	$R_2PPR_1R_1$	$R_1PPR_2R_1$	$R_1PR_2PR_1$

FIGURE 5: $R_2R_2R_2R_1R_1$ connecting chain for rotational mechanism.

5. Structural Synthesis of Translational Parallel Manipulator with Fine Adjustment of Platform Orientation

This section discusses the kinematic structures for fully and partially decoupled mechanisms for TPMFAO that can be derived from the kinematic structures of translational and pure rotational parallel mechanisms presented in the preceding sections.

5.1. Fully Decoupled Mechanism. The kinematic structures of fully decoupled mechanism can be clarified by adding a revolute or prismatic joint to the mechanisms listed in Tables 1 and 2. To accomplish fully decoupled motion, each

connecting chain should become

- (1) a chain for a translational parallel mechanism when the subactive joints are locked at any position,
- (2) a chain for a pure rotational parallel mechanism when the main active joints are locked at any position.

The conditions for a chain to generate translational motion and pure rotational motion are as follows.

- (1) Conditions for generating translational motion.
 - (i) Number of joints in a connecting chain is five.
 - (ii) The axis directions of revolute joints are two.
 - (iii) Number of revolute joints of the same axis direction is fewer than four.
 - (iv) Number of prismatic joints is fewer than four.
- (2) Conditions for generating pure rotational motion.
 - (i) All revolute joints belong to either of two groups mentioned in Section 4.
 - (ii) Number of revolute joints belonging to a group is fewer than four.
 - (iii) Number of revolute joints belonging to the first group is more than one.
 - (iv) Prismatic joints are perpendicular to the revolute joints belonging to the second group.
 - (v) Number of prismatic joints is fewer than three.

The kinematic structures that satisfy these conditions are listed in Table 3. Here, a joint with subscript “ma” represents a joint that must be a main active joint, and a joint with subscript “sa” represents a joint that must be a subactive joint. The prismatic joints denoted by \bar{P} and \tilde{P} are perpendicular to the revolute joint denoted by R_2 while the prismatic joints denoted by \dot{P} are not perpendicular to R_2 . The mechanisms listed in Table 3 were obtained, as a result, by adding a prismatic joint to the pure-rotational parallel mechanisms in Table 2. Then, we considered the following conditions to specify the main active joint and/or the subactive joint in each connecting chain.

- (1) The additional prismatic joint must be the main active joint.
- (2) In the case where there are more than one revolute joints belonging to the second group (R_2) in a connecting chain, they must passively move according to the motion of the prismatic joints used as the main active joints (\dot{P}_{ma}) in the other two connecting chains so that the kinematic condition for fully decoupled mechanism might be satisfied. Therefore, one of the revolute joints other than those belonging to the second group must be the subactive joint if there are more than one R_2 joints in each connecting chain.

An $R_2\dot{P}_{ma}\bar{P}\tilde{P}R_1R_1$ chain is shown in Figure 6 as an example.

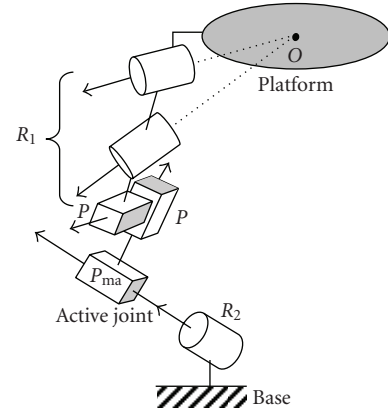


FIGURE 6: $R_2\dot{P}_{ma}\bar{P}\tilde{P}R_1R_1$ connecting chain for fully decoupled parallel mechanism.

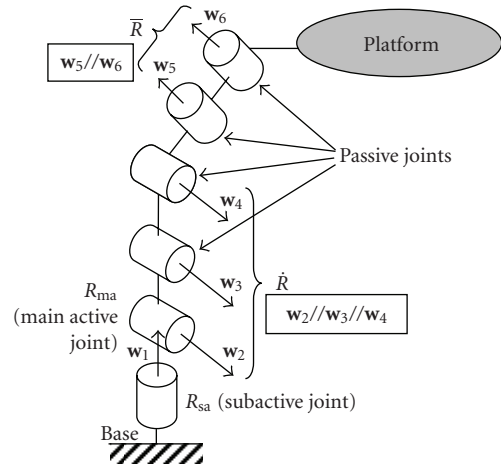


FIGURE 7: $R_{sa}\dot{R}\dot{R}\dot{R}\dot{R}\dot{R}$ connecting chain for partially decoupled parallel mechanism.

5.2. *Partially Decoupled Mechanism.* The structures for partially decoupled mechanism can be derived by adding a joint to those of translational parallel mechanism listed in Table 1 so that the following conditions are satisfied.

- (1) The conditions for translational parallel mechanism still hold even when an additional joint is at any position.
- (2) Only a revolute joint is added to the connecting chain to enable the platform to rotate.

The results are summarized in Table 4. In all mechanisms listed in this table, the additional revolute joint must be the subactive joint of each connecting chain. An $R_{sa}\dot{R}\dot{R}\dot{R}\dot{R}\dot{R}$ chain is shown in Figure 7 as an example.

6. Kinematic Design of Prototype Manipulator

This section discusses the kinematic design of a TPMFAO taking the partially decoupled parallel mechanism with $R_{sa}\dot{R}\dot{R}\dot{R}\dot{R}\dot{R}$ chains because this mechanism is composed of

TABLE 3: Kinematic structures for fully decoupled mechanism.

Classes	Types of connecting chains					
5R1P	$\dot{P}_{ma}R_2R_2R_2R_{1sa}R_1$	$R_2\dot{P}_{ma}R_2R_2R_{1sa}R_1$	$\dot{P}_{ma}R_2R_2R_2R_1R_{1sa}$	$R_2\dot{P}_{ma}R_2R_2R_1R_{1sa}$		
4R2P	$\dot{P}_{ma}\overline{P}R_2R_2R_{1sa}R_1$	$\overline{P}\dot{P}_{ma}R_2R_2R_{1sa}R_1$	$\dot{P}_{ma}R_2\overline{P}R_2R_{1sa}R_1$	$R_2\dot{P}_{ma}\overline{P}R_2R_{1sa}R_1$	$\dot{P}_{ma}R_2R_2\overline{P}R_{1sa}R_1$	$R_2\dot{P}_{ma}R_2\overline{P}R_{1sa}R_1$
	$\dot{P}_{ma}\overline{P}R_2R_2R_1R_{1sa}$	$\overline{P}\dot{P}_{ma}R_2R_2R_1R_{1sa}$	$\dot{P}_{ma}R_2\overline{P}R_2R_1R_{1sa}$	$R_2\dot{P}_{ma}\overline{P}R_2R_1R_{1sa}$	$\dot{P}_{ma}R_2R_2\overline{P}R_1R_{1sa}$	$R_2\dot{P}_{ma}R_2\overline{P}R_1R_{1sa}$
3R3P	$\dot{P}_{ma}\overline{P}\overline{P}R_2R_1R_1$	$\overline{P}\dot{P}_{ma}\overline{P}R_2R_1R_1$	$\dot{P}_{ma}\overline{P}R_2\overline{P}R_1R_1$	$\overline{P}\dot{P}_{ma}R_2\overline{P}R_1R_1$	$\dot{P}_{ma}R_2\overline{P}\overline{P}R_1R_1$	$R_2\dot{P}_{ma}\overline{P}\overline{P}R_1R_1$
	$PPPR_1R_1R_1$					

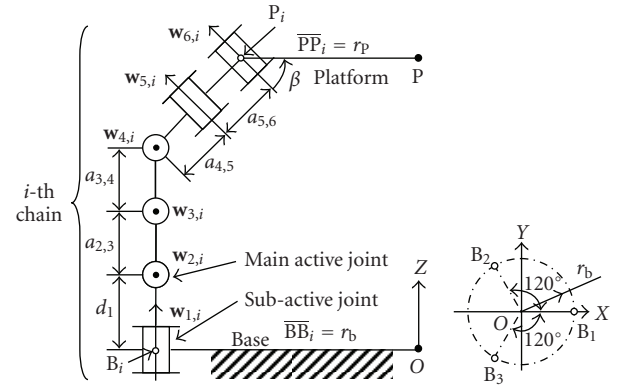
TABLE 4: Kinematic structures for partially decoupled mechanism.

Classes	Types of connecting chains							
6R	$R_{sa}\dot{R}\dot{R}\dot{R}\dot{R}\dot{R}$	$\dot{R}\dot{R}\dot{R}\dot{R}_{sa}\dot{R}\dot{R}$	$\dot{R}\dot{R}\dot{R}\dot{R}\dot{R}_{sa}$					
	$R_{sa}\dot{R}\dot{R}\dot{R}\dot{R}\dot{P}$	$\dot{R}\dot{R}\dot{R}_{sa}\dot{R}\dot{R}\dot{P}$	$\dot{R}\dot{R}\dot{R}\dot{R}_{sa}\dot{P}$	$\dot{R}\dot{R}\dot{R}\dot{R}\dot{P}_{sa}$	$\dot{R}\dot{R}\dot{R}_{sa}\dot{P}\dot{R}$	$\dot{R}\dot{R}\dot{R}\dot{P}\dot{R}_{sa}$	$R_{sa}\dot{R}\dot{R}\dot{P}\dot{R}$	$\dot{R}\dot{R}\dot{R}_{sa}\dot{P}\dot{R}$
5R1P	$\dot{R}\dot{R}\dot{P}R_{sa}\dot{R}\dot{R}$	$\dot{R}\dot{R}\dot{P}\dot{R}_{sa}\dot{R}\dot{R}$	$R_{sa}\dot{R}\dot{R}\dot{R}\dot{P}$	$\dot{R}\dot{R}\dot{R}_{sa}\dot{R}\dot{P}$	$\dot{R}\dot{R}\dot{R}_{sa}\dot{P}$	$\dot{R}\dot{R}\dot{R}\dot{P}_{sa}$	$R_{sa}\dot{R}\dot{R}\dot{P}\dot{R}$	$\dot{R}\dot{R}\dot{R}_{sa}\dot{P}\dot{R}$
	$\dot{R}\dot{R}\dot{P}R_{sa}\dot{R}$	$\dot{R}\dot{R}\dot{P}\dot{R}_{sa}\dot{R}$	$R_{sa}\dot{R}\dot{R}\dot{P}\dot{R}$	$\dot{R}\dot{R}\dot{P}\dot{R}_{sa}\dot{R}$	$\dot{R}\dot{R}\dot{P}\dot{R}_{sa}$	$R_{sa}\dot{R}\dot{P}\dot{R}\dot{R}$	$\dot{R}\dot{P}\dot{R}\dot{R}_{sa}\dot{R}$	$\dot{R}\dot{P}\dot{R}\dot{R}_{sa}$
	$R_{sa}\dot{P}\dot{R}\dot{R}\dot{R}$	$\dot{P}R_{sa}\dot{R}\dot{R}\dot{R}$	$\dot{P}\dot{R}\dot{R}\dot{R}_{sa}\dot{R}$	$\dot{P}\dot{R}\dot{R}\dot{R}_{sa}$				
	$R_{sa}\dot{R}\dot{R}\dot{P}\dot{P}$	$\dot{R}\dot{R}_{sa}\dot{R}\dot{P}\dot{P}$	$\dot{R}\dot{R}\dot{R}_{sa}\dot{P}\dot{P}$	$\dot{R}\dot{R}\dot{P}\dot{P}_{sa}$	$\dot{R}\dot{R}\dot{P}\dot{P}_{sa}$	$R_{sa}\dot{R}\dot{P}\dot{P}\dot{R}$	$\dot{R}\dot{R}_{sa}\dot{P}\dot{P}\dot{R}$	$\dot{R}\dot{R}\dot{P}\dot{P}_{sa}\dot{R}$
	$\dot{R}\dot{R}\dot{P}\dot{P}_{sa}\dot{P}$	$\dot{R}\dot{P}\dot{P}\dot{R}_{sa}\dot{P}$	$R_{sa}\dot{R}\dot{P}\dot{P}\dot{R}$	$\dot{R}\dot{P}\dot{P}_{sa}\dot{R}\dot{P}$	$\dot{R}\dot{P}\dot{P}_{sa}\dot{P}$	$\dot{R}\dot{P}\dot{P}_{sa}\dot{R}$	$R_{sa}\dot{P}\dot{R}\dot{R}\dot{P}$	$\dot{P}R_{sa}\dot{R}\dot{R}\dot{P}$
4R2P	$\dot{P}\dot{R}\dot{R}_{sa}\dot{R}\dot{P}$	$\dot{P}\dot{R}\dot{R}\dot{R}_{sa}\dot{P}$	$\dot{P}\dot{R}\dot{R}\dot{P}_{sa}\dot{R}$	$R_{sa}\dot{R}\dot{P}\dot{P}\dot{R}$	$\dot{R}\dot{R}_{sa}\dot{P}\dot{P}\dot{R}$	$\dot{R}\dot{R}\dot{P}_{sa}\dot{P}\dot{R}$	$\dot{R}\dot{R}\dot{P}\dot{P}_{sa}\dot{R}$	$\dot{R}\dot{R}\dot{P}\dot{P}_{sa}$
	$R_{sa}\dot{R}\dot{P}\dot{P}\dot{R}$	$\dot{R}\dot{P}\dot{P}_{sa}\dot{R}$	$\dot{R}\dot{P}\dot{P}_{sa}\dot{R}$	$\dot{R}\dot{P}\dot{P}_{sa}$	$R_{sa}\dot{P}\dot{R}\dot{P}\dot{R}$	$\dot{P}R_{sa}\dot{R}\dot{P}\dot{R}$	$\dot{P}\dot{R}\dot{R}_{sa}\dot{P}\dot{R}$	$\dot{P}\dot{R}\dot{P}\dot{R}_{sa}$
	$\dot{P}\dot{R}\dot{R}\dot{P}_{sa}\dot{R}$	$R_{sa}\dot{R}\dot{P}\dot{P}\dot{R}$	$\dot{R}\dot{P}\dot{P}_{sa}\dot{R}$	$\dot{R}\dot{P}\dot{P}_{sa}$	$R_{sa}\dot{P}\dot{R}\dot{P}\dot{R}$	$\dot{P}R_{sa}\dot{R}\dot{P}\dot{R}$	$\dot{P}\dot{R}\dot{R}_{sa}\dot{P}\dot{R}$	$\dot{P}\dot{R}\dot{P}\dot{R}_{sa}$
	$R_{sa}\dot{P}\dot{P}\dot{R}\dot{R}$	$\dot{P}R_{sa}\dot{P}\dot{R}\dot{R}$	$\dot{P}\dot{P}\dot{R}_{sa}\dot{R}$	$\dot{P}\dot{P}\dot{R}_{sa}$				
	$R_{sa}\dot{R}\dot{R}\dot{P}\dot{P}\dot{P}$	$\dot{R}\dot{R}_{sa}\dot{R}\dot{P}\dot{P}\dot{P}$	$\dot{R}\dot{R}\dot{R}_{sa}\dot{P}\dot{P}\dot{P}$	$\dot{R}\dot{R}\dot{P}\dot{P}_{sa}\dot{P}$	$\dot{R}\dot{R}\dot{P}\dot{P}_{sa}$	$R_{sa}\dot{R}\dot{P}\dot{P}\dot{P}$	$\dot{R}\dot{R}_{sa}\dot{P}\dot{P}\dot{P}$	$\dot{R}\dot{R}\dot{P}\dot{P}_{sa}\dot{P}$
	$\dot{R}\dot{P}\dot{P}_{sa}\dot{R}\dot{P}\dot{P}$	$\dot{R}\dot{P}\dot{P}_{sa}\dot{R}\dot{P}$	$\dot{R}\dot{P}\dot{P}_{sa}\dot{R}$	$\dot{R}\dot{P}\dot{P}_{sa}$	$R_{sa}\dot{P}\dot{R}\dot{P}\dot{P}$	$\dot{P}R_{sa}\dot{R}\dot{P}\dot{P}$	$\dot{P}\dot{R}\dot{R}_{sa}\dot{P}\dot{P}$	$\dot{P}\dot{R}\dot{P}\dot{P}_{sa}$
3R3P	$\dot{P}\dot{R}\dot{R}\dot{P}_{sa}\dot{P}$	$\dot{P}\dot{R}\dot{R}\dot{P}_{sa}$	$R_{sa}\dot{R}\dot{P}\dot{P}\dot{P}$	$\dot{R}\dot{R}_{sa}\dot{P}\dot{P}\dot{P}$	$\dot{R}\dot{P}\dot{P}_{sa}\dot{P}$	$\dot{R}\dot{P}\dot{P}_{sa}$	$\dot{R}\dot{P}\dot{P}_{sa}\dot{P}$	$\dot{R}\dot{P}\dot{P}_{sa}$
	$R_{sa}\dot{P}\dot{R}\dot{P}\dot{P}$	$\dot{P}R_{sa}\dot{R}\dot{P}\dot{P}$	$\dot{P}\dot{R}\dot{R}_{sa}\dot{P}\dot{P}$	$R_{sa}\dot{R}\dot{P}\dot{P}\dot{P}$	$\dot{R}\dot{R}_{sa}\dot{P}\dot{P}\dot{P}$	$\dot{R}\dot{P}\dot{P}_{sa}\dot{P}$	$\dot{R}\dot{P}\dot{P}_{sa}$	$\dot{R}\dot{P}\dot{P}_{sa}$

revolute joints, and all actuators can be located at the first and second joints from the base. These features are advantageous in protection and cable arrangement of actuators, protection and lubrication of joints, and dynamic performance of the manipulator.

6.1. Mechanism Configuration. The mechanism configuration and the definition of kinematic constants are given in Figure 8. The target application is a manipulator for assembly. Large utility workspace, fine orientation-adjustment capability, and small translational motion coupled with rotational motion when actuating subactive joints are required in such an application.

6.2. Utility Workspace. The reachable workspace of a manipulator is divided into areas according to singularity. Then, the area in which the manipulator can actually work is limited to one of the divided areas that do not contain singularity. Such areas are called “subworkspaces.” Once the manipulator is assembled, it can move inside a subspace. The largest subspace is called the “utility workspace” [7]. At a singular point of a parallel manipulator, the absolute value of the Jacobian matrix becomes zero or infinity, and the sign of the determinant of Jacobian matrix changes around the singular point. Based on this, the boundaries of subworkspaces can be identified, and the utility workspace can be obtained. The volume of the workspace is evaluated

FIGURE 8: Kinematic constants of the 3- $R_{sa}\dot{R}\dot{R}\dot{R}\dot{R}$ partially decoupled parallel mechanism.

by the normalized volume index NVI [22]. We calculated NVI by

$$NVI = \frac{\text{volume of the utility workspace}}{(2\pi L^3/3)}. \quad (3)$$

Here, the characteristic length L is $L = d_1 + \sum_{i=2}^5 a_{i,i+1}$.

TABLE 5: Kinematic constants of the prototype manipulator.

r_b	0.22 m	$a_{2,3}$	0.115 m
r_p	0.086 m	$a_{3,4}$	0.115 m
β	45 deg	$a_{4,5}$	0
d_1	0.06 m	$a_{5,6}$	0.190 m

6.3. Orientation-Adjustment Capability. The resolution of the platform orientation in the fine adjustment by the subactive joints is important as an evaluation item of orientation-adjustment capability of a TPMFAO. It is determined by the submatrix, B_{PD} , of the matrix, J_{PD} , in (2). Taking the worst case into consideration, the maximum singular value of B_{PD} is proposed as the index of the orientation-adjustment capability. This is denoted by *OAC*.

6.4. Coupling Index. Small translational motion coupled with rotational motion by the subactive joints is required to improve the pose accuracy of TPMFAO. The magnitude of this translational motion can be represented by the matrix, $C_{PD}B_{PD}^{-1}$. Then, an evaluation index, *CI*, called the ‘‘coupling index’’ is defined as the maximum singular value of $C_{PD}B_{PD}^{-1}$, which means the maximum translational displacement followed by rotational motion of the platform by a unit angle.

6.5. Kinematic Design and Performance Evaluation. We considered the volume of the utility workspace of the 3- \overline{RRRRR} translational mechanism by fixing the first revolute joint of 3- $R_{sa}\overline{RRRRR}$ partially decoupled mechanism. The constraint singularity of 3- \overline{RRRRR} translational mechanism is independent of the platform position and is determined by the angle β . If $\beta = 0$ or 90° , 3- \overline{RRRRR} is at a constraint singularity. Then, we determined this angle as $\beta = 45^\circ$. Since d_1 does not affect the performance of the mechanism, we determined it as $d_1 = 0.125 L$ taking into consideration the practical conditions in constructing a manipulator such as collisions between links. We then optimized the link lengths $a_{2,3}$, $a_{3,4}$, $a_{4,5}$, and $a_{5,6}$ subject to maximizing the volume of the utility workspace using *NVI* in (3) under the constraint of $L = \text{constant}$. The determined values of kinematic constants of the optimal mechanism are listed in Table 5. Its *NVI* is 0.144.

The evaluation indices in the reachable workspace of the manipulator are shown in Figure 9. We can see from Figure 9(a) that the manipulator can have good kinematic and static characteristics in the upper region of the reachable workspace ($Z > 0.25$ m) since the absolute of the determinant of the Jacobian matrix is within a preferable range of $10^{-4} \leq |\det J_{PD}| \leq 0.1$. Figure 9(b) shows a map of *OAC* at $Z = 0.24$ m and $\omega_z = 0$. Here, $(\omega_x, \omega_y, \omega_z)$ represents the axis and angle of rotation of platform from the initial state. At $(\omega_x, \omega_y, \omega_z) = (0, 0, 0)$, the initial state, *OAC* reaches a minimum of 0.816. Then, the resolution when the platform’s orientation around the initial state is adjusted is almost the same as that of the actuator, while *OAC* changes as the orientation of the platform changes. Figure 9(c) shows a map

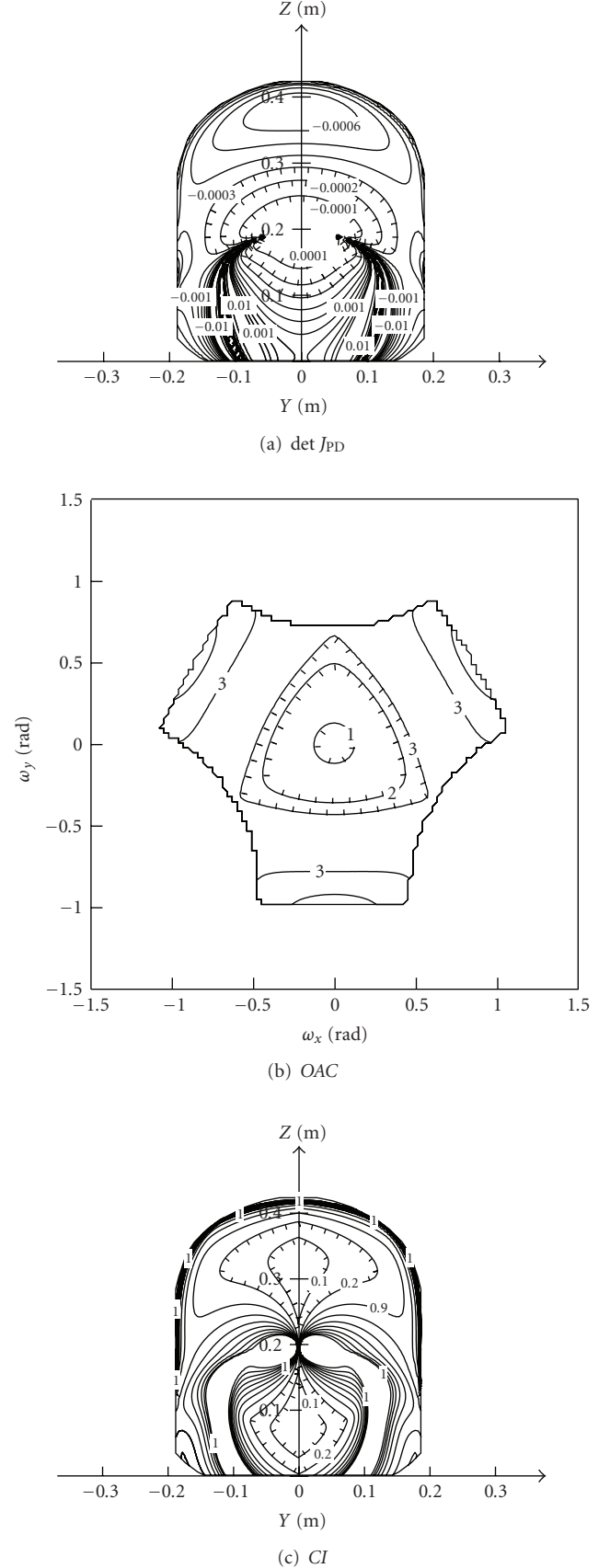


FIGURE 9: Distributions of evaluation indices in the reachable workspace.

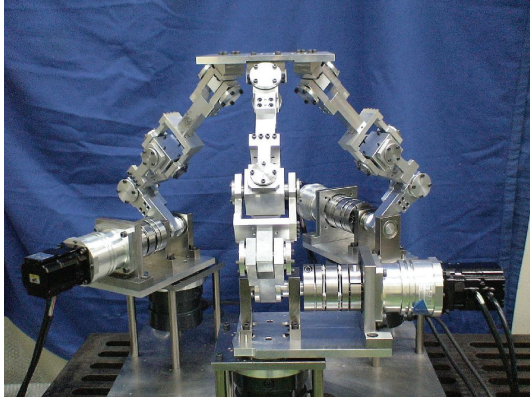


FIGURE 10: Overview of the prototype manipulator.

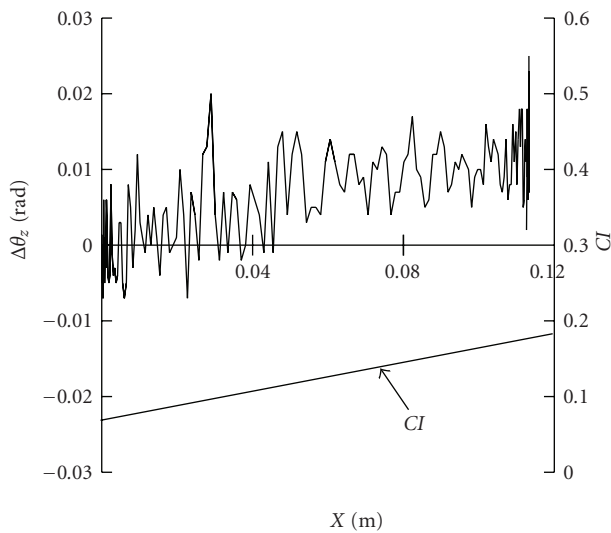


FIGURE 11: Result of trajectory tracking at $(\omega_x, \omega_y, \omega_z)=(0,0,0)$ (X : from 0 to 0.11 m, $Y=0$, $Z=0.35$ m).

of CI at $X=0$ m. We can see from this figure that the manipulator performs well in terms of the coupling index in the area of $|Y| \leq 0.15$ m of the upper area of the reachable workspace, in which its $|\det J_{PD}|$ is within a preferable range.

6.6. Prototype Manipulator. We built a prototype manipulator based on the results of kinematic design. Its overview is shown in Figure 10. We also constructed its control system. Figures 11 and 12 show the inclination angle of the platform (orientation error of the platform) and the evaluation index CI in the cases where trajectories of the platform are given so that the platform moves along the line (X -axis) without changing its orientation. In these experiments, no adjustment or compensation by the subactive joints was given while only the main active joints were actuated. Displacement X and orientation error $\Delta\theta_z$ were measured by a laser displacement sensor and accelerometers, respectively. In these figures, we can observe large orientation error at points of large CI . Then, it is expected that a mechanism with small orientation error without orientation adjustment

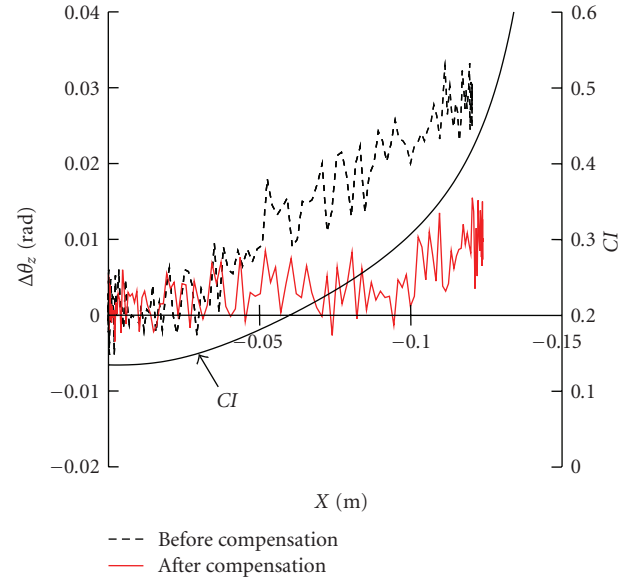


FIGURE 12: Result of trajectory tracking at $(\omega_x, \omega_y, \omega_z)=(0,0,0)$ (X : from 0 to -0.12 m, $Y=0$, $Z=0.35$ m).

by the subactive joints can be designed using CI as one of the evaluation indices in the kinematic synthesis. Moreover, we determined adjustment input for the subactive joints from the orientation error shown in Figure 12 so that the platform orientation error could be compensated for using (2) and then conducted an experiment using this input. The result is given in Figure 12. From this result, we can confirm that the orientation error of the platform was reduced by using the subactive joints. However, resultant error after compensation can be observed in the figure. It is expected to be resulted from the usage of the first-order approximation of the relationship between the input and output displacements (2). In order to eliminate the orientation error as the uncompensatable error of a translational manipulator with subactive joints, kinematic calibration and/or feedback compensation using iterative calculation based on the first-order model should be done as mentioned in Section 2. Based on these basic experimental results, we intend to carry out kinematic synthesis using CI and conduct more experimental studies in kinematic and dynamic modeling and calibration to achieve accurate motions in our future work.

7. Conclusions

We presented a kinematic design of a translational parallel manipulator with fine adjustment capability of platform orientation (TPMFAO). First, to clarify all possible kinematic structures whose main motion is translation and submotion is rotation, we carried out structural synthesis of fully and partially decoupled mechanisms based on the synthesis results of 3-dof translational and rotational parallel mechanisms. Based on these, we designed and built a prototype

TPMFAO. Through theoretical and experimental investigations, we confirmed the effectiveness of our approach and clarified our future work target.

References

- [1] D. Kim and W. K. Chung, "Kinematic condition analysis of three-dof pure translational parallel manipulators," *Journal of Mechanical Design*, vol. 125, no. 2, pp. 323–331, 2003.
- [2] X. Kong and C. M. Gosselin, "Type synthesis of 3-dof translational parallel manipulators based on screw theory," *Journal of Mechanical Design*, vol. 126, no. 1, pp. 83–92, 2004.
- [3] R. Di Gregorio, "Kinematics of the translational 3-URC mechanism," *Journal of Mechanical Design*, vol. 126, no. 6, pp. 1113–1117, 2004.
- [4] H. S. Kim and L.-W. Tsai, "Design optimization of a Cartesian parallel manipulator," *Journal of Mechanical Design*, vol. 125, no. 1, pp. 43–51, 2003.
- [5] D. Chablat and P. Wenger, "Architecture optimization of a 3-dof translational parallel mechanism for machining applications, the orthoglide," *IEEE Transactions on Robotics and Automation*, vol. 19, no. 3, pp. 403–410, 2003.
- [6] Y. Li and Q. Xu, "A new approach to the architecture optimization of a general 3-PUU translational parallel manipulator," *Journal of Intelligent and Robotic Systems*, vol. 46, no. 1, pp. 59–72, 2006.
- [7] M. Tanabe, Y. Takeda, and S. Huda, "Utility workspace of 3-5R translational parallel mechanism," *Journal of Advanced Mechanical Design, Systems, and Manufacturing*, vol. 2, no. 6, pp. 998–1010, 2008.
- [8] Y. Li and Q. Xu, "Design and development of a medical parallel robot for cardiopulmonary resuscitation," *IEEE/ASME Transactions on Mechatronics*, vol. 12, no. 3, pp. 265–273, 2007.
- [9] T. Tanikawa, M. Ukiana, K. Morita, et al., "Design of 3dof parallel mechanism with thin plate for micro finger module in micro manipulation," in *Proceedings of the IEEE International Conference on Intelligent Robots and Systems (IROS '02)*, vol. 2, pp. 1778–1783, 2002.
- [10] T. Huang, G. Tang, S. Li, Y. Li, G. D. Chetwynd, and J. D. Whitehouse, "Kinematic calibration of a class of parallel kinematic machines (PKM) with fewer than six degrees of freedom," *Science in China*, vol. 46, no. 5, pp. 515–526, 2003.
- [11] S. Syamsul and Y. Takeda, "Kinematic design of 3-URU pure rotational parallel mechanism with consideration of uncompensatable error," *Journal of Advanced Mechanical Design, Systems, and Manufacturing*, vol. 2, no. 5, pp. 874–886, 2008.
- [12] C. Innocenti and V. Parenti-Castelli, "Direct kinematics of the 6–4 fully parallel manipulator with position and orientation uncoupled," in *Proceedings of the European Robotics and Intelligent Systems Conference (EURISCON '91)*, pp. 3–10, Corfu, Greece, June 1991.
- [13] S. Patarinski and M. Uchiyama, "Position/orientation decoupled parallel manipulators," in *Proceedings of the IEEE International Conference on Advanced Robotics (ICAR '93)*, pp. 153–158, 1993.
- [14] K. Wohlhart, "Displacement analysis of the general spherical Stewart platform," *Mechanism and Machine Theory*, vol. 29, no. 4, pp. 581–589, 1994.
- [15] Z. J. Geng and L. A. Haynes, "A "3-2-1" kinematic configuration of a Stewart platform and its application to six degree of freedom pose measurements," *Robotics and Computer Integrated Manufacturing*, vol. 11, no. 1, pp. 23–34, 1994.
- [16] D. Bernier, J. M. Castelain, and X. Li, "A new parallel structure with six degrees of freedom," in *Proceedings of the 9th World Congress on the Theory of Machines and Mechanisms (IFToMM '95)*, pp. 8–12, Milan, Italy, 1995.
- [17] K. Mianovski, "Dextrous fully parallel manipulator with six degrees of freedom," in *Proceedings of the 12th CISM-IFToMM Symposium on Theory and Practice of Robots and Manipulators (RoManSy '98)*, pp. 253–260, Paris, France, 1998.
- [18] Y. Takeda, K. Kamiyama, Y. Maki, M. Higuchi, and K. Sugimoto, "Development of position-orientation decoupled spatial in-parallel actuated mechanisms with six degrees of freedom," *Journal of Robotics and Mechatronics*, vol. 17, no. 1, pp. 59–62, 2005.
- [19] Y. Jin, I.-M. Chen, and G. Yang, "Kinematic design of a 6-dof parallel manipulator with decoupled translation and rotation," *IEEE Transactions on Robotics*, vol. 22, no. 3, pp. 545–551, 2006.
- [20] X. Kong and C. M. Gosselin, "Type synthesis of 3-dof spherical parallel manipulators based on screw theory," *Journal of Mechanical Design*, vol. 126, no. 1, pp. 101–108, 2004.
- [21] Y. Fang and L.-W. Tsai, "Structure synthesis of a class of 3-dof rotational parallel manipulators," *IEEE Transactions on Robotics and Automation*, vol. 20, no. 1, pp. 117–121, 2004.
- [22] D. C. H. Yang and Y. Y. Lin, "Pantograph mechanism as a non-traditional manipulator structure," *Mechanism and Machine Theory*, vol. 20, no. 2, pp. 115–122, 1985.

Research Article

Optimal Design and Development of a Decoupled A/B-Axis Tool Head with Parallel Kinematics

Fugui Xie, Xin-Jun Liu, Li-Ping Wang, and Jinsong Wang

Department of Precision Instruments, Institute of Manufacturing Engineering, Tsinghua University, Beijing 100084, China

Correspondence should be addressed to Xin-Jun Liu, xinjunliu@mail.tsinghua.edu.cn

Received 21 March 2009; Accepted 27 September 2009

Academic Editor: Fengfeng Xi

Copyright © 2010 Fugui Xie et al. This is an open access article distributed under the Creative Commons Attribution License, which permits unrestricted use, distribution, and reproduction in any medium, provided the original work is properly cited.

This paper is an attempt to design a decoupled A/B-axis tool head with parallel kinematics, due to the increasing demand for A/B-axis tool heads in industry, particularly in thin wall machining applications for structural aluminium aerospace components. In order to carry out further analysis, the method of orientation description based on the *azimuth and tilt angles* is introduced, which is a convenient method describing kinematics, parasitic motions, and orientation workspace. For the purpose of optimal design, three indices are defined to evaluate the force transmission performance of the tool head. They have obvious physical significance and are dependent of any coordinate system. Based on the indices and their performance atlases, the optimization process is presented in detail. The parasitic motions and orientation capability of the designed tool head are analyzed finally. The results show that the designed device is far from singularity, has good force transmissibility, and has very high tilting angle. The indices and analysis and design method used here should be said to be extended to other parallel robots.

1. Introduction

Generally, a tool head that can rotate about the x -axis and y -axis is defined as A/B-axis tool head, and that can rotate about the x -axis and z -axis is defined as A/C-axis tool head. Most of the multifunction milling machines have a tool head with two rotational degrees of freedom (DOFs), and the tool head usually adopts the serial architecture, such as the A/C-axis tool head proposed in [1]. In order to reduce the machining time and deformation of the work piece, A/B-axis tool heads are used instead of the A/C-axis tool head in the manufacture of structural aircraft parts with thin walls. Such kind of serial tool head usually has complicated transmission system, huge structure and high weight, it is difficult to install, and moreover, the manufacture cost and maintenance fee is relatively high. And, in practical engineering application, this serial architecture has many disadvantages such as inconvenience for locus planning and control difficulty since its two rotations are not coupled motions due to its serial kinematic structure. Although the A/B-axis tool head with parallel kinematics has relatively small rotational angle compared with the serial tool head, it has high manufacturing efficiency and much

smaller deformation made to work piece. What is more, the parallel manipulator has the advantages of high stiffness, high velocity, compactness, time-saving of machining, high load/weight ratio, and low moving inertia. So, the A/B-axis tool head with parallel kinematics has the absolute advantage in the manufacture of structural aircraft parts with thin walls which needs mass cutting and high speed. Recently, parallel A/B-axis tool heads with high tilting angle have become the most important and fundamental part in the manufacturing field of key structural aircraft parts. DS Technology in Germany has developed a machining tool head [2], the Sprint Z3, and FATRONIK in Spain has developed the Space 5H tool head [3]. Both of them have made great success in engineering application. The Z3 tool head is based on a 3-DOF spatial 3-PRS (P, R, and S stand for prismatic, revolute, and spherical joints, resp.) parallel manipulator. It has a translational DOF along the z -axis and two rotational DOFs about the A and B axes, respectively. In this kind of tool head, the most important is the two rotational DOFs that provide the coupled tilting motion. And, generally, some machining centers just need the two rotational DOFs. So, the development of an A/B-axis tool head with parallel kinematics is becoming more and more popular.

For parallel manipulator, optimal design is one of the most important and challenging problems and is attracting more and more efforts [4–7]. There are two issues involved: performance evaluation and dimension synthesis. Having designed a mechanism, it is necessary to evaluate its performance. So, the first problem is of most importance and should be reconsidered due to the doubt of the mostly used index, that is, local conditioning index (LCI) [8]. The second problem is to determine the dimensions (link lengths) of the mechanism, which is suitable for the task at hand. It is one of the most difficult issues in the field.

Several well-defined performance indices which are popular in the field of serial mechanism, such as manipulability, workspace, singularity, dexterity, stiffness, and accuracy, have developed extensively and applied to the design of parallel manipulator. The LCI, which is the reciprocal of the condition number of Jacobian matrix, is usually used to evaluate the accuracy, dexterity, and distance to singularity of a parallel manipulator. For this reason, the LCI has drawn much more attention. However, a recent study [8] reviewed the LCI and global conditioning index (GCI) that is the computation over a kind of workspace of the manipulator. The study found serious inconsistencies when these indices are applied to parallel manipulators with combined translational and rotational degrees of freedom and conclude that these indices should not be used in parallel manipulators with mixed types of DOFs (translational and rotational). To eliminate the singularity and its near configurations, most researchers use the local conditioning index (LCI). Usually, a good-condition workspace [9] or effective workspace [10] was defined with respect to a specified minimum LCI. However, the minimum is still arbitrary or comparative since we cannot give it a defined value due to its frame-dependent characteristic. Generally, it is impossible to define a mathematical distance to a singularity for a parallel manipulator. Thus, the authors think that the LCI cannot be used in parallel manipulator, but not only those with mixed type of DOFs.

As is well known, the planar four-bar mechanisms have been studied for a very long time, longer than that of serial robots and much longer than that of parallel manipulators. The transmission angle is an important index for the design of such a mechanism as was pointed out by Alt [11], who defined the concept, using the forces tending to move the driven link and tending to apply pressure to the driven link bearings as a simple index, to judge the force-transmission characteristics of a mechanism. So, the transmission angle is an index evaluating the quality of motion/force transmission. By means of the index of transmission angle, the quality of motion/force transmission in a mechanism can be judged in the design stage. And it helps to decide the best from a family of possible mechanisms for the most effective force transmission [12]. Also, the transmission angle of a mechanism provides a very good indication of the quality of its motion, the accuracy of its performance, its expected noise output, and its cost in general [13]. Although a good transmission angle is not a cure-all for all design problems, as is pointed out in [14], for many mechanical

applications it can guarantee the performance of a linkage at higher speed without unfavorable vibrations. The study [15] shows that when the transmission angle equals to 90° , the most effective force transmission takes place and the output motion becomes less sensitive to the manufacturing tolerances on the link lengths, clearance between joints, and change of dimensions due to thermal expansion. A large transmission angle usually leads to reasonable mechanical advantages and a high quality of motion transmission. The study of link mechanisms shows that transmission angle is significant not only as an indicator of good force and motion transmission but also as a prime factor in the linkage sensitivity to small design parameter errors. The smaller the transmission angle is, the more sensitive the linkage will be [16]. Mechanisms having a transmission angle too far from 90° exhibit poor operational characteristics such as noise and jerk at high speeds [17, 18], and many studies have reached the conclusion that if the transmission angle becomes too small, the mechanical advantage becomes small, even a very small amount of friction will lead the mechanism to jam, and if it is 0, self-locking takes place. For the purpose of high speed, high accuracy, and high quality of motion transmission, the most widely accepted design limits for the transmission angle are $(45^\circ, 135^\circ)$ [18] or $(40^\circ, 140^\circ)$ [11].

A planar four-bar mechanism is a single-closed-loop system. A parallel manipulator is a multiclosed-loop system. Usually, a fully parallel manipulator has more or less the characteristic of a planar four-bar mechanism. We suggest that the design concept of the four-bar mechanisms could be used in the design of a parallel manipulator. In this paper, the *local* and *global transmission indices* (defined in Section 5.2) based on the concept of transmission angle will be proposed as indices in the optimal design of an A/B-axis tool head with parallel kinematics, which can be kinematically considered as the combination of two slider-crank mechanisms at any moment.

Many methods have been proposed for the dimensional optimization of a specified mechanism. The most common method is the objective-function-based optimal design. According to this method, an objective function with specified constraints must be established, and then a search is conducted to find the result utilizing an optimum algorithm. Not only is this method time consuming, but it is difficult to reach the globally optimum target because of the infiniteness of the individual parameters, the antagonism of multiple criteria, and the assignment of initial values. The most serious drawback is that it provides only one solution for a design problem. This is actually unreasonable for a practical design, since it is impossible to predict any application in advance and to know whether a particular design is the only solution.

The ideal dimensional optimization method would be that using the performance charts (atlas), which is widely used in classical design. A performance atlas can show, visually and globally, the relationship between a performance index and the associated design parameters in a limited space [19]. Moreover, it can show how antagonistic the involved indices actually are. Compared with the result achieved

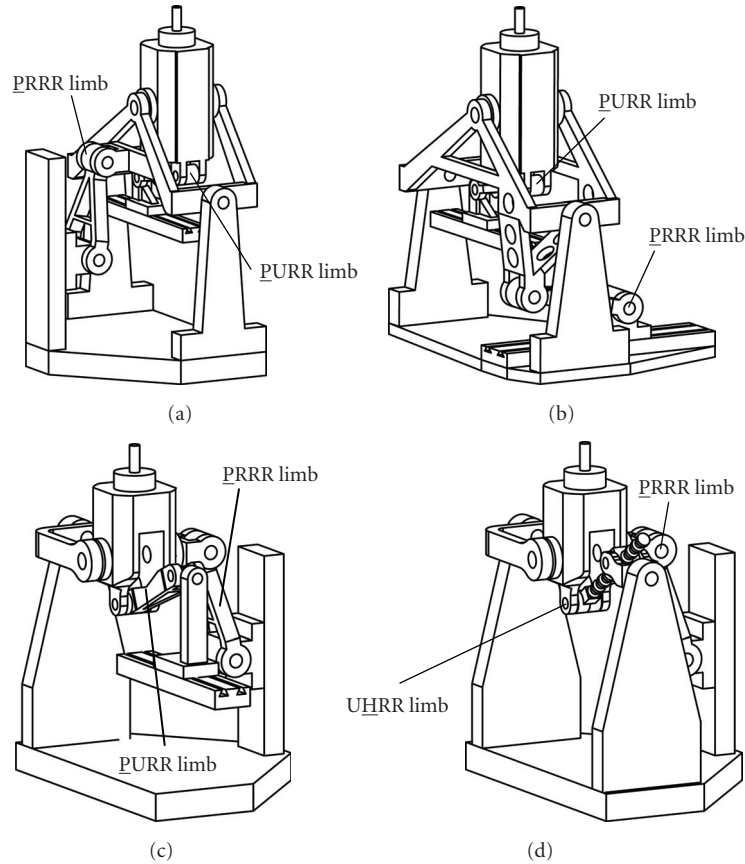


FIGURE 1: The CAD models of the A/B-axis tool head with parallel kinematics (P-prismatic joint, R-revolute joint, U-universal joint, H-helical joint, and the underlined joints are active.).

by the objective-function-based method, the result of this optimal method is comparative and fuzzy. However, it is more flexible, because it provides not only a single solution, but also all possible solutions to a design problem. This means that the designer can adjust the optimum result appropriately according to the particular design conditions he is dealing with [20]. This method will be extended to the dimensional optimization of the A/B-axis tool head with parallel kinematics.

The remainder of this paper is organized as follows. The next section describes the structure of the proposed tool head with different configurations. Section 3 introduces the method of orientation description of the tool head and analyzes the relationship between orientational angles and output angles of the two legs, and then, the parasitic motions are given. Section 4 investigates the inverse kinematics of the tool head. Section 5 recalls the classical concept of *transmission angle*, defines the *forward* and *inverse transmission angle*, proposes some indices, and then, plots performance atlases for these new indices and presents the optimal design using the atlases. Section 6 analyzes the orientation capability and parasitic motions of the tool head given in Section 5. Development of the tool head is presented in Section 7 and conclusions are given in Section 8.

2. Structure Description

The A/B-axis tool head with parallel kinematic, shown in Figure 1, contains a moving platform which connects to the base through two legs. The first leg contains a fixed length link and a bracket, the bracket can rotate about the y -axis through a revolute joint, another revolute joint connects the link to the bracket, the other end of the link is connected to an active slider through a revolute joint, and the slider is attached to the base by a prismatic joint whose move direction is vertical (Figures 1(a), 1(c), and 1(d)) or horizontal (Figure 1(b)). The second leg contains a fixed length link (Figures 1(a), 1(b), and 1(c)) or an extensible link which is active (Figure 1(d)). For the models shown in Figures 1(a), 1(b), and 1(c), the link is connected to the active slider through a universal joint. For the model shown in Figure 1(d), the active link is connected to the base through a screw joint and a universal joint. The moving platform is connected with the two legs by two revolute joints, respectively. In order to make it move, the axes of the revolute joint fixed to the bracket and that of the universal joint in y -axis direction must be collinear. The rotational axes of the moving platform are orthogonal but not coplanar for the models shown in Figures 1(a) and 1(b); they are orthogonal and coplanar for the models shown in Figures

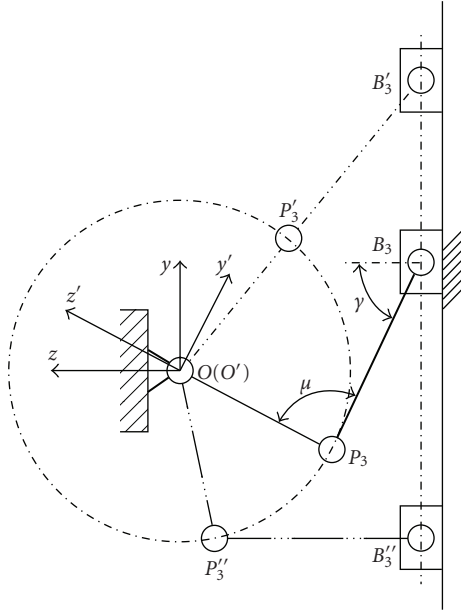


FIGURE 2: A slider-crank mechanism.

1(c) and 1(d). It is not difficult to find that the two rotations of any one of the structures are decoupled.

From the above description, one can see that, at any moment, this kind of A/B-axis tool head can be considered as the combination of two slider-crank mechanisms. The slider-crank mechanism, shown in Figure 2, is a classical planar four-bar mechanism. And such a combination can make sure that this A/B-axis tool head is decoupled. As is well known, a decoupled mechanism is easier to control and achieve higher accuracy.

We may see that the models shown in Figures 1(a), 1(b), and 1(c) are similar in kinematics but are different from that shown in Figure 1(d). In this paper, we will mainly focus on the models shown in Figures 1(a) and 1(d). For the former model, its kinematic scheme is shown in Figure 3, where the two rotational axes of the moving platform are orthogonal but not coplanar. Thus, such a mechanism has parasitic motion which will be analyzed in the next section. We call such a case the case I in this paper. For the later model in Figure 1(d), its kinematic scheme is shown in Figure 4, where the two rotational axes of the moving platform are orthogonal and coplanar. There is no parasitic motion for this mechanism. This is a great advantage for application. We call such a case the case II.

3. Orientation Description of the Parallel A/B-Axis Tool Head

Most researchers have used Euler angles to describe the orientation of a parallel manipulator. For the manipulator discussed in this paper, this method is inconvenient to describe the orientation and to analyze the kinematic problems. We will use another method introduced in [21], which is suitable for the task at hand. For any feasible

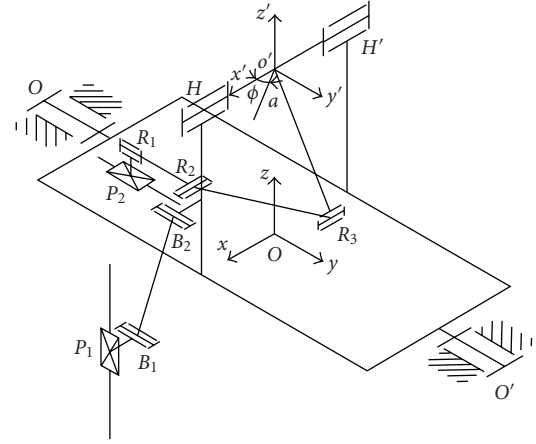


FIGURE 3: kinematical scheme of the model with parasitic motions (Figure 1(a)).

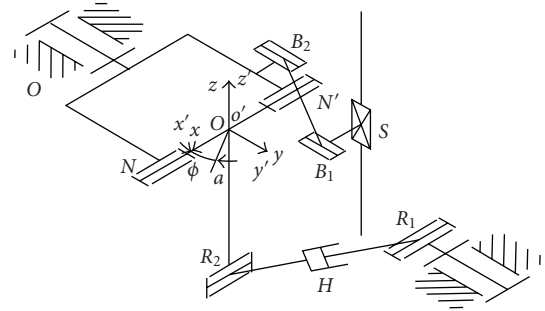


FIGURE 4: kinematical scheme of the model with no parasitic motion (Figure 1(d)).

orientation of the moving platform of a mechanism with two rotational DOFs, its two rotations can be obtained from the reference (home) orientation by a single rotation about a line passing through the center of the moving platform. Here, two angular parameters are involved. The azimuth angle, denoted by ϕ , defines an a -axis passing through the platform center o' (Figure 3) or o (Figure 4) and lying in the $o'-x'y'$ or $o-xy$ plane, and the tilt angle, denoted by θ , describes the swing angle about the a -axis. And, the corresponding rotation matrix can be written as

$$R_a(\theta) = \begin{bmatrix} \cos^2\phi\mathfrak{A} + \cos\theta & \sin\phi \cos\phi\mathfrak{A} & \sin\phi \sin\theta \\ \sin\phi \cos\phi\mathfrak{A} & \sin^2\phi\mathfrak{A} + \cos\theta & -\cos\phi \sin\theta \\ -\sin\phi \sin\theta & \cos\phi \sin\theta & \cos\theta \end{bmatrix}, \quad (1)$$

where \mathfrak{A} denotes $(1 - \cos\theta)$, ϕ is measured between the x' -axis and the a -axis, and $\phi \in (0, 360^\circ)$, $\theta \in (0, 90^\circ)$.

As analyzed above, this mechanism can be considered as the combination of two slider-crank mechanisms. Then, there are two independent rotational angles about the y -axis and x -axis or x' -axis, respectively, and they are referred to as α and β , correspondingly.

In order to carry on further analysis, we need to find out the relationship between (ϕ, θ) and (α, β) and that between

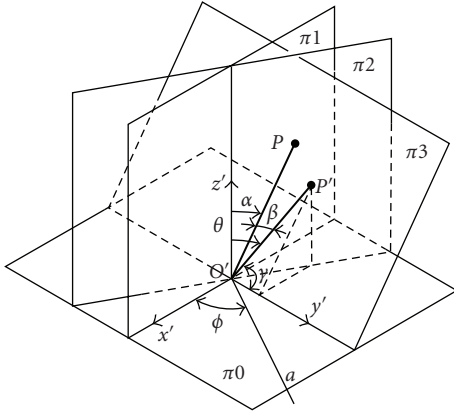
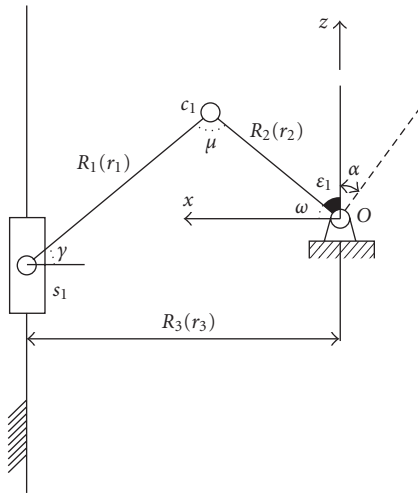

 FIGURE 5: The projective relationship between (ϕ, θ) and (α, β) .


FIGURE 6: The first leg of the tool head.

the parasitic motions and (ϕ, θ) . The projective relationship is shown in Figure 5.

Point P denotes the tip of the tool, and o' is the center of the moving platform. Angular parameter α is defined as the rotational angle from home orientation of $o'P$ about the y' -axis in the π_1 plane, and β is referred to the rotational angle from current orientation of $o'P$ to the orientation of $o'P$ in the π_3 plane. The planes π_1 and π_3 are orthogonal to each other. θ is the angle mentioned above, which is the rotational angle from home orientation of $o'P'$ about a -axis in the π_2 plane, and the a -axis is orthogonal to the π_2 plane. π_0 denotes the $o'-x'y'$ plane. ϕ is the angle between the x' -axis and a -axis in π_0 plane.

Letting $o'P = o'P' = l$, we can get

$$\begin{aligned} l \cos(90^\circ - \beta) &= l \cos(90^\circ - \theta) \cos(\phi), \\ l \cos(90^\circ - \theta) \sin(\phi) \tan(\alpha) &= l \sin(90^\circ - \theta). \end{aligned} \quad (2)$$

That is

$$\begin{aligned} \beta &= 90^\circ - \arccos[\sin(\theta) \cos(\phi)], \quad \beta \in (-90^\circ, 90^\circ), \\ \alpha &= \tan^{-1}[\tan(\theta) \sin(\phi)], \quad \alpha \in (-90^\circ, 90^\circ). \end{aligned} \quad (3)$$

For the case I (shown in Figure 3), $oo' = R$, and (x, y, z) is the position of the point o' .

Please note that, for the second leg shown in Figure 7(a), $oo' = R = D_3$ is required to allow the first leg shown in Figure 6 to rotate about y -axis.

Then, the parasitic motions can be described as

$$\begin{aligned} x &= R \cos(90^\circ + \alpha), \\ y &= 0, \\ z &= R \sin(90^\circ + \alpha). \end{aligned} \quad (4)$$

For the case II (shown in Figure 4), $oo' = R = 0$; so, there is no parasitic motion.

4. Inverse Kinematic Analysis of the Tool Head

4.1. Inverse Kinematics of the Tool Head with Parasitic Motions. For the case I, a kinematical scheme of the tool head is developed as shown in Figure 3, and the first and second legs are shown in Figures 6 and 7(a), respectively. A fixed global reference frame $o-xyz$ is located at the center of the bracket with the y -axis being collinear with the rotational axis of the first leg and the plane $o-xy$ being horizontal.

A mobile reference frame $o'-x'y'z'$ is located at the center of the rotational axis of the second leg with the x -axis being collinear with this rotational axis and the z -axis directing along oo' , which is also the direction of the tool.

As shown in Figures 6 and 7(a), the planar schemes of the first and second legs are similar in configuration. The geometric parameters will be $s_1c_1 = R_1$, $c_1o = R_2$ and the normal distance from point o to the straight-line path of the joint point s_1 is R_3 . And the adjusting angles ε_1 and ε_2 are constants which will be given in the optimal process.

Vectors \mathbf{s}_1 , \mathbf{c}_1 , \mathbf{s}_2 , and \mathbf{c}_2 are defined as the position vectors of points s_1 , c_1 , s_2 , and c_2 in the reference frame $o-xyz$ and can be written as

$$\begin{aligned} \mathbf{s}_1 &= (R_3, 0, z), \\ \mathbf{c}_1 &= \left(R_2 \cos\left(\frac{\pi}{2} - \varepsilon_1 + \alpha\right), 0, R_2 \sin\left(\frac{\pi}{2} - \varepsilon_1 + \alpha\right) \right), \\ \mathbf{s}_2 &= (0, y, -D_3), \\ \mathbf{c}_2 &= \left(0, D_2 \cos\left(\frac{\pi}{2} - \varepsilon_2 - \beta\right), D_2 \sin\left(\frac{\pi}{2} - \varepsilon_2 - \beta\right) + R \right). \end{aligned} \quad (5)$$

The kinematic problem of the tool head can be solved by writing the constraint equations:

$$\begin{aligned} |\mathbf{s}_1\mathbf{c}_1| &= R_1, \\ |\mathbf{s}_2\mathbf{c}_2| &= D_1. \end{aligned} \quad (6)$$

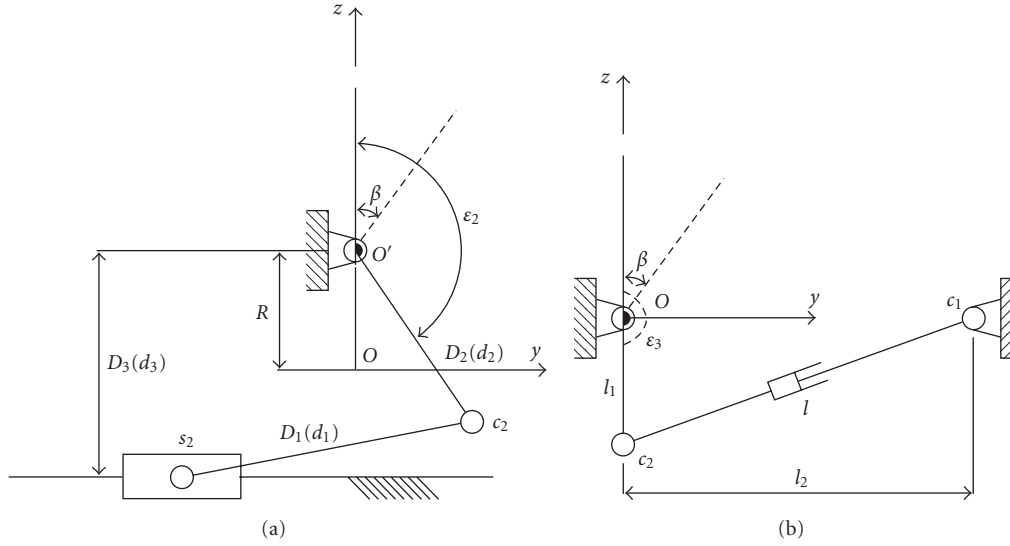


FIGURE 7: The second leg of the tool head: (a) for the model in Figure 1(a) and 1(b) for the model in Figure 1(d).

Then, there are

$$\begin{aligned} & \left[R_2 \cos\left(\frac{\pi}{2} - \varepsilon_1 + \alpha\right) - R_3 \right]^2 + \left[R_2 \sin\left(\frac{\pi}{2} - \varepsilon_1 + \alpha\right) - z \right]^2 \\ & = R_1^2, \\ & \left[D_2 \cos\left(\frac{\pi}{2} - \varepsilon_2 - \beta\right) - y \right]^2 + \left[D_2 \sin\left(\frac{\pi}{2} - \varepsilon_2 - \beta\right) + R + D_3 \right]^2 \\ & = D_1^2. \end{aligned} \quad (7)$$

The inputs y and z can be obtained as

$$y = \frac{-b \pm \sqrt{b^2 - 4c}}{2}, \quad (8)$$

$$z = \frac{-e \pm \sqrt{e^2 - 4g}}{2}, \quad (9)$$

where

$$\begin{aligned} b & = -2D_2 \cos\left(\frac{\pi}{2} - \varepsilon_2 - \beta\right), \\ c & = D_2^2 - D_1^2 + (R + D_3)^2 + 2D_2(R + D_3) \sin\left(\frac{\pi}{2} - \varepsilon_2 - \beta\right), \\ e & = -2R_2 \sin\left(\frac{\pi}{2} - \varepsilon_1 + \alpha\right), \\ g & = R_2^2 + R_3^2 - R_1^2 - 2R_3R_2 \cos\left(\frac{\pi}{2} - \varepsilon_1 + \alpha\right). \end{aligned} \quad (10)$$

For a given pose (ϕ, θ) , substituting (3) into (10), we can get the inputs y and z easily. The parasitic motions can be got from (4).

4.2. Inverse Kinematics of the Tool Head without Parasitic Motions. For the case **II**, a kinematical scheme of the tool head is developed as shown in Figure 4, and the first and second legs are shown in Figures 6 and 7(b), respectively.

The fixed global reference frame $o-xyz$ is the same as that in Section 4.1. A mobile reference frame $o'-x'y'z'$ is located at the intersecting point of the two rotational axes with the x -axis being collinear with the rotational angle of the second leg and the y -axis being collinear with the rotational angle of the first leg. It is clear that the fixed and mobile reference frames are identical at this moment.

Compared with case **I**, only the second leg is different. So, we will focus on the mechanism shown in Figure 7(b).

The point c_1 locates at the intersecting line of the $o-yz$ plane and the horizontal plane passing through the point o . The geometric parameters will be $oc_2 = l_1$ and $oc_1 = l_2$. Then, the extensible link length l can be expressed as follows:

$$l = \sqrt{l_1^2 + l_2^2 - 2l_1l_2 \cos\left(\frac{\pi}{2} + \beta\right)}. \quad (11)$$

Therefore, for case **II** the inputs z and l can be obtained through (9) and (11).

5. Kinematic Optimum Design

5.1. Transmission Angle. The *transmission angle* is something we are very familiar with without realizing it; it is a classical concept in the field of four-bar mechanism design. In fact, in our daily life, we frequently try to move something which is constrained in some way and cannot be moved freely, such as the handle of a crank, a curtain on a rail, and a sliding door. In all of these cases, the object may not be able to be moved even when we exert pressure against it. Let us take the case of the handle of a crank as an example. As shown in Figure 8, the crank is attached to the base with a constant counterclockwise moment M ; to move it, we must

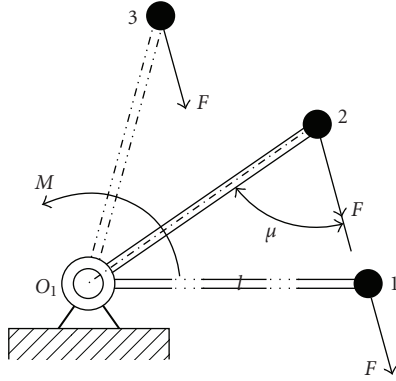


FIGURE 8: The handle of a crank.

apply a right-hand force F at the end of the crank; when the direction of the force is constant, depending on the position of the end point it may be more or less easy to start rotating. This is actually a matter of the *transmission angle*. Since the direction of motion of a crank is always perpendicular to the crank, the smaller angle between the force and crank is defined as the transmission angle, denoted as μ . When the force is normal to the crank, that is, identical to the direction of motion, force transmission is most effective; when the force is perpendicular to the direction of motion, force transmission is very inefficient.

For the planar four-bar mechanism shown in Figure 9, O_1A is the input link, and the force applied to the output link BO_2 is transmitted through the coupler link AB . For sufficiently slow motions (negligible inertia forces), the force in the coupler link is pure tension or compression (negligible bending action) and is directed along AB . For a given force in the coupler link, the torque transmitted to the output bar (about point O_2) is at a maximum when the angle μ between the coupler bar AB and the output bar BO_2 is 90° . Therefore, angle ABO_2 is called the *transmission angle*. In [17], the *transmission angle* is defined as the smaller angle between the direction of the velocity difference vector of the driving link and the direction of the absolute velocity vector of the output link, both taken at the point of connection. Although there are other definitions (see [11, 22], e.g.), all these definitions are somehow related to a joint variable(s) of the mechanism.

When the transmission angle deviates significantly from 90° , the torque on the output bar decreases and may not be sufficient to overcome the friction in the system. For this reason, the deviation angle $\alpha = |90^\circ - \mu|$ should not be too great.

Meanwhile, at the moment that the angle γ between the input link O_1A and the coupler link AB is 0 or 180° , as shown in Figure 9, the output point B will not move whatever the input is. Then, the motion of the input cannot be transmitted to the output effectively. This means that the output point will lose a degree of freedom. Therefore, the deviation angle $\beta = |90^\circ - \gamma|$ should not be too great either. In this paper, the angle μ is defined as the *forward transmission angle*, and the angle γ is referred to as the *inverse transmission angle*. If BO_2

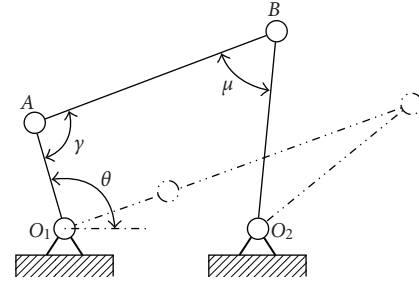


FIGURE 9: Transmission angle.

is an active link, the angle O_1AB is the *forward transmission angle* and angle ABO_2 the *inverse transmission angle*.

Take the slider-crank mechanism shown in Figure 2 as an example, where angle $O'P_3B_3$ is the *forward transmission angle* and the angle between the coupler link and the normal to the straight-line path of the slider is the *inverse transmission angle* if the slider is actuated.

5.2. Definition of Some Indices

5.2.1. Local Transmission Index (LTI).

The condition number of the Jacobian matrix is an index that has been used successfully in the design of serial robots. Although the condition number is depended on the coordinate frame, it has the main advantage of describing the kinematic behavior of a robot by means of a number. The index has also been applied in the analysis and design of parallel robots. It was used as an index to evaluate the accuracy/dexterity [23, 24], to describe the closeness of a pose to a singularity of a parallel robot [25, 26]. In an optimal design, the condition number (or its reciprocal) was used to define a useful, good-condition, or effective workspace with a specified minimum LCI [10, 19, 27]. However, the minimum is still arbitrary or comparative since we cannot give it a definite value. Generally, it is not possible to define a mathematical distance to a singularity for a parallel robot [8]. Instead of LCI, another index will be defined here.

Following the definition of transmission index proposed in [28], an index based on the transmission angle is defined as

$$\chi = \sin(TA), \quad (12)$$

where $TA = \mu$ or $TA = \gamma$. Then, there is

$$0 \leq \chi \leq 1. \quad (13)$$

A larger χ indicates better motion/force transmission. Since at a different pose the transmission angles will be different, the index χ is referred to as the *local transmission index (LTI)* in this paper. The angle is defined as the figure formed by two lines diverging from a common point, or as that formed by two planes diverging from a common line. Thus, the angle is usually measured by the ratio of two linear parameters. Therefore, the LTI is definitely independent of any coordinate frame. This is one of its advantages and is the most important for the optimal design of mechanisms.

For the purpose of high speed and high quality of motion/force transmission, the most widely accepted range for the transmission angle is $(45^\circ, 135^\circ)$ [18] or $(40^\circ, 140^\circ)$ [11]. Therefore, the LTI limit will correspondingly be

$$\chi > \sin\left(\frac{\pi}{4}\right) \quad \text{or} \quad \chi > \sin\left(\frac{2\pi}{9}\right). \quad (14)$$

Then, unlike the LCI, the LTI has a significant limitation to its application.

It is worth mentioning that, in [26, 29], the authors defined a transmission index, that is, $\cos \alpha$, by using the concept of the pressure angle α . Since the pressure angle is the complement of the transmission angle, the two definitions have the same significance. However, the authors did not define indices to evaluate a workspace with good transmission and to judge the effectiveness of motion/force transmission of a robot over a whole workspace. The two kinds of indices will be very important in the design of a parallel robot.

5.2.2. Good-Transmission Workspace (GTW). With the minimum of LTI, that is, $\sin(\pi/4)$ or $\sin(2\pi/9)$, we can identify a workspace for a mechanism. The corresponding workspace is referred to as a *good-transmission workspace (GTW)*, which is defined as the set of pose where the transmission index for every transmission angle is greater than $\sin(\pi/4)$ or $\sin(2\pi/9)$. In other words, within the GTW, at every pose the sine of every transmission angle is subject to the condition given by (14).

5.2.3. Global Transmission Index (GTI). The LTI χ can only judge the effectiveness of motion/force transmission of a robot at a single pose. Usually, a robot performs a task in a specified workspace but not at a pose. In a practical design, we should make a decision whether a robot is good or not by taking into account the behavior within a considering workspace. In order to measure the global behavior of the motion/force transmission over the whole GTW, following the definition of GCI suggested in [30], a *global transmission index (GTI)* is defined as

$$\Gamma = \frac{\int_W \sum_i^n \chi_i / ndW}{\int_W dW} \quad (15)$$

in which W denotes the good-transmission workspace, n the number of transmission angles, and $\Gamma_{\min} < \Gamma < 1$ (Γ_{\min} equals $\sin(\pi/4)$ or $\sin(2\pi/9)$). It is obvious that the GTI is also independent of any coordinate frame.

Undoubtedly, for manipulators with different link lengths, their GTWs will be the same. If such a case occurs, we cannot judge which robot is better with respect to the GTW index itself. However, with the same GTWs, their GTIs may be different. The two indices, GTW and GTI, together will help us to design a robot optimally. Additionally, for a specified design problem, other performance indices such as stiffness and accuracy may be involved in identifying a better solution. This is not the content of the paper. To demonstrate the use of the proposed indices, that is, LTI, GTI, and GTW,

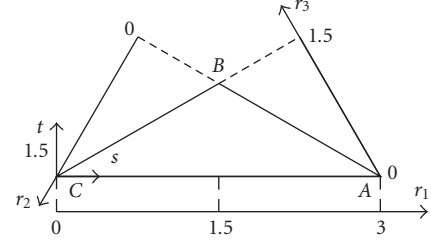


FIGURE 10: Parameter design space of the slide-crank mechanism.

the subsequent section will discuss the optimal design of the A/B-axis tool head with parallel kinematics proposed in Section 2.

5.3. Performance Atlas. As analyzed in Section 2, to optimize the proposed A/B-axis tool head, we should first analyze the slider-crank mechanism.

For the case **I**, the first and second legs are similar. We need just to analyze one of them; here, we consider the mechanism shown in Figure 6. By using the normalization method introduced in [20], we here have three normalization parameters r_1 , r_2 , and r_3 for R_1 , R_2 , and R_3 . The *parameter design space* of the slider-crank mechanism is constrained by

$$r_1 + r_2 + r_3 = 3, \quad r_1 + r_2 > r_3, \quad r_2 \leq r_3, \quad (16)$$

where $r_i = R_i/D$ ($i = 1, 2, 3$) and $D = (R_1 + R_2 + R_3)/3$ is the normalization factor. The parameter design space is shown in Figure 10.

We can easily get the relationship between s , t , and r_1 , r_2 , r_3 , that is,

$$\begin{aligned} s &= r_1, \\ t &= \sqrt{3} - \frac{\sqrt{3}}{3}r_1 - \frac{2\sqrt{3}}{3}r_2, \\ r_1 &= s, \\ r_2 &= \frac{3 - s - \sqrt{3}t}{2}, \\ r_3 &= 3 - r_1 - r_2. \end{aligned} \quad (17)$$

We should first find out the *usable workspace*, which is defined as the maximum continuous workspace that contains no singular loci inside but bounded by singular loci outside, in the *parameter design space*. For the slider-crank mechanism, the *usable workspace* can be written as $W_{\omega_UW} = |\omega_{O1} - \omega_{O2}|$, where ω_{O1} and ω_{O2} are the output angles when the mechanism is singular, respectively. And the atlas of the *usable workspace* of the slider-crank mechanism is shown in Figure 11. It is clear that, when s is near 1.5, the mechanism has a relatively larger usable workspace.

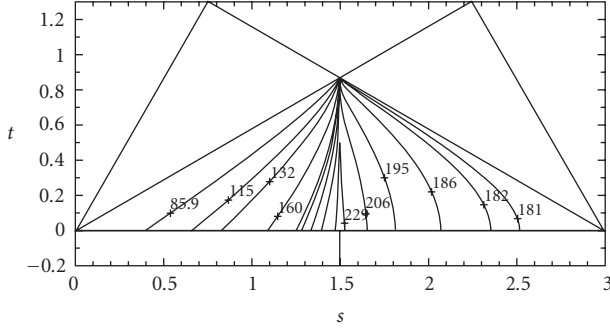


FIGURE 11: The usable workspace of the slider-crank mechanism.

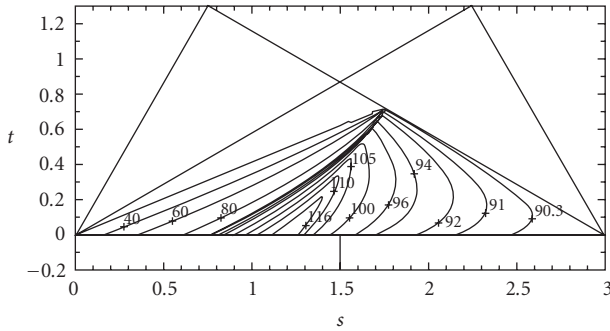


FIGURE 12: Atlas of the good transmission workspace (GTI) of the slider-crank mechanism.

As shown in Figure 6, according to (16), the *forward and inverse transmission angles* of the normalized mechanism can be obtained as

$$\begin{aligned} \mu &= \cos^{-1} \left(\frac{r_1^2 + r_2^2 - l^2}{2r_1 r_2} \right), \\ \gamma &= \cos^{-1} \left(\frac{r_3 - r_2 \cos(\omega)}{r_1} \right), \end{aligned} \quad (18)$$

where ω is the output angle, and $l^2 = (r_1 \sin \gamma + r_2 \sin \omega)^2 + r_3^2$.

Suppose that when $\omega \in (\omega_{\min}, \omega_{\max})$, the two transmission angles μ and γ in (18) are all subject to the LTI constraint given by (14). Here, ω_{\min} and ω_{\max} are the output angles where one of $\sin \mu$ and $\sin \gamma$ is equal to $\sin(\pi/4)$ or $\sin(2\pi/9)$ and another one is subject to (14). Then, the GTW for the output angle is defined as the relative angle between the two orientations ω_{\min} and ω_{\max} . If the workspace is denoted as W_{ω_GTW} , we get

$$W_{\omega_GTW} = \omega_{\max} - \omega_{\min}. \quad (19)$$

Figure 12 gives the relationship between W_{ω_GTW} and s, t when $\chi \geq \sin(\pi/4)$. It shows that, when s is near 1.5 and t is less than 0.5, that is, r_1 is near 1.5 and r_3 is more than 0.5 and less than 1, the mechanism has a larger GTW.

The relationship between *good transmission index* (GTI) and s, t when $\chi \geq \sin(\pi/4)$ is shown in Figure 13, from which we can see that the GTI is inversely proportional to the parameter r_3 and is proportional to the parameter r_2 .

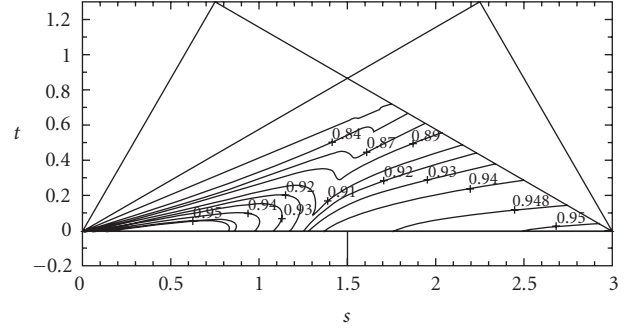


FIGURE 13: Atlas of the good transmission index (GTI) of the slider-crank mechanism.

For the case **II**, the first leg is identified with that of the case **I**; what we need do is to analyze the extensible link mechanism shown in Figure 7(b).

Through similar process of normalization, we can get the normalization parameters l_1 and l_2 for L_1 and L_2 . The parameter design space of the extensible link mechanism is constrained by

$$l_1 + l_2 = 2, \quad l_1 < l_2, \quad (20)$$

where $l_i = L_i/D$, ($i = 1, 2$) and $D = (L_1 + L_2)/2$ is the normalization factor. From (20), we know that $l_1 \in (0, 1)$.

For the extensible link mechanism, only one transmission angle, that is, $\mu = \angle OC_2 C_1$ should be considered. When $l_1 < l_2$ and $45^\circ \leq \mu \leq 135^\circ$, we can get the two limit points C'_2 and C''_2 of point C_2 , as shown in Figures 14 and 15.

From Figure 14, we can get

$$\begin{aligned} \frac{l_1}{\sin(\lambda_1)} &= \frac{l_2}{\sin(45^\circ)}, \\ \frac{l_1}{\sin(\lambda_2)} &= \frac{l_2}{\sin(135^\circ)}. \end{aligned} \quad (21)$$

Then

$$\lambda_1 = \lambda_2. \quad (22)$$

That is to say that points C_1 , C'_2 , and C''_2 are collinear as shown in Figure 15.

So, the angle between OC'_2 and OC''_2 is 90° .

Figure 16 shows the relationship between GTW and l_1 ($l_1 \in (0, 1)$), from which we can see that $W_{gtw} = 90^\circ$ when $\mu \in (45^\circ, 135^\circ)$. And Figure 17 gives the relationship between GTI and l_1 ($l_1 \in (0, 1)$).

5.4. Dimension Optimization Using the Performance Atlases.

For the case **I** shown in Figure 3, we consider the design problem that the desired rotational angle is as much as $\pm 50^\circ$ at every point of the workspace. The optimization process of the first leg shown in Figure 6 based on the atlases of Figures 12 and 13 can be summarized as follows.

Step 1. Identification of an optimum region in the parameter design space.

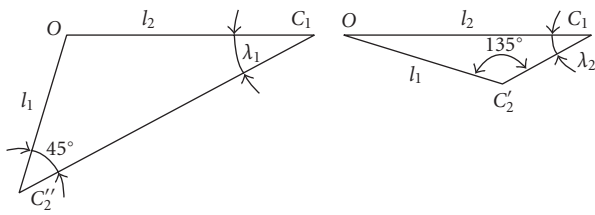


FIGURE 14: The relationship between λ_1 and λ_2 when $\mu = 45^\circ$ or 135° .

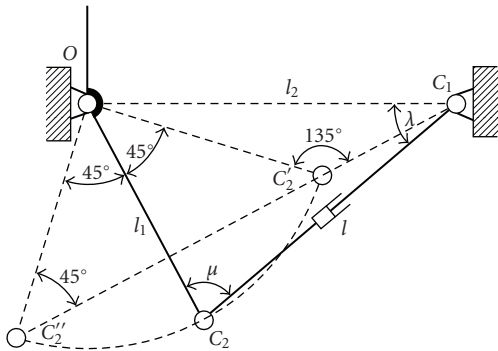


FIGURE 15: The rotational capability of the extensible link mechanism when $\mu \in (45^\circ, 135^\circ)$.

Please note that since all design conditions cannot be the same, the identification of an optimum region is up to the designer. Here, we just give an example.

For the slider-crank mechanism, an optimum region Ω will be determined with respect to the constraints of $W_{\omega_GTW} \geq 100^\circ$ and better GTI, for example, $\Gamma > 0.92$. This region is shown as the hatched parts in the parameter design space in Figure 18, where the region is divided two parts.

The identified optimum region contains all possible nondimensional solutions for the design problem. Since a nondimensional robot in the parameter design space and all of its corresponding dimensional mechanisms are similar in performance [20], the final design result based on the mechanism in the optimum region will be optimal. Therefore, the next step is to find an acceptable solution candidate in the optimum region.

Step 2. Selection of a solution candidate from the optimum region.

The obtained optimum region Ω contains all possible solutions for the design. Since there is no best but only a comparatively better solution for a design problem, one may pick up any nondimensional robot from the region.

We here pick up the nondimensional robot with parameters $r_1 = 1.5$, $r_2 = 0.65$, and $r_3 = 0.85$ from the optimum region Ω . For the selected robot, there are $W_{\omega_GTW} = 102.7^\circ$ and $\Gamma = 0.9347$. The orientation range for the robot is defined by $\omega_{min} = -69.5^\circ$ and $\omega_{max} = 33.2^\circ$.

Step 3. Determination of the dimensional parameters R_1 , R_2 , and R_3 with respect to the desired workspace.

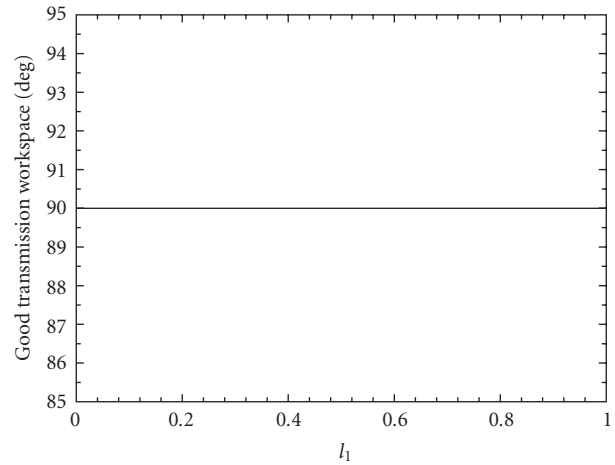


FIGURE 16: The relationship between the *good transmission workspace* (GTW) and l_1 .

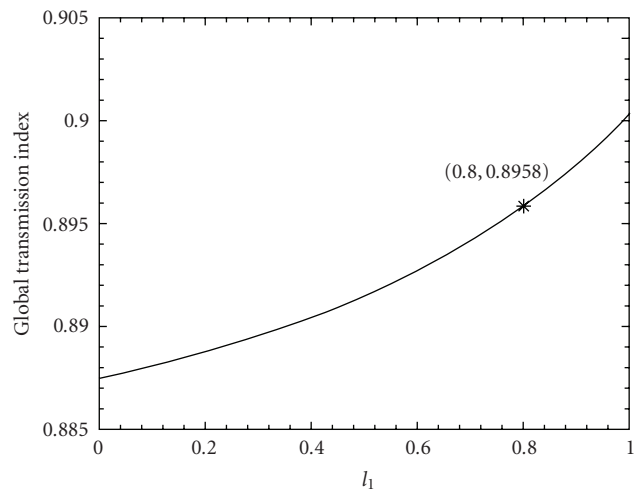


FIGURE 17: The relationship between the *good transmission index* (GTI) and l_1 .

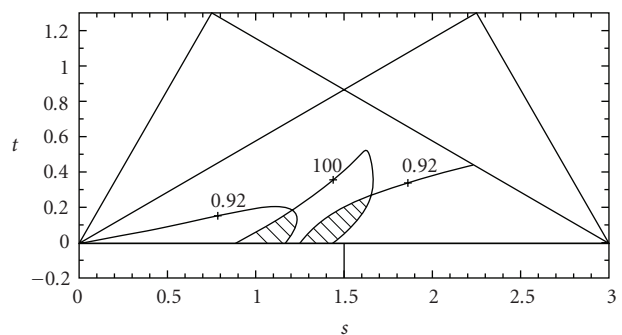


FIGURE 18: An optimum region for the slider-crank mechanism when $W_{\omega_GTW} \geq 100^\circ$ and $\Gamma > 0.92$.

According to the normalization method introduced in [20, 31], we should first determine the normalization factor, that is, D . This factor can be obtained by comparing the desired workspace of a design problem and the workspace of the nondimensional mechanism selected from the optimum region.

For the slider-crank mechanism, the output angle is only dependent on the ratio of related linear parameters but not on any one of the parameters itself, we cannot determine the normalization factor D with respect to the orientational workspace $\pm 50^\circ$. In this case, we should first determine the parameter R_1 of the mechanism according to the practical application and let the parameter be as small as possible for reducing the occupation space of the manipulator. Here, we take $R_1 = 150$ mm, for example. There are $D = R_1/r_1 = 100$, $R_2 = Dr_2 = 65$ mm, and $R_3 = Dr_3 = 85$ mm.

Step 4. Calculation of the input range and adjusting angle.

The input range to reach the desired workspace can be calculated by means of the inverse kinematic equations (9) and (10). In Step 2, we have got $\omega_{\min} = -69.5^\circ$ and $\omega_{\max} = 33.2^\circ$, please note that ω_{\min} and ω_{\max} are not symmetric about zero, and to make the output angle is α (shown in Figure 6) bilateral symmetry about O - yz plane, we choose the adjusting angle $\varepsilon_1 = 90^\circ + (\omega_{\min} + \omega_{\max})/2 \approx 72^\circ$. Then, when the output angle $\alpha = \pm 50^\circ$, $\omega \in (-68^\circ, 32^\circ)$ and the input range for the actuator is $z \in [-76.92$ mm, -181.44 mm].

Step 5. Checking the design result and adjusting, if necessary, the design solution.

In this step, what should be checked depends on the application. For example, the designer may check whether the input range is suitable for his preferred commercial actuator. Whatever is checked, if the solution is not satisfactory, the designer can return to Step 2 and pick up another nondimensional mechanism, or even return to Step 1 to identify another optimum region, adjusting the design solution until the solution is satisfactory. This is actually the advantage of this design method.

Similarly, we still pick up the nondimensional robot with parameters $r_1 = 1.5$, $r_2 = 0.65$, and $r_3 = 0.85$ from the optimum region Ω . According to the practical problem, the geometric parameters of the second leg can be got as $D_1 = 120$ mm, $D_2 = 52$ mm, and $D_3 = R = 68$ mm.

Then, the adjusting angle is $\varepsilon_2 = 162^\circ$. When the output angle is $\beta = \pm 50^\circ$, the input range for the actuator is $y \in [-104.72$ mm, 19.53 mm].

For the case II shown in Figure 4, the optimization process and the parameters of the first leg are identified with those in the case I. For the second leg, we pick up the nondimensional robot with parameters $l_1 = 0.8$ and $l_2 = 1.2$ as shown in Figures 16 and 17. From the two atlases, we can see that $W_{\omega-gtw} = 90^\circ$ and $\Gamma = 0.8958$. To compare it with the second leg in the case I, we take $L_1 = 52$ mm and $L_2 = 78$ mm, for example. Then, the adjusting angle is $\varepsilon_3 = 152^\circ$ and the output angle is $\beta = \pm 45^\circ$. The specified information is shown in Figure 19.

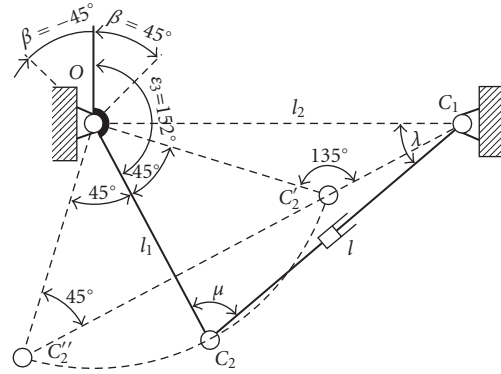


FIGURE 19: The second leg in the case II.

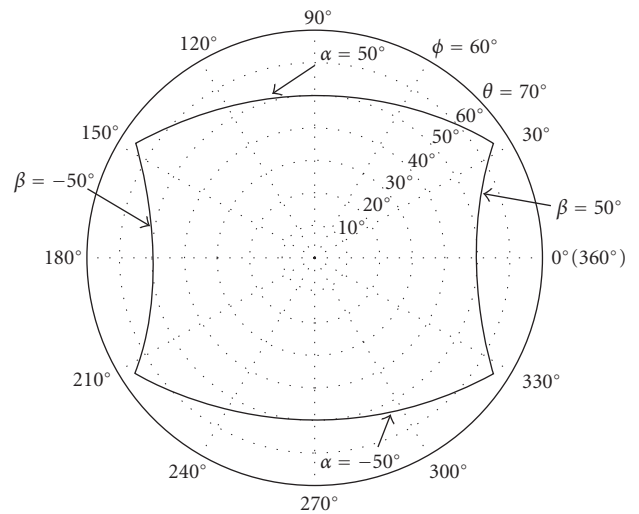


FIGURE 20: The orientation workspace of the tool head in the case I.

6. Orientation Capability and Parasitic Motions Analysis

In Section 3, we have introduced the method of orientation description of the tool head. In this section, we will investigate the relationship between the *azimuth and tilt angles* and the *good transmission workspace* of the designed tool head in Section 5.

We can get the output angles (α and β) of the first and second legs from (3).

For the case I, as analyzed in Section 5.4, the good transmission workspace is $\alpha = \pm 50^\circ$ and $\beta = \pm 50^\circ$. The orientation workspace of the tool head is shown in Figure 20.

The parasitic motions can be got from (4). In order to know the relationship between the orientation angles and the parasitic motions, we need first to find out the relationship between the orientation angles and the output angle α of the first leg, as shown in Figure 21. Figure 22 shows the relationship between the orientation angles and the output angle α . Then, from Figures 21 and 22, we can clearly know how the parasitic motions are.

For the case II, as analyzed in Section 5.4, the good transmission workspace can be described as $\alpha = \pm 50^\circ$ and

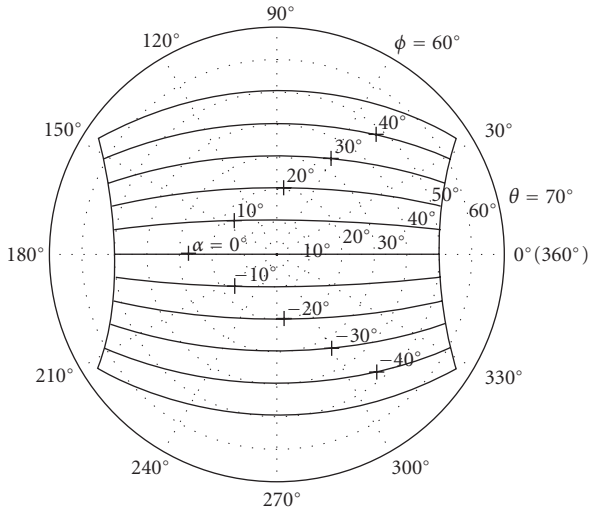


FIGURE 21: The relationship between the orientation angles and the output angle α of the first leg in the case I.

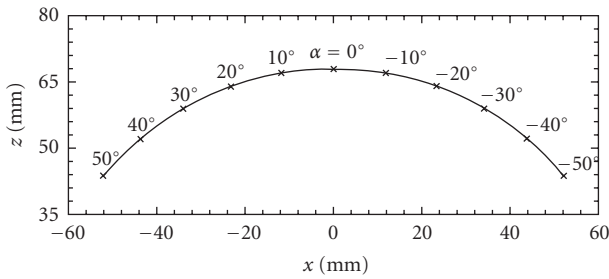


FIGURE 22: The relationship between parasitic motions and the output angle α of the first leg in the case I.

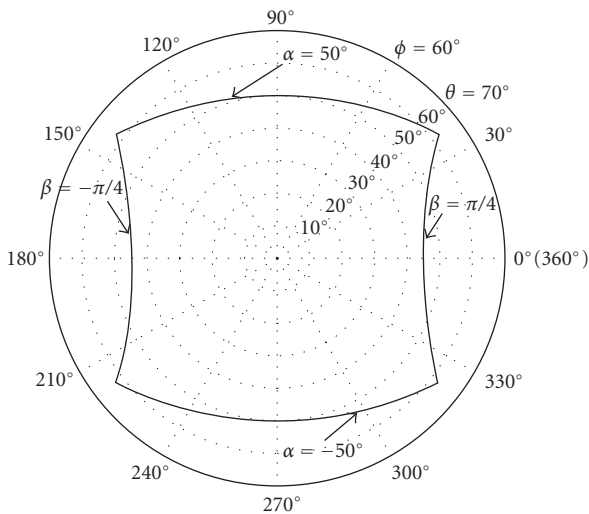


FIGURE 23: The orientation workspace of the tool head in the case II.

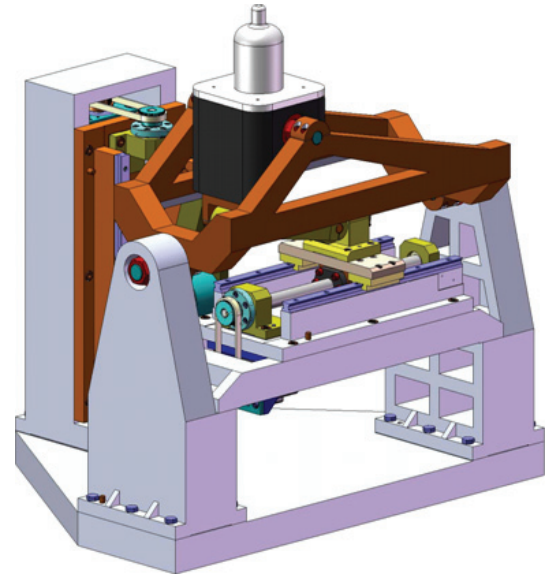


FIGURE 24: The real model of the mechanism in the case I.

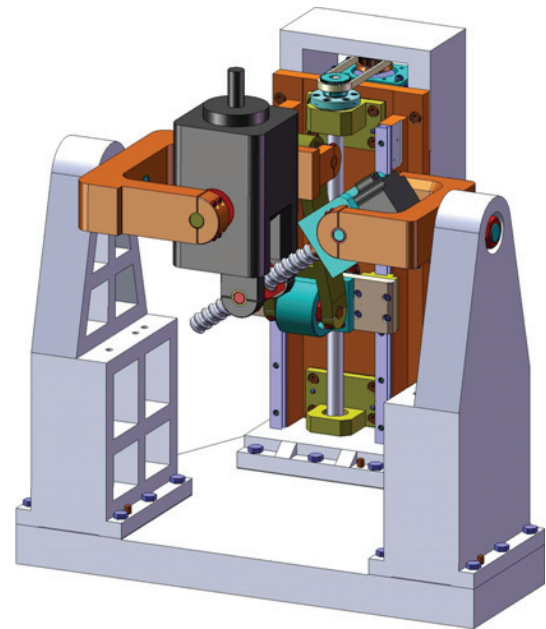


FIGURE 25: The real model of the mechanism in the case II.

$\beta = \pm 45^\circ$. Similarly, we can get the orientation workspace of the tool head as shown in Figure 23.

7. Development of the Tool Head

We have built the real model of this kind of mechanism, as shown in Figures 24 and 25 and may have them manufactured and carry out some experiments further.

8. Conclusion

In this paper, we have introduced and analyzed an A/B-axis tool head with parallel kinematics, which is kinematically decoupled. Firstly, we have introduced a method of orientation description of the tool head, that is, the *azimuth and tilt angles*. Then, the *transmission angle* was recalled and the *forward and inverse transmission angles* were defined accordingly. Based on the concept of *transmission angle*, we proposed and defined some new indices, that is, *local transmission index (LTI)*, *good transmission workspace (GTW)*, and *global transmission index (GTI)*. Then, the performance atlases and optimal design of the tool head based on these indices are presented. Finally, we analyzed the orientation capability and the parasitic motions of the designed tool head. The results show that the *azimuth and tilt angles* are convenient to describe the orientation of the tool head discussed here, and the indices proposed in this paper have obvious physical significance and could be extended to the analysis and design of other parallel robots.

Acknowledgments

This work was supported in part by the National Natural Science Foundation of China under Grant 50775118, the National Basic Research Program (973 Program) of China (no. 2007CB714000), and by Program for New Century Excellent Talents in the University of China.

References

- [1] W. Peng, B. J. Liu, S. J. Yao, and W. T. Ben, "Two Articulated Tool Head with embedded configuration," patent no. CN2644086, 2004.
- [2] J. Wahl, "Articulated Tool Head," WIPO patent no. WO 00/25976, 2000.
- [3] A. J. S. Fernandez, V. C. Jimenez, and M. G. Olazabal, "Kinematical System for a Movable Platform of a Machine," European patent no. EP1245349(A1), 2002.
- [4] C. Gosselin and J. Angeles, "Optimum kinematic design of a spherical three-degree-of-freedom parallel manipulator," *Journal of Mechanisms, Transmissions, and Automation in Design*, vol. 111, no. 2, pp. 202–207, 1989.
- [5] E. Ottaviano and M. Ceccarelli, "Optimal design of CaPaMan (Cassino Parallel Manipulator) with a specified orientation workspace," *Robotica*, vol. 20, no. 2, pp. 159–166, 2002.
- [6] D. Chablat and P. Wenger, "Architecture optimization of a 3-DoF translational parallel mechanism for machining applications, the orthoglide," *IEEE Transactions on Robotics and Automation*, vol. 19, no. 3, pp. 403–410, 2003.
- [7] X.-J. Liu, "Optimal kinematic design of a three translational DoFs parallel manipulator," *Robotica*, vol. 24, no. 2, pp. 239–250, 2006.
- [8] J. P. Merlet, "Jacobian, manipulability, condition number, and accuracy of parallel robots," *Journal of Mechanical Design*, vol. 128, no. 1, pp. 199–206, 2006.
- [9] X.-J. Liu, "Optimal kinematic design of a three translational DoFs parallel manipulator," *Robotica*, vol. 24, no. 2, pp. 239–250, 2006.
- [10] Y. J. Lou, G. F. Liu, N. Chen, and Z. X. Li, "Optimal design of parallel manipulators for maximum effective regular workspace," in *Proceedings of IEEE/RSJ International Conference on Intelligent Robots and Systems*, pp. 1208–1213, Edmonton, Canada, August 2005.
- [11] V. H. Alt, "Der ubertragungswinkel und seine bedeutung fur dar konstruieren periodischer getriebe," *Werksstattstechnik*, vol. 26, no. 4, pp. 61–65, 1932.
- [12] S. S. Balli and S. Chand, "Transmission angle in mechanisms (Triangle in mech)," *Mechanism and Machine Theory*, vol. 37, no. 2, pp. 175–195, 2002.
- [13] J. T. Kimbrell, *Kinematics Analysis and Synthesis*, McGraw-Hill, New York, NY, USA, 1991.
- [14] P. W. Eschenbach and D. Tesar, "Link length bounds on the four-bar chain," *Transactions of the ASME, Journal of Engineering for Industry, Series B*, vol. 93, no. 1, pp. 286–293, 1971.
- [15] A. S. Hall, *Kinematics and Linkage Design*, Prentice-Hall, Englewood Cliffs, NJ, USA, 1961.
- [16] G. H. Sutherland and J. N. Siddall, "Dimensional synthesis of linkages by multifactor optimization," *Mechanism and Machine Theory*, vol. 9, no. 1, pp. 81–95, 1974.
- [17] R. S. Hartenberg and J. Denavit, *Kinematic Synthesis of Linkages*, McGraw-Hill, New York, NY, USA, 1964.
- [18] D. C. Tao, *Applied Linkage Synthesis*, Addison-Wesley, Reading, Mass, USA, 1964.
- [19] X.-J. Liu, J. Wang, and G. Pritschow, "Kinematics, singularity and workspace of planar 5R symmetrical parallel mechanisms," *Mechanism and Machine Theory*, vol. 41, no. 2, pp. 145–169, 2006.
- [20] X.-J. Liu and J. Wang, "A new methodology for optimal kinematic design of parallel mechanisms," *Mechanism and Machine Theory*, vol. 42, no. 9, pp. 1210–1224, 2007.
- [21] X.-J. Liu and I. A. Bonev, "Orientation capability, error analysis, and dimensional optimization of two articulated tool heads with parallel kinematics," *Journal of Manufacturing Science and Engineering*, vol. 130, no. 1, Article ID 011015, 9 pages, 2008.
- [22] K. Hain, *Applied Kinematics*, McGraw-Hill, New York, NY, USA, 1967.
- [23] K. H. Pittens and R. P. Podhorodeski, "Family of Stewart platforms with optimal dexterity," *Journal of Robotic Systems*, vol. 10, no. 4, pp. 463–479, 1993.
- [24] R. S. Stoughton and T. Arai, "Modified Stewart platform manipulator with improved dexterity," *IEEE Transactions on Robotics and Automation*, vol. 9, no. 2, pp. 166–172, 1993.
- [25] P. A. Voglewede and I. Ebert-Uphoff, "Measuring "closeness" to singularities for parallel manipulators," in *Proceedings of IEEE International Conference on Robotics and Automation (ICRA '04)*, pp. 4539–4544, Orleans, La, USA, April-May 2004.
- [26] H. Funabashi and Y. Takeda, "Determination of singular points and their vicinity in parallel manipulators based on the transmission index," in *Proceedings of the 9th World Congress on the Theory of Machines and Mechanisms*, pp. 1977–1981, Milan, Italy, August-September 1995.
- [27] D. Chablat, P. Wenger, and J.-P. Merlet, "Workspace analysis of the orthoglide using interval analysis," in *Proceedings of International Symposium on Advances in Robot Kinematics*, pp. 397–406, Caldes de Malavalla, Spain, June 2002.

- [28] G. Sutherland and B. Roth, "A transmission index for spatial mechanism," *Transactions of the ASME, Journal of Engineering for Industry*, pp. 589–597, 1973.
- [29] Y. Takeda, H. Funabashi, and H. Ichimaru, "Development of spatial in-parallel actuated manipulators with six degrees of freedom with high motion transmissibility," *JSME International Journal, Series C*, vol. 40, no. 2, pp. 299–308, 1997.
- [30] C. Gosselin and J. Angeles, "Global performance index for the kinematic optimization of robotic manipulators," *Journal of Mechanisms, Transmissions, and Automation in Design*, vol. 113, no. 3, pp. 220–226, 1991.
- [31] X.-J. Liu, J. Wang, and G. Pritschow, "On the optimal kinematic design of the PRRRP 2-DoF parallel mechanism," *Mechanism and Machine Theory*, vol. 41, no. 9, pp. 1111–1130, 2006.

Research Article

Modeling of Configuration-Dependent Flexible Joints for a Parallel Robot

Zili Zhou,¹ Chris K. Mechefske,¹ and Fengfeng Xi²

¹Department of Mechanical and Materials Engineering, Queen's University, Kingston, ON, Canada K7L 3N6

²Department of Aerospace Engineering, Ryerson University, Toronto, ON, Canada M5B 2K3

Correspondence should be addressed to Chris K. Mechefske, chrism@me.queensu.ca

Received 7 November 2008; Revised 13 April 2009; Accepted 12 July 2009

Academic Editor: Zhen Huang

Copyright © 2010 Zili Zhou et al. This is an open access article distributed under the Creative Commons Attribution License, which permits unrestricted use, distribution, and reproduction in any medium, provided the original work is properly cited.

This paper provides a method to determine the variable flexible joint parameters which are dependent on configurations for a PRS Parallel Robot. Based on the continuous force approach, virtual springs were used between the joint components to simulate the joint flexibility. The stiffness matrix of the joint virtual springs was derived. The method uses system dynamic characteristics in different configurations to set the virtual spring stiffness for all the joints in the system. Modal testing was conducted on a set of selected robot configurations to determine the system natural frequencies and mode shapes along with their variation. To obtain the virtual spring stiffness, the system was condensed at the joint nodal coordinates. Then eigen-sensitivity analysis was conducted on the condensed system matrices with respect to the stiffness parameters of the joint virtual springs. Thus, the virtual spring parameters in the model can be set to match the variation of the system dynamic responses with the robot configuration changes. The virtual spring parameters between the selected robot configurations were obtained by interpolation. The research indicates that the method is effective and relatively easy to conduct, compared to other methods. The variable flexible joint model is applicable to flexible multibody systems with variable configurations.

1. Introduction

Dynamic modeling of flexible multibody systems is a classical problem. The link flexibility and joint compliance (elasticity) of robots or mechanisms in general have been studied for a long time. This paper focuses on the difficult issue of joint flexibility which varies due to system configuration changes. Joint flexibility has been studied since the 1980s, mainly by relating it to contact/impact mechanics. Tzou et al. [1] proposed a stochastic approach to model the random feature of the dynamic contacts in the joints. Bowden and Dugundji [2] presented the linear and nonlinear analysis for the global dynamics of jointed structures. Moon and Li [3] conducted an experimental study on a pin-jointed truss. Tzou and Rong [4] provided a mathematical model for a three-dimensional spherical joint based on the contact force analysis. Kakizaki et al. [5] presented a dynamic modeling method for a SCARA manipulator with link flexibility and joint clearances. Seneviratne et al. [6] provided a combined massless-link and spring-damping model for modeling the

joint clearance. Ravn et al. [7] presented the analysis of revolute joint clearances with and without lubricant. Schwab et al. [8] presented a study on the dynamic response of mechanisms affected by the joint clearance. Ting et al. [9] presented a novel and simple approach to identify the worst position and direction errors due to the joint clearance of a single loop linkage. Zhu and Ting [10] studied the uncertainty of planar and spatial robots with joint clearances. Wang et al. [11] presented the virtual spring method at joints to completely decouple the dynamic model of complex robotic systems with closed kinematic chains.

In the above investigations, two basic approaches were used in the dynamics of flexible joint systems. The first approach uses an impulse momentum model, where the pieced intervals are analyzed. The impulse momentum equations can be solved with the restitution condition for the jump discontinuity in the system velocities and the joint reaction forces. The second approach uses a continuous force model to represent the force of interaction between the impact surfaces. Stiffness and damping coefficients are set

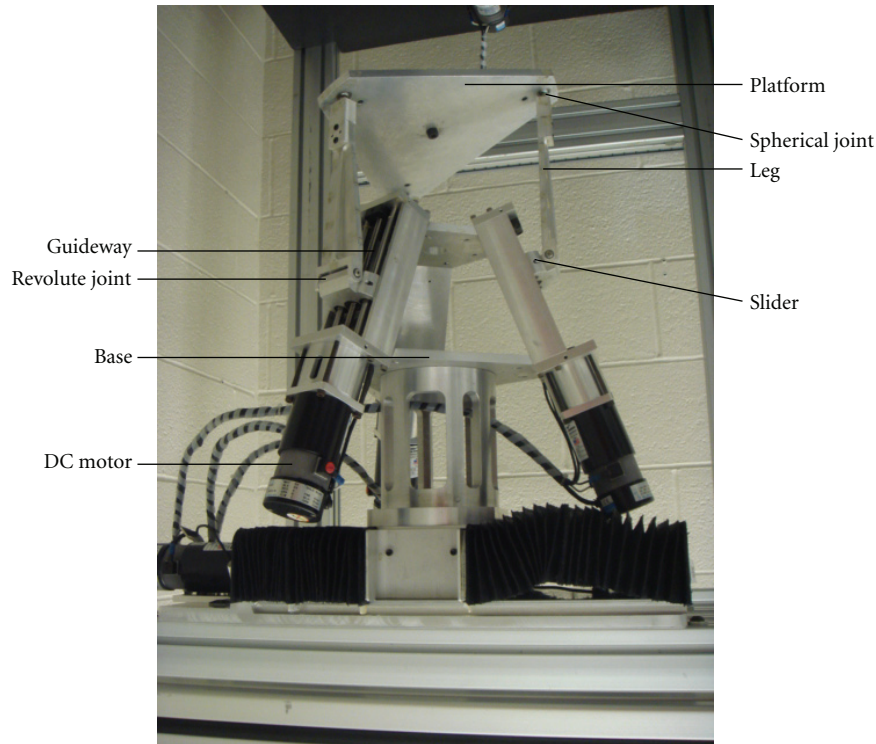


FIGURE 1: The Parallel Robot Prototype.

to account for the impact surface compliance and energy dissipation during the impact process. Obviously, the second approach is easier to handle than the first. No matter which method is used, a key step is to determine the parameters in the joint models. Though the above models are effective to different extents when used to represent the physics of an individual joint in a configuration-fixed system, they are difficult to use for multiple joints assembled together in a configuration-variable system (such as a robot). The difficulty is that the joint flexibility parameters may change when the system configuration changes. Also, the parameters may be different for the same type of joints at different locations in a system. It is the highlight for this paper to display how to set the flexibility parameters for multiple joints in a system with variable configuration.

Based on the continuous force model, this paper presents a modeling method on the joint whose flexibility results from the variable joint looseness due to the system configuration change. The flexible joint model was used in the simulation of a PRS parallel robot shown in Figure 1. Instead of studying the joint individually, the method uses system dynamic characteristics to set the flexibility parameters for all the joints in the system. Experimental modal testing was conducted at a set of selected robot configurations to determine the variation of the system natural frequencies and mode shapes. To easily obtain the joint flexibility parameters, the system was condensed at the joint coordinates. At each selected robot configuration, eigen-sensitivity analysis was conducted on the condensed system matrices with respect

to the joint flexibility parameters. Thus, the joint flexibility parameters in the model can be updated at each selected robot configuration to be consistent with the variation of the system dynamic responses. The joint flexibility parameters between the selected configurations were obtained by interpolation.

2. Flexible Joint Model

Figure 2 shows the system model of a PRS parallel robot, where $OXYZ$ is the global reference, ${}^P O {}^P X {}^P Y {}^P Z$ is the platform body reference, and ${}^l O {}^l X {}^l Y {}^l Z$ is the leg body reference, $l = 1, 2, 3$. As a continuous force model, all the joint constraints are released and replaced by virtual springs and virtual dampers correspondingly, except for the rotational constraint around ${}^l Z$ in the revolute joints. Figures 3(a) and 3(b) show the flexible revolute joint model and the related coordinate system, where $k_{1/l}$, $k_{2/l}$, $k_{3/l}$, and $k_{4/l}$ are the stiffness parameters of the virtual springs at the revolute joints in their original constrained directions: along ${}^l X$, ${}^l Y$, ${}^l Z$, and around ${}^l X$, respectively, $l = 1, 2, 3$. Similarly (not shown), let $k_{5/l}$, $k_{6/l}$, and $k_{7/l}$ be the stiffness parameters of the virtual springs at the spherical joints in the directions of the leg body reference ${}^l O {}^l X {}^l Y {}^l Z$: along ${}^l X$, ${}^l Y$, and ${}^l Z$, respectively, $l = 1, 2, 3$. Altogether there are 21 stiffness parameters of the joint virtual springs, or simply called joint stiffness parameters, in the robot system model. In the revolute joint, the rotational constraint around ${}^l Z$ (leg axis in undeformed state) is still kept, because releasing of

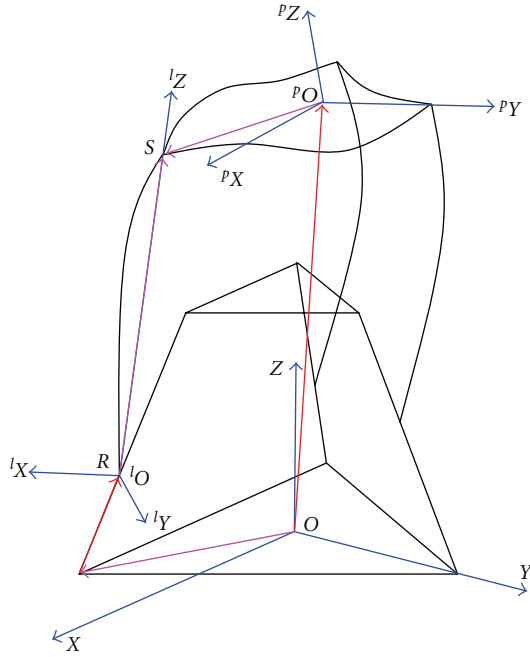


FIGURE 2: Parallel Robot System Model.

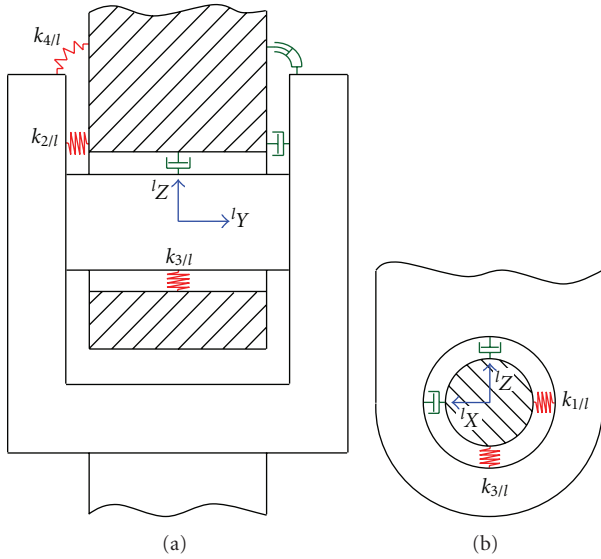


FIGURE 3: (a) Flexible Revolute Joint Model (axial-section view). (b) Flexible Revolute Joint Model (cross-section view).

this constraint is kinematically meaningless for the tripod motion (configuration determining), and the kinetic energy of this rotation is small enough to omit (compared to the rotation around lX).

In this case it is recognized that the special revolute joint (not related to the leg body) is not a “general” revolute joint even for the flexible case, and so the symbol “R” in the phrase “PRS parallel robot” may not seem perfectly suitable. Rather than use a special symbol (such as R'), we have maintained the use of R in order to reduce unnecessary confusion. For

simplicity, this research considers the joint virtual dampers with modal damping in the entire system; only the joint virtual springs are modeled here.

The potential energy of the joint virtual springs in the l th branch can be originally written as

$$\begin{aligned} {}^jU_l = & \frac{1}{2}k_{1/l} {}^l u_R^2 + \frac{1}{2}k_{2/l} {}^l v_R^2 + \frac{1}{2}k_{3/l} {}^l w_R^2 \\ & + \frac{1}{2}k_{4/l} {}^l \varphi_R^2 + \frac{1}{2}k_{5/l} ({}^l u_S - {}^p u_{S/l})^2 \\ & + \frac{1}{2}k_{6/l} ({}^l v_S - {}^p v_{S/l})^2 + \frac{1}{2}k_{7/l} ({}^l w_S - {}^p w_{S/l})^2, \end{aligned} \quad (1)$$

where ${}^l u_R$, ${}^l v_R$, ${}^l w_R$, and ${}^l \varphi_R$ are the nodal coordinates of the leg at the revolute joint of the l th branch along lX , lY , lZ , and about lX directions, respectively; ${}^l u_S$, ${}^l v_S$, and ${}^l w_S$ are the nodal coordinates of the leg at the spherical joint of the l th branch along lX , lY , and lZ directions, respectively; ${}^p u_{S/l}$, ${}^p v_{S/l}$, and ${}^p w_{S/l}$ are the nodal coordinate projections in leg body reference ${}^lO {}^lX {}^lY {}^lZ$ from ${}^p u_{S/l}$, ${}^p v_{S/l}$, and ${}^p w_{S/l}$, the nodal coordinates of the platform at the spherical joint of the l th branch along pX , pY , and pZ directions, respectively, and the projections can be calculated as

$$\begin{aligned} & \begin{bmatrix} {}^p u_{S/l} & {}^p v_{S/l} & {}^p w_{S/l} \end{bmatrix}^T \\ & = [{}^l \mathbf{R}]^T [{}^p \mathbf{R}] \begin{bmatrix} {}^p u_{S/l} & {}^p v_{S/l} & {}^p w_{S/l} \end{bmatrix}^T, \quad l = 1, 2, 3 \end{aligned} \quad (2)$$

in which $[{}^p \mathbf{R}]$ is the transformation matrix from platform body reference ${}^pO {}^pX {}^pY {}^pZ$ to global reference $OXYZ$, and $[{}^l \mathbf{R}]$ from leg body reference ${}^lO {}^lX {}^lY {}^lZ$ to global reference $OXYZ$. Substituting (2) into (1) leads to the matrix form

$${}^jU_l = \frac{1}{2} \{ {}^j \mathbf{q}_l \}^T [{}^j \mathbf{K}_l] \{ {}^j \mathbf{q}_l \}, \quad (3)$$

where $\{ {}^j \mathbf{q}_l \}$ are the associated joint nodal coordinates in the l th branch

$$\begin{aligned} & \{ {}^j \mathbf{q}_l \} \\ & = \begin{bmatrix} {}^l u_R & {}^l v_R & {}^l w_R & {}^l \varphi_R & {}^l u_S & {}^l v_S & {}^l w_S & {}^p u_{S/l} & {}^p v_{S/l} & {}^p w_{S/l} \end{bmatrix}^T \end{aligned} \quad (4)$$

and $[{}^j \mathbf{K}_l]$ is the joint stiffness matrix in the l th branch

$$[{}^j \mathbf{K}_l] = \begin{bmatrix} [{}^j \mathbf{K}_{R/l}] & \mathbf{0} & \mathbf{0} \\ \mathbf{0} & [{}^j \mathbf{K}_{S/l}] & -[{}^j \mathbf{K}_{S/l}] [{}^l \mathbf{R}]^T [{}^p \mathbf{R}] \\ \mathbf{0} & \mathfrak{A} & \mathfrak{B} \end{bmatrix}, \quad (5)$$

where \mathfrak{A} denotes $-[{}^p \mathbf{R}]^T [{}^l \mathbf{R}] [{}^j \mathbf{K}_{S/l}]$, and \mathfrak{B} denotes $[{}^p \mathbf{R}]^T [{}^l \mathbf{R}] [{}^j \mathbf{K}_{S/l}] [{}^l \mathbf{R}]^T [{}^p \mathbf{R}]$ in which $[{}^j \mathbf{K}_{R/l}]$ and $[{}^j \mathbf{K}_{S/l}]$ are the

revolute and spherical joint stiffness matrices, respectively, in the l th branch:

$$\begin{aligned} [{}^j\mathbf{K}_{R/l}] &= \begin{bmatrix} k_{1/l} & 0 & 0 & 0 \\ 0 & k_{2/l} & 0 & 0 \\ 0 & 0 & k_{3/l} & 0 \\ 0 & 0 & 0 & k_{4/l} \end{bmatrix}, \\ [{}^j\mathbf{K}_{S/l}] &= \begin{bmatrix} k_{5/l} & 0 & 0 \\ 0 & k_{6/l} & 0 \\ 0 & 0 & k_{7/l} \end{bmatrix}. \end{aligned} \quad (6)$$

The joint coordinates $\{{}^j\mathbf{q}_l\}$ in the l th branch can be expressed in terms of the system total nodal coordinates $\{\mathbf{q}\}$ by joint coordinate connectivity matrix $[{}^j\mathbf{N}_{c/l}]$:

$$\{{}^j\mathbf{q}_l\} = [{}^j\mathbf{N}_{c/l}]\{\mathbf{q}\}, \quad l = 1, 2, 3, \quad (7)$$

where the elements of matrix $[{}^j\mathbf{N}_{c/l}]$ are 1 and 0. Thus, by substituting (7) into (3), the system joint stiffness matrix $[{}^j\mathbf{K}]$ is obtained by summing the joint stiffness matrix $[{}^j\mathbf{K}_l]$ from all three branches:

$$[{}^j\mathbf{K}] = \sum_{l=1}^3 [{}^j\mathbf{N}_{c/l}]^T [{}^j\mathbf{K}_l] [{}^j\mathbf{N}_{c/l}]. \quad (8)$$

By writing the system potential energy, the system stiffness matrix $[\mathbf{K}]$ can be obtained as the summation of system link stiffness matrix $[{}^L\mathbf{K}]$ and system joint stiffness matrix $[{}^j\mathbf{K}]$, both associated with the system total nodal coordinates $\{\mathbf{q}\}$:

$$[\mathbf{K}] = [{}^L\mathbf{K}] + [{}^j\mathbf{K}]. \quad (9)$$

In (6), the joint stiffness parameters will be set variable to match the variation of the system dynamic responses at different configurations. Therefore, (5), (8), and (9) are variable matrices.

Using static condensation method given by Guyan [12], the condensed system stiffness matrix $[\mathbf{K}_m]$ and mass matrix $[\mathbf{M}_m]$ are obtained as follows:

$$\begin{aligned} [\mathbf{K}_m] &= [\mathbf{N}_m]^T [\mathbf{K}] [\mathbf{N}_m] \\ &\quad - [\mathbf{N}_m]^T [\mathbf{K}] [\mathbf{N}_s] \left([\mathbf{N}_s]^T [\mathbf{K}] [\mathbf{N}_s] \right)^{-1} \\ &\quad \cdot [\mathbf{N}_s]^T [\mathbf{K}] [\mathbf{N}_m], \end{aligned} \quad (10)$$

$$\begin{aligned} [\mathbf{M}_m] &= [\mathbf{N}_m]^T [\mathbf{M}] [\mathbf{N}_m] \\ &\quad - [\mathbf{N}_m]^T [\mathbf{M}] [\mathbf{N}_s] \left([\mathbf{N}_s]^T [\mathbf{K}] [\mathbf{N}_s] \right)^{-1} [\mathbf{N}_s]^T [\mathbf{K}] [\mathbf{N}_m] \\ &\quad - [\mathbf{N}_m]^T [\mathbf{K}] [\mathbf{N}_s] \left([\mathbf{N}_s]^T [\mathbf{K}] [\mathbf{N}_s] \right)^{-1} [\mathbf{N}_s]^T [\mathbf{M}] [\mathbf{N}_m] \\ &\quad + [\mathbf{N}_m]^T [\mathbf{K}] [\mathbf{N}_s] \left([\mathbf{N}_s]^T [\mathbf{K}] [\mathbf{N}_s] \right)^{-1} [\mathbf{N}_s]^T [\mathbf{M}] [\mathbf{N}_s] \\ &\quad \cdot \left([\mathbf{N}_s]^T [\mathbf{K}] [\mathbf{N}_s] \right)^{-1} [\mathbf{N}_s]^T [\mathbf{K}] [\mathbf{N}_m], \end{aligned} \quad (11)$$

where $[\mathbf{M}]$ is system mass matrix, and $[\mathbf{N}_m]$ and $[\mathbf{N}_s]$ are partitioning matrices with elements of 1 and 0 which divide system total nodal coordinates $\{\mathbf{q}\}$ as master coordinates $\{\mathbf{q}_m\}$, mainly consisted of the joint nodal coordinates, and slave coordinates $\{\mathbf{q}_s\}$ as follows:

$$\{\mathbf{q}\} = [\mathbf{N}_m]\{\mathbf{q}_m\} + [\mathbf{N}_s]\{\mathbf{q}_s\}. \quad (12)$$

The above $[\mathbf{K}_m]$ and $[\mathbf{M}_m]$ are associated with the master coordinates $\{\mathbf{q}_m\}$.

3. Eigen-Sensitivity on the Condensed System

According to Fox and Kapoor [13], the natural frequency sensitivity and mode shape sensitivity with respect to joint stiffness parameter $k_{b/l}$, $b = 1$ to 7, $l = 1$ to 3, can be respectively, derived on the condensed system as

$$\begin{aligned} \frac{\partial f_i}{\partial k_{b/l}} &= \frac{1}{8\pi^2 f_i} \{\Phi_i\}^T \left(\frac{\partial [\mathbf{K}_m]}{\partial k_{b/l}} - \omega_i^2 \frac{\partial [\mathbf{M}_m]}{\partial k_{b/l}} \right) \{\Phi_i\}, \quad (13) \\ \frac{\partial \{\Phi_i\}}{\partial k_{b/l}} &= -\frac{1}{2} \{\Phi_i\}^T \frac{\partial [\mathbf{M}_m]}{\partial k_{b/l}} \{\Phi_i\} \{\Phi_i\} \\ &\quad + \sum_{\substack{j=1 \\ j \neq i}}^n \frac{1}{\omega_i^2 - \omega_j^2} \{\Phi_i\}^T \left(\frac{\partial [\mathbf{K}_m]}{\partial k_{b/l}} - \omega_i^2 \frac{\partial [\mathbf{M}_m]}{\partial k_{b/l}} \right) \\ &\quad \cdot \{\Phi_j\} \{\Phi_j\}, \end{aligned} \quad (14)$$

where f_i is the i th natural frequency, $\{\Phi_i\}$ is the i th normalized mode shape vector, and $\omega_i = 2\pi f_i$. Using (9) and noticing that $[{}^L\mathbf{K}]$ and $[\mathbf{M}]$ are constant lead to

$$\begin{aligned} \frac{\partial [\mathbf{K}]}{\partial k_{b/l}} &= \frac{\partial [{}^j\mathbf{K}]}{\partial k_{b/l}} \\ \frac{\partial [\mathbf{M}]}{\partial k_{b/l}} &= [\mathbf{0}]. \end{aligned} \quad (15)$$

Therefore, the terms $\partial [\mathbf{K}_m] / \partial k_{b/l}$ and $\partial [\mathbf{M}_m] / \partial k_{b/l}$ in (13) and (14) can be calculated using (10) and (11) as

$$\begin{aligned} \frac{\partial [\mathbf{K}_m]}{\partial k_{b/l}} &= [\mathbf{N}_m]^T \frac{\partial [{}^j\mathbf{K}]}{\partial k_{b/l}} [\mathbf{N}_m] \\ &\quad - [\mathbf{N}_m]^T \frac{\partial [{}^j\mathbf{K}]}{\partial k_{b/l}} [\mathbf{N}_s] \left([\mathbf{N}_s]^T [\mathbf{K}] [\mathbf{N}_s] \right)^{-1} [\mathbf{N}_s]^T [\mathbf{K}] [\mathbf{N}_m] \\ &\quad - [\mathbf{N}_m]^T [\mathbf{K}] [\mathbf{N}_s] \left([\mathbf{N}_s]^T [\mathbf{K}] [\mathbf{N}_s] \right)^{-1} [\mathbf{N}_s]^T \frac{\partial [{}^j\mathbf{K}]}{\partial k_{b/l}} [\mathbf{N}_m] \\ &\quad + [\mathbf{N}_m]^T [\mathbf{K}] [\mathbf{N}_s] \left([\mathbf{N}_s]^T [\mathbf{K}] [\mathbf{N}_s] \right)^{-1} [\mathbf{N}_s]^T \frac{\partial [{}^j\mathbf{K}]}{\partial k_{b/l}} [\mathbf{N}_s] \\ &\quad \cdot \left([\mathbf{N}_s]^T [\mathbf{K}] [\mathbf{N}_s] \right)^{-1} [\mathbf{N}_s]^T [\mathbf{K}] [\mathbf{N}_m], \end{aligned} \quad (16)$$

$$\begin{aligned}
& \frac{\partial[\mathbf{M}_m]}{\partial k_{b/l}} \\
&= [\mathbf{N}_m]^T [\mathbf{M}] [\mathbf{N}_s] \left([\mathbf{N}_s]^T [\mathbf{K}] [\mathbf{N}_s] \right)^{-1} [\mathbf{N}_s]^T \frac{\partial[{}^J\mathbf{K}]}{\partial k_{b/l}} [\mathbf{N}_s] \\
&\quad \cdot \left([\mathbf{N}_s]^T [\mathbf{K}] [\mathbf{N}_s] \right)^{-1} [\mathbf{N}_s]^T [\mathbf{K}] [\mathbf{N}_m] \\
&\quad - [\mathbf{N}_m]^T [\mathbf{M}] [\mathbf{N}_s] \left([\mathbf{N}_s]^T [\mathbf{K}] [\mathbf{N}_s] \right)^{-1} [\mathbf{N}_s]^T \frac{\partial[{}^J\mathbf{K}]}{\partial k_{b/l}} [\mathbf{N}_m] \\
&\quad + [\mathbf{N}_m]^T [\mathbf{K}] [\mathbf{N}_s] \left([\mathbf{N}_s]^T [\mathbf{K}] [\mathbf{N}_s] \right)^{-1} [\mathbf{N}_s]^T \frac{\partial[{}^J\mathbf{K}]}{\partial k_{b/l}} [\mathbf{N}_s] \\
&\quad \cdot \left([\mathbf{N}_s]^T [\mathbf{K}] [\mathbf{N}_s] \right)^{-1} [\mathbf{N}_s]^T [\mathbf{M}] [\mathbf{N}_m] \\
&\quad - [\mathbf{N}_m]^T \frac{\partial[{}^J\mathbf{K}]}{\partial k_{b/l}} [\mathbf{N}_s] \left([\mathbf{N}_s]^T [\mathbf{K}] [\mathbf{N}_s] \right)^{-1} [\mathbf{N}_s]^T [\mathbf{M}] [\mathbf{N}_m] \\
&\quad + [\mathbf{N}_m]^T \frac{\partial[{}^J\mathbf{K}]}{\partial k_{b/l}} [\mathbf{N}_s] \left([\mathbf{N}_s]^T [\mathbf{K}] [\mathbf{N}_s] \right)^{-1} [\mathbf{N}_s]^T [\mathbf{M}] [\mathbf{N}_s] \\
&\quad \cdot \left([\mathbf{N}_s]^T [\mathbf{K}] [\mathbf{N}_s] \right)^{-1} [\mathbf{N}_s]^T [\mathbf{K}] [\mathbf{N}_m] \\
&\quad - [\mathbf{N}_m]^T [\mathbf{K}] [\mathbf{N}_s] \left([\mathbf{N}_s]^T [\mathbf{K}] [\mathbf{N}_s] \right)^{-1} [\mathbf{N}_s]^T \frac{\partial[{}^J\mathbf{K}]}{\partial k_{b/l}} \\
&\quad \cdot [\mathbf{N}_s] \left([\mathbf{N}_s]^T [\mathbf{K}] [\mathbf{N}_s] \right)^{-1} \\
&\quad \cdot [\mathbf{N}_s]^T [\mathbf{M}] [\mathbf{N}_s] \left([\mathbf{N}_s]^T [\mathbf{K}] [\mathbf{N}_s] \right)^{-1} [\mathbf{N}_s]^T [\mathbf{K}] [\mathbf{N}_m] \\
&\quad + [\mathbf{N}_m]^T [\mathbf{K}] [\mathbf{N}_s] \left([\mathbf{N}_s]^T [\mathbf{K}] [\mathbf{N}_s] \right)^{-1} [\mathbf{N}_s]^T [\mathbf{M}] [\mathbf{N}_s] \\
&\quad \cdot \left([\mathbf{N}_s]^T [\mathbf{K}] [\mathbf{N}_s] \right)^{-1} [\mathbf{N}_s]^T \frac{\partial[{}^J\mathbf{K}]}{\partial k_{b/l}} [\mathbf{N}_m] \\
&\quad - [\mathbf{N}_m]^T [\mathbf{K}] [\mathbf{N}_s] \left([\mathbf{N}_s]^T [\mathbf{K}] [\mathbf{N}_s] \right)^{-1} [\mathbf{N}_s]^T [\mathbf{M}] [\mathbf{N}_s] \\
&\quad \cdot \left([\mathbf{N}_s]^T [\mathbf{K}] [\mathbf{N}_s] \right)^{-1} \\
&\quad \cdot [\mathbf{N}_s]^T \frac{\partial[{}^J\mathbf{K}]}{\partial k_{b/l}} [\mathbf{N}_s] \left([\mathbf{N}_s]^T [\mathbf{K}] [\mathbf{N}_s] \right)^{-1} [\mathbf{N}_s]^T [\mathbf{K}] [\mathbf{N}_m].
\end{aligned} \tag{17}$$

In light of (8), the term $\partial[{}^J\mathbf{K}]/\partial k_{b/l}$ in (16) and (17) is

$$\begin{aligned}
\frac{\partial[{}^J\mathbf{K}]}{\partial k_{b/l}} &= \frac{\partial}{\partial k_{b/l}} \sum_{l=1}^3 [{}^j\mathbf{N}_{c/l}]^T [{}^j\mathbf{K}_l] [{}^j\mathbf{N}_{c/l}] \\
&= [{}^j\mathbf{N}_{c/l}]^T \frac{\partial[{}^j\mathbf{K}_l]}{\partial k_{b/l}} [{}^j\mathbf{N}_{c/l}], \quad b = 1 \text{ to } 7; l = 1, 2, 3,
\end{aligned} \tag{18}$$

where $\partial[{}^j\mathbf{K}_l]/\partial k_{b/l}$ can be calculated using (5) as

$$\frac{\partial[{}^j\mathbf{K}_l]}{\partial k_{b/l}} = \begin{bmatrix} \frac{\partial[{}^j\mathbf{K}_{R/l}]}{\partial k_{b/l}} & \mathbf{0} & \mathbf{0} \\ \mathbf{0} & \frac{\partial[{}^j\mathbf{K}_{S/l}]}{\partial k_{b/l}} & -\frac{\partial[{}^j\mathbf{K}_{S/l}]}{\partial k_{b/l}} [{}^l\mathbf{R}]^T [{}^p\mathbf{R}] \\ \mathbf{0} & \mathfrak{C} & \mathfrak{D} \end{bmatrix}, \tag{19}$$

where \mathfrak{C} denotes $-[{}^p\mathbf{R}]^T [{}^l\mathbf{R}] (\partial[{}^j\mathbf{K}_{S/l}]/\partial k_{b/l})$, and \mathfrak{D} denotes $[{}^p\mathbf{R}]^T [{}^l\mathbf{R}] (\partial[{}^j\mathbf{K}_{S/l}]/\partial k_{b/l}) [{}^l\mathbf{R}]^T [{}^p\mathbf{R}]$ in which, by using (6) and (7), the differentials of the revolute and spherical joint stiffness matrices with respect to the joint stiffness parameters in the l th branch are

$$\begin{aligned}
\frac{\partial[{}^j\mathbf{K}_{R/l}]}{\partial k_{1/l}} &= \begin{bmatrix} 1 & 0 & 0 & 0 \\ 0 & 0 & 0 & 0 \\ 0 & 0 & 0 & 0 \\ 0 & 0 & 0 & 0 \end{bmatrix}, \\
\frac{\partial[{}^j\mathbf{K}_{R/l}]}{\partial k_{2/l}} &= \begin{bmatrix} 0 & 0 & 0 & 0 \\ 0 & 1 & 0 & 0 \\ 0 & 0 & 0 & 0 \\ 0 & 0 & 0 & 0 \end{bmatrix}, \\
\frac{\partial[{}^j\mathbf{K}_{R/l}]}{\partial k_{3/l}} &= \begin{bmatrix} 0 & 0 & 0 & 0 \\ 0 & 0 & 0 & 0 \\ 0 & 0 & 1 & 0 \\ 0 & 0 & 0 & 0 \end{bmatrix}, \\
\frac{\partial[{}^j\mathbf{K}_{R/l}]}{\partial k_{4/l}} &= \begin{bmatrix} 0 & 0 & 0 & 0 \\ 0 & 0 & 0 & 0 \\ 0 & 0 & 0 & 0 \\ 0 & 0 & 0 & 1 \end{bmatrix}, \\
\frac{\partial[{}^j\mathbf{K}_{R/l}]}{\partial k_{5/l}} &= \frac{\partial[{}^j\mathbf{K}_{R/l}]}{\partial k_{6/l}} = \frac{\partial[{}^j\mathbf{K}_{R/l}]}{\partial k_{7/l}} = [\mathbf{0}]_{4 \times 4}, \\
\frac{\partial[{}^j\mathbf{K}_{S/l}]}{\partial k_{1/l}} &= \frac{\partial[{}^j\mathbf{K}_{S/l}]}{\partial k_{2/l}} = \frac{\partial[{}^j\mathbf{K}_{S/l}]}{\partial k_{3/l}} = \frac{\partial[{}^j\mathbf{K}_{S/l}]}{\partial k_{4/l}} = [\mathbf{0}]_{3 \times 3}, \\
\frac{\partial[{}^j\mathbf{K}_{S/l}]}{\partial k_{5/l}} &= \begin{bmatrix} 1 & 0 & 0 \\ 0 & 0 & 0 \\ 0 & 0 & 0 \end{bmatrix}, \\
\frac{\partial[{}^j\mathbf{K}_{S/l}]}{\partial k_{6/l}} &= \begin{bmatrix} 0 & 0 & 0 \\ 0 & 1 & 0 \\ 0 & 0 & 0 \end{bmatrix}, \\
\frac{\partial[{}^j\mathbf{K}_{S/l}]}{\partial k_{7/l}} &= \begin{bmatrix} 0 & 0 & 0 \\ 0 & 0 & 0 \\ 0 & 0 & 1 \end{bmatrix}.
\end{aligned} \tag{20}$$

TABLE 1: Configuration Settings for the Simulations and Modal Testing.

Modal testing configuration	Position of Leg Sliders (prismatic joints): distance from Base along Guideway			
	Leg 1	Leg 2	Leg 3	
				For simulation
				For modal testing
661				0 mm
662				15 mm
663				30 mm
664	75 mm	75 mm	every 5 mm	45 mm
665				60 mm
666				75 mm
667				90 mm
261				0 mm
262				15 mm
263				30 mm
264	15 mm	75 mm	every 5 mm	45 mm
265				60 mm
266				75 mm
267				90 mm

TABLE 2: Physical data for numerical calculations.

Length of leg	198	mm
Thickness of platform (modified)	18.5	mm
Triangle side length of platform (modified)	240	mm
Triangle side length of base bottom	270	mm
Length of guideway	90	mm
Slant angle of guideway from vertical	20	deg
Mass density of all parts	2710	kg/m ³
Young's modulus of all parts	70	GN/m ²
Poisson's ratio of all parts	0.33	

4. Modal Testing and Simulation

MATLAB codes were written based on the above analysis. The link model was built by using finite elements and was used to investigate the joint flexibility. For coordinate condensation, the selected master coordinates are the linear joint nodal coordinates in (4) in three branches (removing angular coordinate ${}^l\phi_R$ due to the difficulty to measure), plus three linear nodal coordinates at the centre of the platform, where the cutting tool is supposed to be attached, along pX , pY , and pZ directions. Thus there are 30 master coordinates in total. All other coordinates are set slave. Table 1 shows the physical parameters of the robot. Table 2 lists the two sets of robot configurations that were used in the modal testing and simulation. They feature both asymmetric and symmetric robot configurations.

Modal testing was conducted at each selected robot configuration. In order to understand the entire robot prototype, all measurement points were chosen to be evenly distributed on the platform and three legs. The excitation points were

chosen close to the spherical joints on the moving platform. Accelerometers were used to detect the responses in the local body reference directions at the measurement points of each leg and the platform. The excitation and response signals were amplified and then recorded using LabVIEW where the FRF of each measurement is generated. The sampling frequency was 2000 Hz and sampling time was 1 second. The window function was set as force-exponential with 50% force window and 10% exponential window. The FRF measurements were imported to the postprocessing software ME'scope which extracts the system natural frequencies and operating deflection shapes (ODSs) that are theoretically close to the mode shapes.

With eigen-sensitivity (13) and (14) at hand, the natural frequencies and mode shapes in the model can be modified at the selected robot configurations according to the modal testing results by adjusting the joint stiffness parameters as follows:

$$\{\Delta\mathbf{k}\} = \begin{bmatrix} \frac{\partial \mathbf{f}}{\partial \mathbf{k}} \\ \frac{\partial \Phi_1}{\partial \mathbf{k}} \\ \frac{\partial \Phi_2}{\partial \mathbf{k}} \\ \vdots \\ \frac{\partial \Phi_n}{\partial \mathbf{k}} \end{bmatrix}^+ \begin{Bmatrix} \Delta \mathbf{f} \\ \Delta \Phi_1 \\ \Delta \Phi_2 \\ \vdots \\ \Delta \Phi_n \end{Bmatrix}, \quad (21)$$

where $\{\Delta\mathbf{k}\}$ represents the modification values of the 21 joint stiffness parameters; $\{\Delta\mathbf{f}\}$ represents the errors of natural frequencies between the measurement and the calculation; $\{\Delta\Phi_i\}$, $i = 1$ to n , represents the errors of components in the i th mode shape between the measurement and the

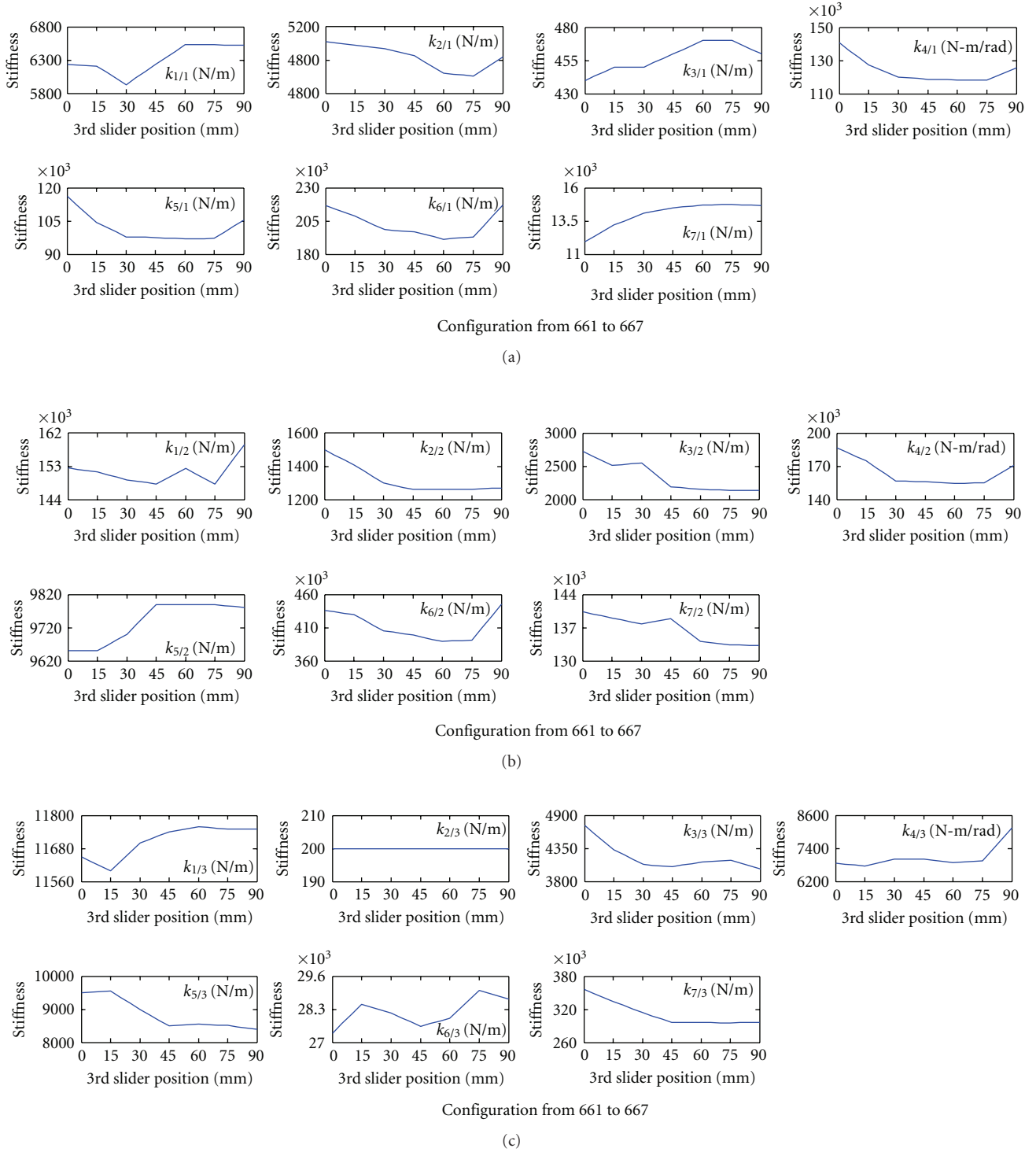
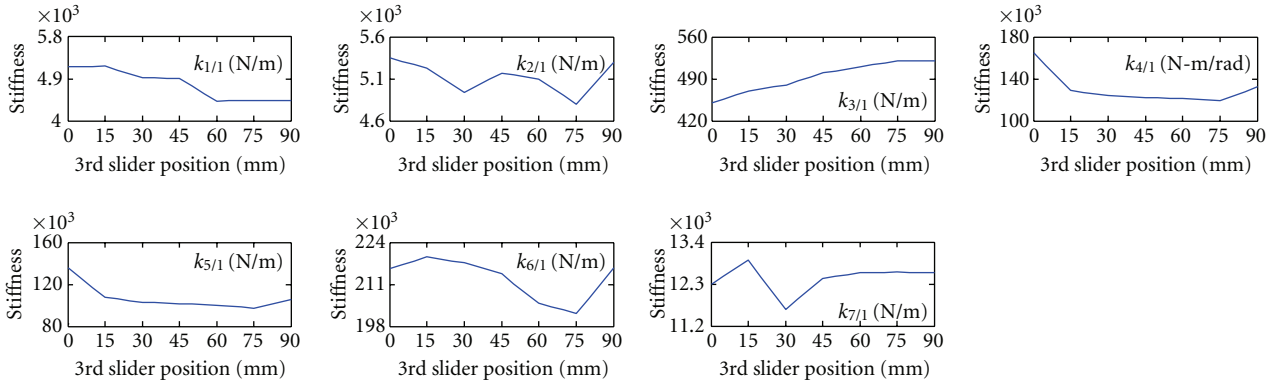


FIGURE 4: (a) Joint Stiffness in Branch 1 versus Configuration from 661 to 667. (b): Joint Stiffness in Branch 2 versus Configuration from 661 to 667. (c) Joint Stiffness in Branch 3 versus Configuration from 661 to 667.

calculation; $\partial \mathbf{f} / \partial \mathbf{k}$ is the matrix whose elements are the values from (13); $\partial \Phi_i / \partial \mathbf{k}$, $i = 1$ to n , is the matrix whose elements are the vector element values from (14); n is the eigen-solution order number; the superscript + stands for the Moore-Penrose pseudoinverse. Based on (21), an iteration

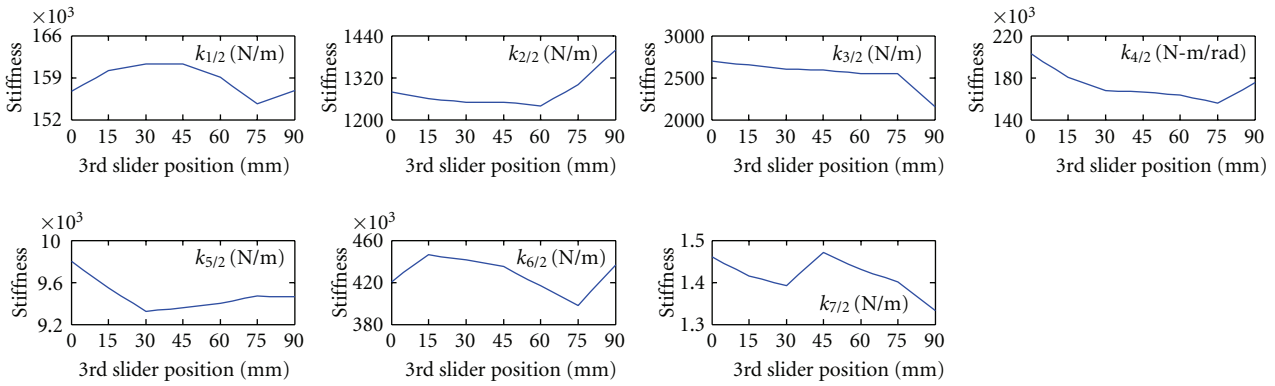
procedure is formed to update the joint stiffness parameters until the errors of natural frequencies and mode shapes are within specified limits.

Figures 4(a), 4(b), and 4(c) show the stiffness parameters of the joint virtual springs for the robot configurations



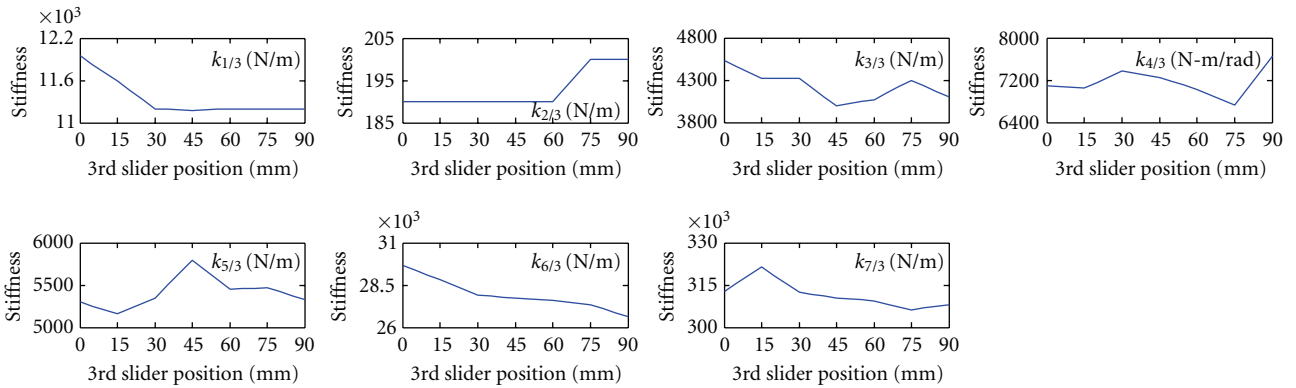
Configuration from 261 to 267

(a)



Configuration from 261 to 267

(b)



Configuration from 261 to 267

(c)

FIGURE 5: (a) Joint Stiffness in Branch 1 versus Configuration from 261 to 267. (b) Joint Stiffness in Branch 2 versus Configuration from 261 to 267. (c) Joint Stiffness in Branch 3 versus Configuration from 261 to 267.

from 661 to 667, and Figures 5(a), 5(b), and 5(c) from 261 to 267. The initial joint stiffness parameters are uniformly set as 10^5 N/m (or $N \cdot m/rad$ for $k_{4/l}$, $l = 1, 2, 3$) for all configurations. By using (21) for iteration, the joint stiffness

parameters are obtained at the modal testing configurations 661 to 667 and 261 to 267, and linearly interpolated into the simulation configurations between these modal testing configurations. These figures indicate that the joint stiffness

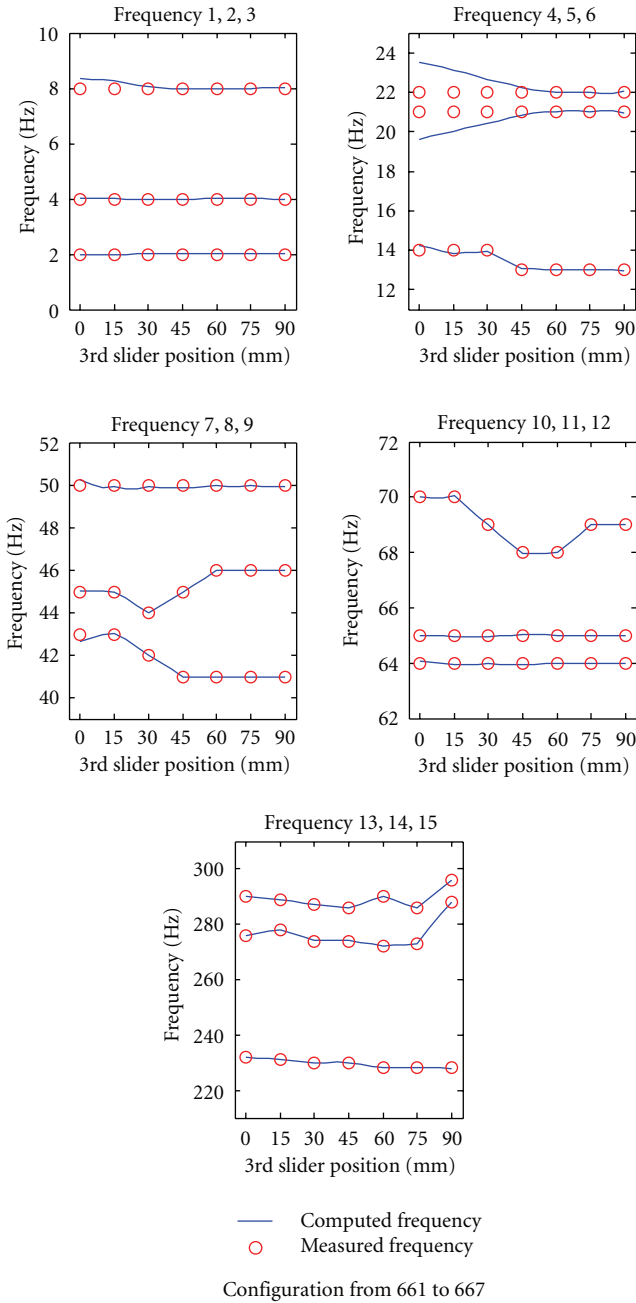


FIGURE 6: Natural Frequency versus Configuration from 661 to 667.

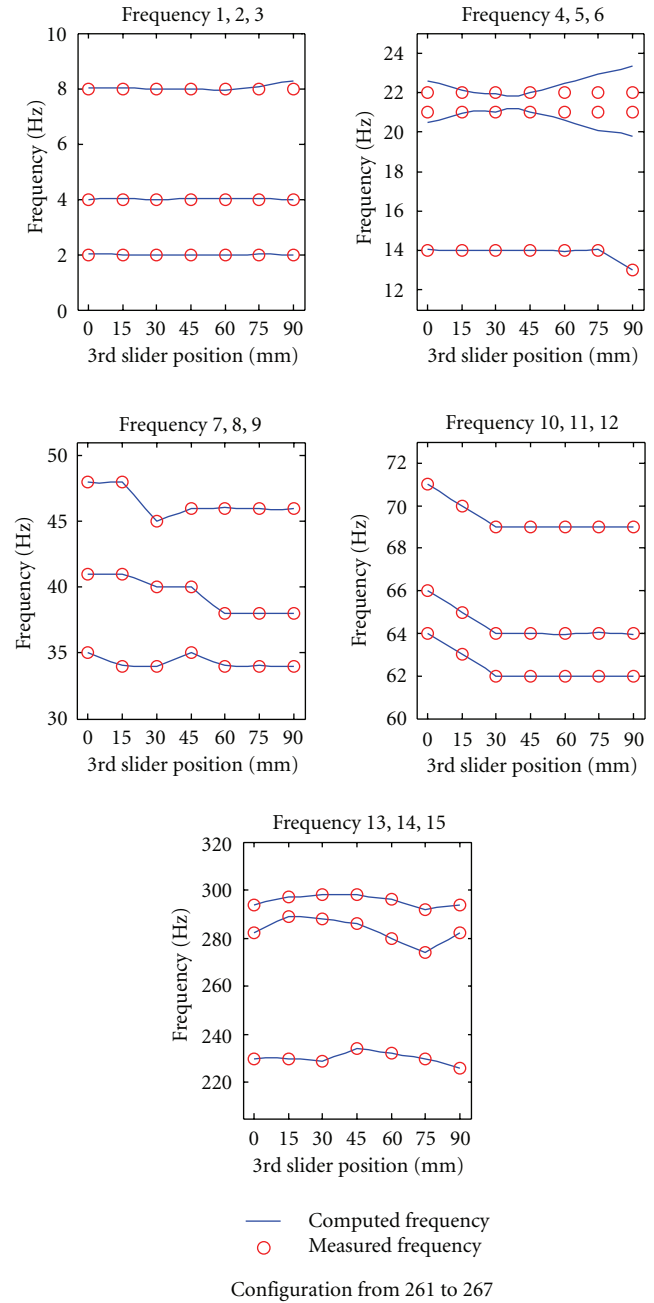


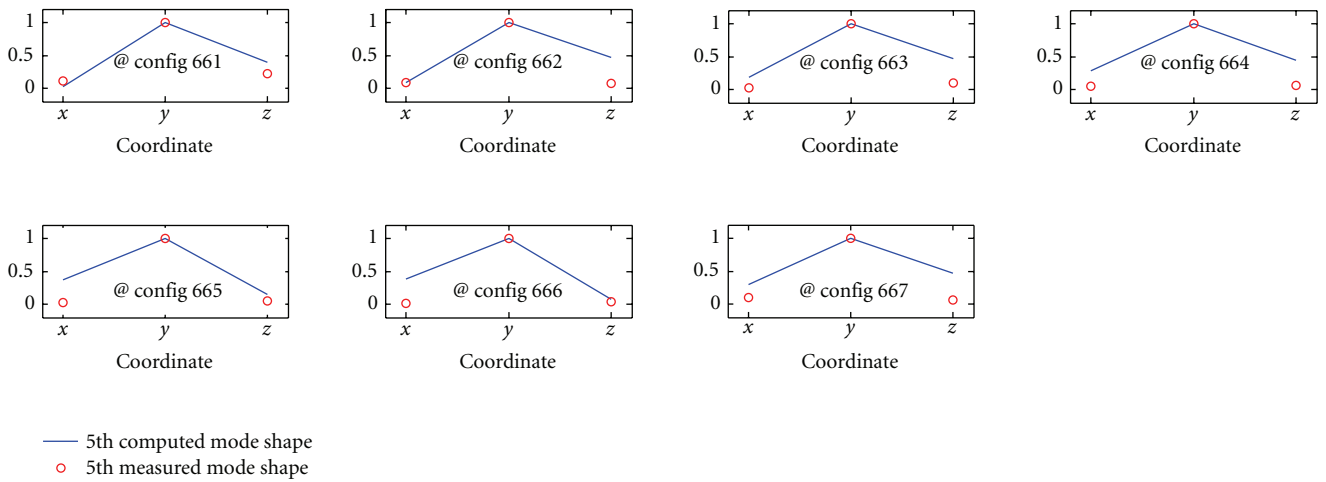
FIGURE 7: Natural Frequency versus Configuration from 261 to 267.

parameters are set configuration-dependent in order to match the variation of the system dynamic responses.

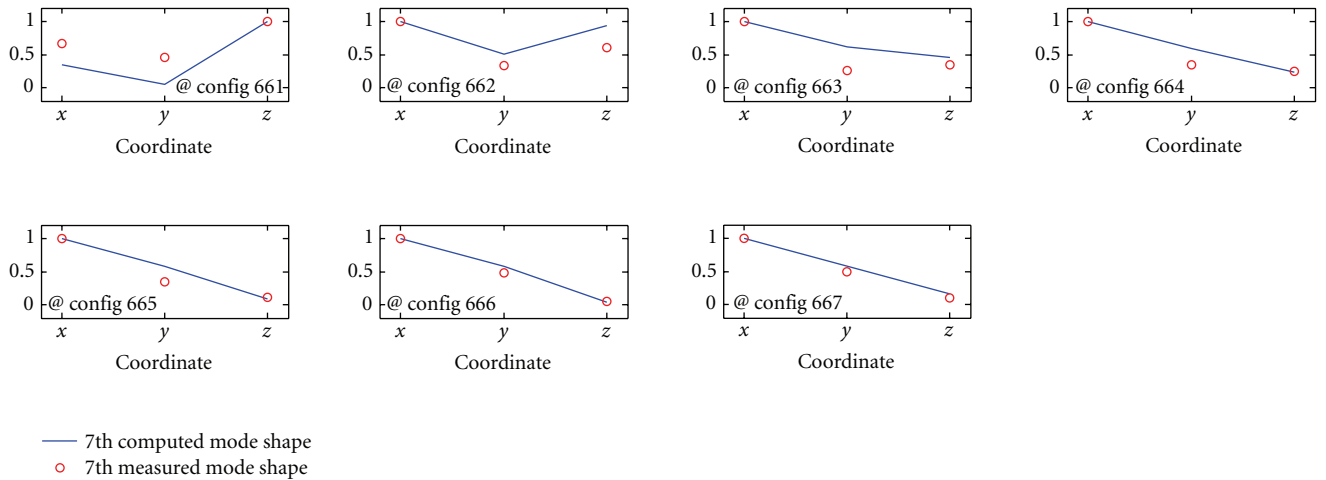
Figure 6 displays and compares the variations of the first 15 calculated and measured natural frequencies with the slider (prismatic joint) position changes starting at configuration 661 and ending at configuration 667 (referring to Table 1), and Figure 7 starting at configuration 261 and ending at configuration 267. The differences between the calculated and the measured frequencies are mostly less than 1%, and the largest deviations are less than 7% at the 5th and 6th natural frequencies at configurations 661 and 267. The possible reasons for the deviations are that the solutions

of the joint stiffness parameters are locally optimal and that these two frequencies may be related with some slave coordinates.

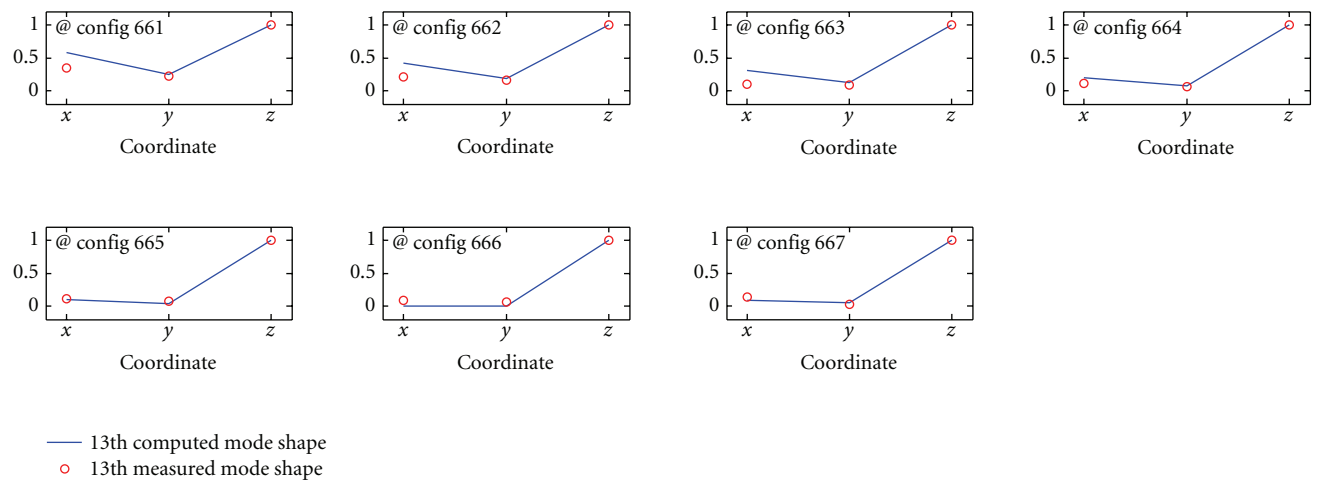
Figures 8(a), 8(b), and 8(c), respectively, display and compare the 5th, 7th, and 13th mode shapes at the node of the platform center (omitting mode shapes at other nodes) at configuration 661 to 667, and Figures 9(a), 9(b), and 9(c) at configuration 261 to 267. These mode shapes have the largest displacements at the platform center compared to other mode shapes: the 5th mode shape has the largest displacement in $^P Y$ direction, the 7th in $^P X$ direction, and the 13th in $^P Z$ direction. For easy comparison, the selected



(a)

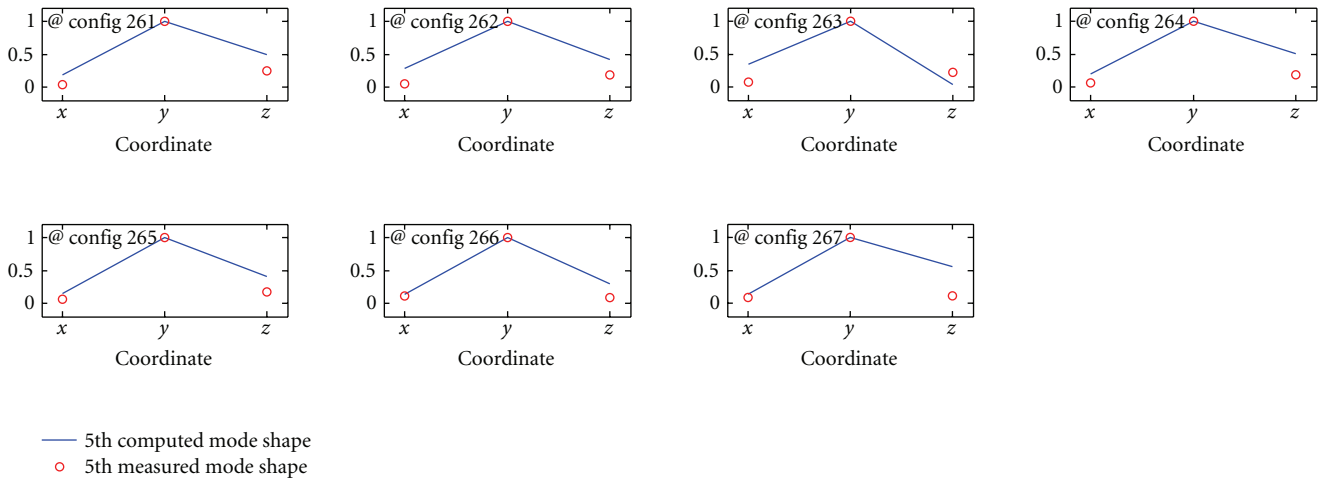


(b)

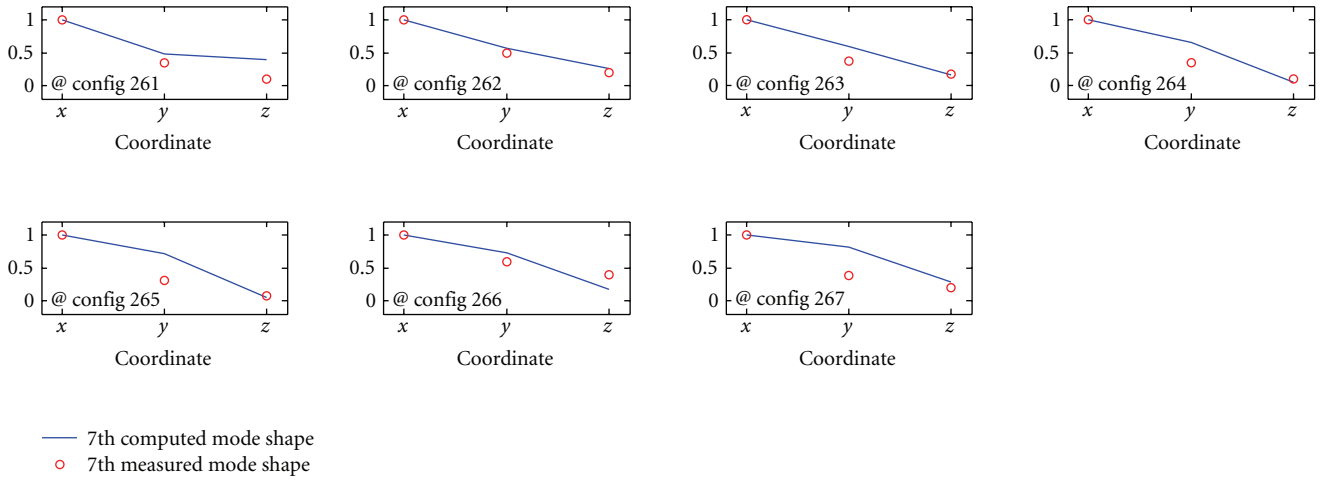


(c)

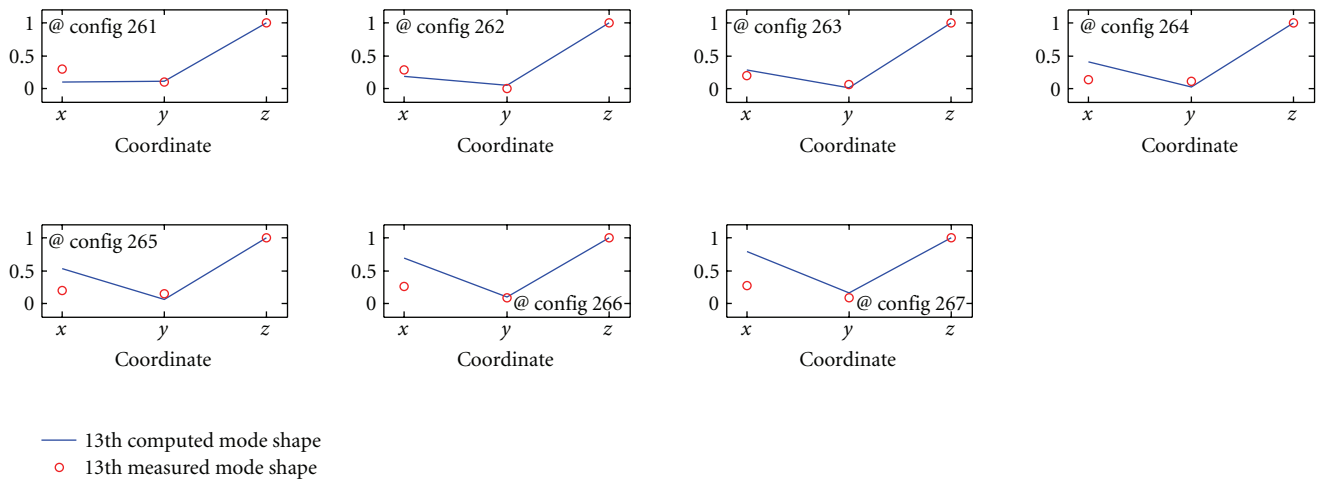
FIGURE 8: (a) 5th Mode Shape at Platform Center at Configuration 661 to 667. (b) 7th Mode Shape at Platform Center at Configuration 661 to 667. (c) 13th Mode Shape at Platform Center at Configuration 661 to 667.



(a)



(b)



(c)

FIGURE 9: (a) 5th Mode Shape at Platform Center at Configuration 261 to 267. (b) 7th Mode Shape at Platform Center at Configuration 261 to 267. (c) 13th Mode Shape at Platform Center at Configuration 261 to 267.

mode shape components are normalized. These figures show that the calculated mode shapes are close to the measured ones although they do not perfectly agree. The disagreement may result from the undamped joint model on which the joint stiffness parameters are calculated. For the simplicity of the method, however, it is worthy of the small loss of mode shape accuracy.

It must be indicated that, for the ideal rigid (tight) joint model of the same robot, natural frequencies and mode shapes will also be variable with the configuration changing (not shown here), but the natural frequencies are much higher than those of the flexible joint model. In simulation of the ideal joint model, the first natural frequency is about 200 Hz and the second is about 500 Hz. Therefore, Figures 6–9 display the flexible joint effect on the system due to configuration changes.

5. Conclusions

This study presents a configuration-dependant flexible joint model for a parallel robot. The method is based on adaptation of virtual springs between the joint components to simulate the joint flexibility. The joint stiffness matrix of virtual springs was derived. The system was condensed at the joint nodal coordinates. Eigen-sensitivity analysis was conducted on the condensed system matrix with respect to the stiffness parameters of the joint virtual springs. Dynamic modification was conducted at a series of robot configurations for the virtual spring parameters to be set variable to match the variation of the system natural frequencies and mode shapes obtained from modal testing. The virtual spring parameters between the selected robot configurations were obtained by interpolation. The research indicates that the presented method is effective and relatively easy to conduct, compared to other methods. The variable flexible joint model is applicable to flexible multibody systems with variable configurations.

References

- [1] H. S. Tzou, Y. Rong, and A. Nassirharand, "Design and stochastic simulation of elastically jointed mechanical systems," *Computer-Aided Design*, vol. 21, no. 7, pp. 435–440, 1989.
- [2] M. Bowden and J. Dugundji, "Joint damping and nonlinearity in dynamics of space structures," *American Institute of Aeronautics and Astronautics*, vol. 28, no. 4, pp. 740–749, 1990.
- [3] F. C. Moon and G. X. Li, "Experimental study of chaotic vibrations in a pin-jointed space truss structure," *American Institute of Aeronautics and Astronautics*, vol. 28, no. 5, pp. 915–921, 1990.
- [4] H. S. Tzou and Y. Rong, "Contact dynamics of a spherical joint and a jointed truss-cell system," *American Institute of Aeronautics and Astronautics*, vol. 29, no. 1, pp. 81–88, 1991.
- [5] T. Kakizaki, J. F. Deck, and S. Dubowsky, "Modeling the spatial dynamics of robotic manipulators with flexible links and joint clearances," *Journal of Mechanical Design, Transactions of the ASME*, vol. 115, no. 4, pp. 839–847, 1993.
- [6] L. D. Seneviratne, S. W. E. Earles, and D. N. Fenner, "Analysis of a four-bar mechanism with a radially compliant clearance joint," *Journal of Mechanical Engineering Science*, vol. 210, no. 3, pp. 215–223, 1996.
- [7] P. Ravn, S. Shivaswamy, B. J. Alshaer, and H. M. Lankarani, "Joint clearances with lubricated long bearings in multibody mechanical systems," *Journal of Mechanical Design, Transactions of the ASME*, vol. 122, no. 4, pp. 484–488, 2000.
- [8] A. L. Schwab, J. P. Meijaard, and P. Meijers, "A comparison of revolute joint clearance models in the dynamic analysis of rigid and elastic mechanical systems," *Mechanism and Machine Theory*, vol. 37, no. 9, pp. 895–913, 2002.
- [9] K.-L. Ting, J. Zhu, and D. Watkins, "Effects of joint clearance on position and orientation deviation of linkages and manipulators," *Mechanism and Machine Theory*, vol. 35, no. 3, pp. 391–401, 2000.
- [10] J. Zhu and K.-L. Ting, "Uncertainty analysis of planar and spatial robots with joint clearances," *Mechanism and Machine Theory*, vol. 35, no. 9, pp. 1239–1256, 2000.
- [11] J. Wang, C. M. Gosselin, and L. Cheng, "Modeling and simulation of robotic systems with closed kinematic chains using the virtual spring approach," *Multibody System Dynamics*, vol. 7, no. 2, pp. 145–170, 2002.
- [12] R. J. Guyan, "Reduction of stiffness and mass matrices," *American Institute of Aeronautics and Astronautics*, vol. 3, no. 2, p. 380, 1965.
- [13] R. L. Fox and M. P. Kapoor, "Rates of change of eigenvalues and eigenvectors," *American Institute of Aeronautics and Astronautics*, vol. 6, no. 12, pp. 2426–2429, 1968.

Research Article

Kinetostatic and Inertial Conditioning of the McGill Schönflies-Motion Generator

Alessandro Cammarata,¹ Jorge Angeles,² and Rosario Sinatra¹

¹ Dipartimento Ingegneria Industriale e Meccanica, Università di Catania, Viale A. Doria 5, 95123 Catania, Italy

² Department of Mechanical Engineering & Centre for Intelligent Machines, McGill University, 817 Sherbrooke Street W., Montreal, QC, Canada H3A 2K6

Correspondence should be addressed to Rosario Sinatra, rsinatra@diim.unict.it

Received 1 April 2009; Revised 31 August 2009; Accepted 30 October 2009

Academic Editor: Tian Huang

Copyright © 2010 Alessandro Cammarata et al. This is an open access article distributed under the Creative Commons Attribution License, which permits unrestricted use, distribution, and reproduction in any medium, provided the original work is properly cited.

This paper focuses on the optimization of the McGill Schönflies Motion Generator. Recent trends on optimum design of parallel robots led us to investigate the advantages and disadvantages derived from an optimization based on performance indices. Particularly, we optimize here two different indices: the kinematic conditioning and the inertial conditioning, pertaining to the condition number of the Jacobian matrix and to that of the generalized inertia matrix of the robot, respectively. The problem of finding the characteristic length for the robot is first investigated by means of a constrained optimization problem; then plots of the kinetostatic and the inertial conditioning indices are provided for a particular trajectory to be tracked by the moving platform of the SMG. Deep connections appear between the two indices, reflecting a correlation between kinematics and dynamics.

1. Introduction

In recent years researchers and industry have been paying more attention to parallel-kinematics machines (PKMs) with reduced mobility [1–4]. The growing search for high performance in terms of accuracy, precision, maximum acceleration, and ease in control revealed some limits of PKMs with full mobility to accomplish certain types of tasks [5]. The main characteristic of a PKM with reduced mobility is a reduced number of limbs with respect to a six-degrees-of-freedom (dof) PKM. This aspect yields a reduced weight of the global structure, which leads to an enhanced performance of the moving platform (MP). Besides, this feature implies a lower complexity of the architecture, which leads to a lower risk of limb collisions, while increasing the workspace. Obviously, robots of this type are designed for specific applications and cannot perform the general tasks of their six-dof counterparts. Then again, industrial tasks usually call for specific types of motions; that is, not all dof of the MP are necessary. Some applications, as pick-and-place, drilling, riveting, assembling, painting, and so on, call for three to five dof. If a particular task required more dof

than those provided by a single PKM, two or more PKMs might be assembled to cooperate. Unfortunately, the simpler architecture of these robot does not translate into a simpler analysis. The main issues lie in type synthesis, which excludes the use of the intuition at the conceptual design stage; a more systematic synthesis procedure of this new class of robots is needed [6].

Achieving high performance involves optimization in terms of kinematics and dynamics. Essentially, a performance index is a scalar function related to the kinematic or the dynamic performance of a robot. Kinematic-performance indices are mainly based on the robot Jacobian matrix. Various performance indices based on the Jacobian matrix have been proposed: we cite the *conditioning* of robotic manipulators [7–9], or the concept of *manipulability*, as proposed by Yoshikawa [10], is an attempt to measure the distance to singularity of the Jacobian matrix of a robot. One of the most frequently used performance indices, the *kinetostatic conditioning index*, is based on the *condition number* of the Jacobian matrix [11]. We refer to [12–14] for a summary of the aforementioned kinematic-performance indices.

We shall devote our paper to only the kinetostatic conditioning index, the one studied most intensively.

Most of the dynamic performance indices have been derived through analogy from the kinetostatic indices. As a matter of fact, the *dynamic conditioning index* is obtained similar to the kinetostatic conditioning index by replacing the Jacobian matrix with the *generalized inertia matrix* (GIM). By the same token, Yoshikawa introduced the *dynamic manipulability measure* as the counterpart to his kinematic manipulability [15]. Wiens et al. [16] proposed some indices for the measure of the nonlinear inertia forces while Khatib and Burdick [17] defined the *isotropic acceleration* as the greatest magnitude that the acceleration of the end-effector can reach in any direction starting from a given manipulator configuration. Ma and Angeles introduced the dynamic isotropy of an n -dof serial manipulator and the “dynamic conditioning index” as a measure of the latter [18]. Di Gregorio and Parenti-Castelli proposed the use of three homogeneous coordinates, chosen among the operational-space coordinates, for the definition of a three-dof-manipulator GIM to be used in the determination of the dynamically isotropic configurations meaningful for three-dof-manipulator design [19]. Di Gregorio studied two-dof mechanisms and defined some indices that characterize the dynamic isotropy of these mechanisms [20].

In this paper the case of the McGill Schönflies-Motion Generator (SMG) is analyzed to apply the concepts of kinetostatic and inertial conditioning.

First, a brief description of the robot is provided. Then, the concept of characteristic length for positioning and orienting robots is recalled and adapted to the case of the McGill SMG. Further, a constrained optimization problem is set to find the posture of the robot with a Jacobian matrix and a GIM of minimum condition number. Finally, the same indices are analyzed while the robot moves along a standard trajectory, the *test-cycle trajectory*, to show that it would be possible to find an optimum location for the said trajectory where the indices attain minimum values.

2. Robot Description

Here a brief description of the McGill SMG is given, further details being available in [21]. The McGill SMG is a parallel robot for SCARA-type motions: its moving platform can undergo three independent translations and one rotation about a vertical axis. A CAD model is shown in Figure 1, where one can distinguish the different parts composing the robot. Starting from the top of the fixed frame, each limb is composed of two motors, an epicyclic gear train (EGT), a right-angled gear box (RGB), and an RIIIR kinematic chain. Then, the two chains, one for each limb, are coupled to a moving platform (MP). The EGTs and the RGBs are made of steel, while the two brackets, referred to as the distal and the proximal brackets, links of the RIIIR chain, are fabricated of aluminum. Finally, the Π joints are slender plate elements fabricated of carbon-fiber to make these joints lighter.

Figure 2 shows the kinematic chain of the SMG. Hereafter, we will refer to the set of angles $\{\theta_{I1}, \theta_{I2}, \theta_{II1}, \theta_{II2}\}$

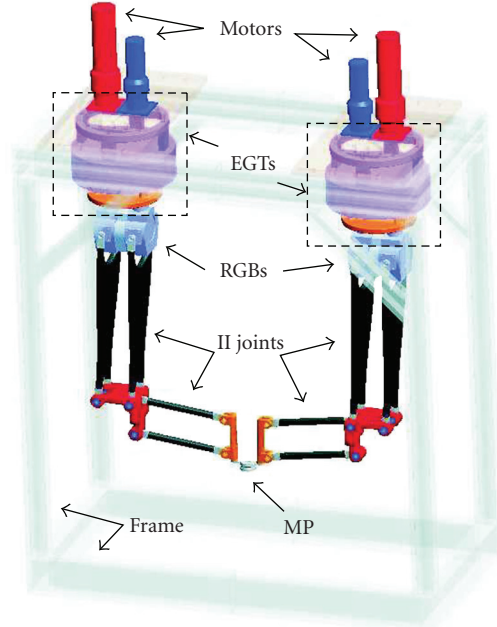


FIGURE 1: CAD model of McGill Schönflies Motion Generator.

TABLE 1: Nomenclature.

Notation	Description
(x, y, z)	The Cartesian coordinates of the operation point P of the end-effector, expressed in the coordinate frame $\mathcal{F}(O, X, Y, Z)$
ϕ	Angle of rotation of the end-effector about the vertical axis
θ_{ji}	Angle of rotation, measured according with the right-hand rule
R	$\ \vec{O}_{J4}P\ $
\mathbf{f}_j	Unit vector normal to the J -limb
l_i	$\ \vec{O}_{J(i-1)}\vec{O}_{Ji}\ $, for $i = 1, 2, 3, 4$
l_0	Distance between the two fixed bases, that is, between the two pan-axes of the drive-units

as the actuated-joint variables, while the remaining angles, $\{\theta_{I3}, \theta_{I4}, \theta_{II3}, \theta_{II4}\}$, are the passive-joint variables. The DKP gives four different solutions for the actuated-joint variables when the generic configuration of the robot is defined. It is noteworthy that, during the optimization problem, we will refer only to a single manifold of solutions by imposing suitable initial values for the said angles. Furthermore, the plane of the Π joint of limb J is normal to the unit vector \mathbf{f}_j , $J = I, II$.

In Table 1 the notation used throughout the paper is described. All symbols with double subscript, comprising one Roman and one Arabic numeral, refer to the limb number, I or II , and to the corresponding item of the respective arm. In Table 1, $J = I, II$ and $i = 1, 2, 3$.

We will not dwell on the derivation of the kinematics and dynamics model of the SMG, described in detail in [21].

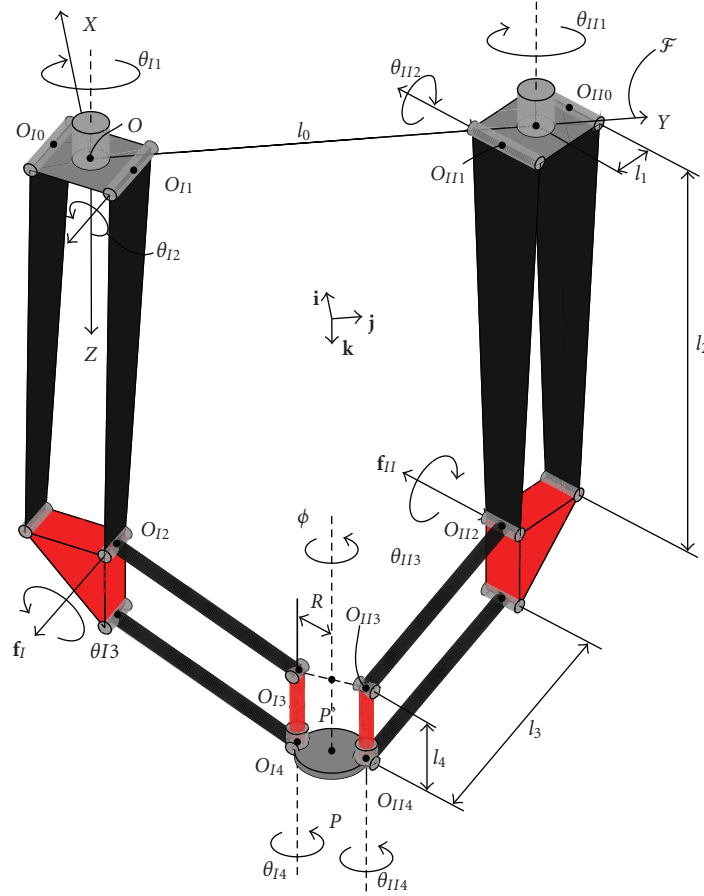


FIGURE 2: Kinematic chain of McGill Schönflies Motion Generator.

3. The Characteristic Length

Before starting with the conditioning-index definition, we recall the kinematics equation of a parallel robot:

$$\mathbf{A}\mathbf{t} = \mathbf{B}\dot{\boldsymbol{\theta}}, \quad (1)$$

which relates the array of actuated joint rates $\dot{\boldsymbol{\theta}}$ with the twist array \mathbf{t} of the MP at the operation point, located on the moving platform, by means of two matrices, \mathbf{A} and \mathbf{B} , referred to as the direct-kinematics and the inverse-kinematics Jacobian matrices, respectively. For the case at hand, in light of the reduced mobility of the MP of the SMG, we have

$$\mathbf{t} \in \mathbb{R}^4, \quad \mathbf{A} \in \mathbb{R}^{6 \times 4}, \quad \mathbf{B} \in \mathbb{R}^{6 \times 4}, \quad \dot{\boldsymbol{\theta}} \in \mathbb{R}^4 \quad (2)$$

as derived in [21]. It is noteworthy that \mathbf{A} and \mathbf{B} are 6×4 Jacobians, (2) thus entailing six equations linear in the four independent components of either \mathbf{t} or $\dot{\boldsymbol{\theta}}$. We resorted to this *redundancy* to add robustness to the kinematics model, so as to prevent algorithmic singularities—not related to the actual kinematics of the robot—which occur whenever the planes of the two limbs coincide. Here, solving (1) for

the twist array \mathbf{t} , let us introduce the definition of the SMG Jacobian \mathbf{J} as

$$\mathbf{t} = \mathbf{J}\dot{\boldsymbol{\theta}}, \quad \mathbf{J} = \mathbf{A}^\dagger \mathbf{B}, \quad (3)$$

where \mathbf{A}^\dagger is the left Moore-Penrose generalized inverse of \mathbf{A} [22].

For robots accomplishing positioning and orienting tasks, like every SCARA, and the SMG is a parallel version thereof, the Jacobian bears different units, thus preventing the computation of the Jacobian condition number for optimization tasks. In order to remove the dimensional inhomogeneity, a *characteristic length* is introduced. The characteristic length is defined as that normalizing length that renders the condition number of the Jacobian matrix a minimum [12]. As we will explain in detail in this section the condition number of the Jacobian matrix is bounded from below by unity but unbounded from above. Two situations can occur: robots whose Jacobian condition number can attain the minimum value of unity at one or more postures, termed *isotropic* robots, and robots whose Jacobian condition number attains a minimum larger than unity, at certain postures. Isotropy is not the rule but depends on the robot architecture.

It has been demonstrated that for spatial serial manipulators the characteristic length is the root mean square of

the distances of the revolute axes to the operation point when the robot finds itself at a posture of minimum condition number [23]. For parallel robots this geometric condition has not been found, although the original definition still stands. Finding a formula for the characteristic length is possible only for simple cases; more generally, the characteristic length is calculated via an optimization procedure.

The problem we solve here is formulated as follows: given a manipulator with a prescribed architecture, find its characteristic length as that which renders the Jacobian dimensionless and its condition number a minimum at an optimum posture. As the characteristic length is strictly connected to the concept of condition number of a matrix, that is, the Jacobian matrix, we briefly recall some pertinent concepts. It is noteworthy that the concept of condition number of a matrix is meaningful if and only if all the matrix entries bear the same physical units. The simplest definition of condition number is based on the matrix 2-norm, namely, [22],

$$\kappa_2(\mathbf{M}) = \frac{\sigma_{\max}}{\sigma_{\min}}, \quad (4)$$

where σ_{\max} and σ_{\min} are the maximum and the minimum singular values of the matrix \mathbf{M} . Apparently, we can order all the singular values of a matrix if and only if all its entries bear the same units. This definition, based on the 2-norm, is simple to state, but rather cumbersome to work with because $\kappa_2(\mathbf{M})$ is not an *analytic function* of the matrix entries everywhere, which brings about some computational difficulties. For this reason we use the condition number based on the *Frobenius norm* [22], namely,

$$\kappa_F(\mathbf{M}) = \|\mathbf{M}\|_F \|\mathbf{M}^{-1}\|_F, \quad (5)$$

where, for SMGs, $\|\mathbf{M}\|_F$ takes the form

$$\|\mathbf{M}\|_F \equiv \sqrt{\frac{1}{4} \text{tr}(\mathbf{M}^T \mathbf{M})} \equiv \sqrt{\frac{1}{4} \text{tr}(\mathbf{M} \mathbf{M}^T)} \quad (6)$$

which is the *weighted Frobenius norm* of a 4×4 matrix, as the Jacobian at hand has four nonzero singular values. Using (6), $\kappa_F(\mathbf{M})$ becomes

$$\kappa_F(\mathbf{M}) = \frac{1}{4} \sqrt{\text{tr}(\mathbf{M}^T \mathbf{M}) \text{tr}[(\mathbf{M}^T \mathbf{M})^{-1}]}. \quad (7)$$

We recall further that $\kappa_F(\mathbf{M})$, like any form of condition number, is bounded from below but unbounded from above, that is,

$$1 \leq \kappa_F(\mathbf{M}) < \infty. \quad (8)$$

Once again, a robot is termed *isotropic* when the condition number of its Jacobian reaches its minimum value of unity. It should be underlined that the condition number is configuration-dependent, and so, a manipulator can attain isotropic configurations only at certain points of its workspace if its design so permits.

For the McGill SMG we will set a constrained optimization problem to find its characteristic length L and its

minimum condition number. Firstly, let \mathbf{x} be the design-variable vector whose components are the joint angles and the characteristic length L . We start by noticing that the angles θ_{J4} , $J = I, II$, have no effect on the Jacobian \mathbf{J} of (3); hence, only the remaining six angles will be taken into account. It should be mentioned that it is possible to chose a minimum set made of only actuated angles and the characteristic length L , but this choice, while reducing the number of design variables, makes the calculation more cumbersome, and so, we will not attempt it. The design-variable vector is then defined as

$$\mathbf{x} \equiv [\theta_{I1} \ \theta_{I2} \ \theta_{I3} \ \theta_{II1} \ \theta_{II2} \ \theta_{II3} \ L]^T. \quad (9)$$

Now, after introducing the vectors $\mathbf{p}_J = \overrightarrow{OO_{J3}}$, $J = I, II$, the optimum value of \mathbf{x} is found by solving the constrained optimization problem:

$$\min_{\mathbf{x}} \kappa_F^2(\mathbf{J}) \quad (10)$$

subject to the constraints:

$$\|\overrightarrow{O_{I4}O_{II4}}\|^2 \equiv \|\overrightarrow{O_{I3}O_{II3}}\|^2 \equiv \|\mathbf{p}_I - \mathbf{p}_{II}\|^2 = 4R^2, \quad (11a)$$

$$z_I = z_{II}, \quad (11b)$$

where z_J is the z -component of \mathbf{p}_J , $J = I, II$ and R is the radius of the MP. Notice that (11a)-(11b) implicitly take into account the dependency of the passive-joint angles from their actuated counterparts. The first constraint in (11a) must be set to preserve the parallel architecture, while the second in (11b) guarantees that the moving platform undergoes Schönflies displacements only.

It is noteworthy that the minimization problem is set for all configurations inside the workspace of the robot. As the moving platform has four dof, that is, three translations and one rotation, we might give a complete representation of the workspace only in a four-dimensional space. To overcome this issue we will recur to the constant orientation workspace representation, that is, the reachable volume attained by the operation point of the MP, its centroid in our case. In Figure 3 the said workspace is plotted for different values of the angle of rotation of the MP.

The results of the minimization problem are reported in Table 2 and Figure 4. As we can see, two postures, symmetric with respect to the YZ -plane, in which the robot Jacobian matrix attains minimum condition number $\kappa_F(\mathbf{J})$, exist. The values of \mathbf{x} and $\kappa_F(\mathbf{J})$ are reported in Table 2.

Apparently, the condition number $\kappa_F(\mathbf{J})$ is very close to unity but is not unity; hence, the McGill SMG is not an isotropic robot.

4. Inertial Conditioning

Germane to the kinematic conditioning, the concept of dynamic isotropy relates to the GIM \mathbf{I} of a robotic mechanical system. It has been recognized that it is convenient to have an isotropic GIM, that is, of the form

$$\mathbf{I} = \sigma \mathbf{1}, \quad (12)$$

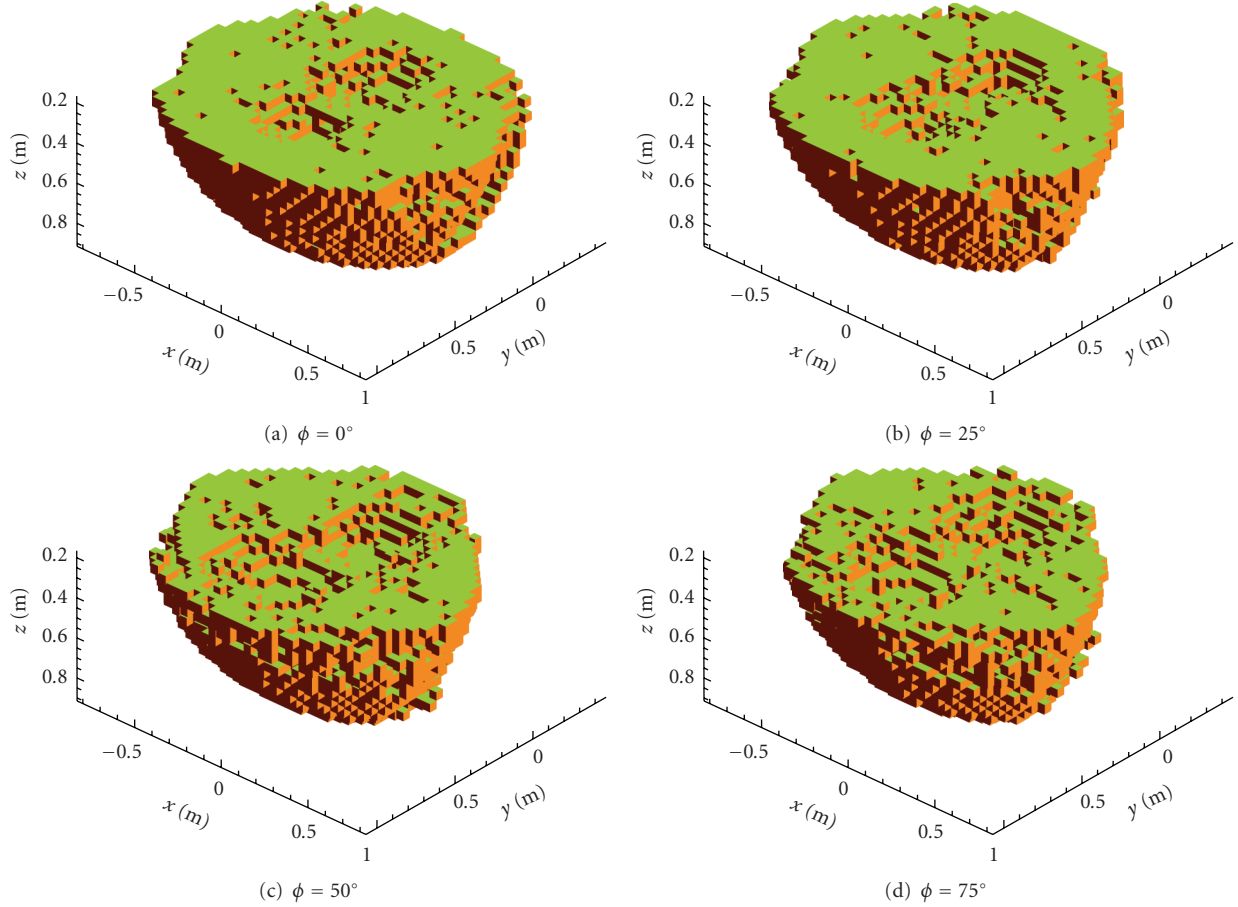


FIGURE 3: Constant orientation workspace of the McGill SMG.

TABLE 2: Postures with optimum condition number and characteristic length.

Solution	θ_{I1}	θ_{I2}	θ_{I3}	θ_{II1}	θ_{II2}	θ_{II3}	L (m)	$\kappa_F(\mathbf{J})$
Figure 4(a)	0.6433	1.4369	0.9763	-0.6434	1.7047	2.1653	0.0514	1.1132
Figure 4(b)	-0.6434	1.4370	0.9763	0.6433	1.7047	2.1652	0.0514	1.1132

where \mathbf{I} is the $n \times n$ identity matrix and σ a real, positive number, the unique eigenvalue of \mathbf{I} , of algebraic multiplicity n . An isotropic GIM is convenient because this matrix must be inverted when solving for joint accelerations in the direct-dynamics problem. The inertia matrix being positive-definite, its eigenvalues are identical to its singular values.

Usually, the units of the GIM depend on the generalized coordinates chosen to describe a mechanical system. In robotics, for control purposes, it is often convenient to make these coincident with the actuated-joint variables. Therefore, the entries of the GIM of a robot can bear disparate units. The McGill SMG is actuated by two pairs of motors, all entries of \mathbf{I} thus bearing units of kg m^2 , and hence, the GIM is dimensionally homogeneous. We have chosen to consider in our analysis also the EGTs and RGBs because most of the inertia of the SMG is concentrated on them.

The global GIM \mathbf{I} is derived upon adding the three inertia matrices, \mathbf{I}_E , \mathbf{I}_{RGB} , and \mathbf{I}_L , of the three subsystems making

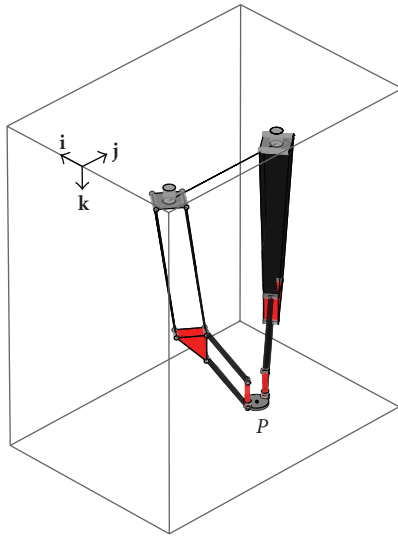
up the SMG: EGTs, RGBs, and aluminum parts. Hence, the global GIM becomes

$$\mathbf{I} = \mathbf{I}_E + \mathbf{I}_{\text{RGB}} + \mathbf{I}_L. \quad (13)$$

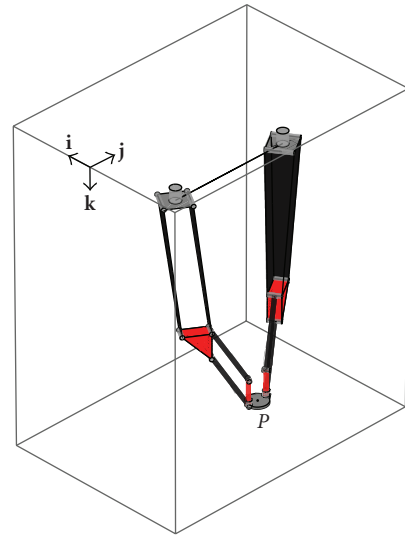
All parameters used to obtain these matrices are recorded in [21], the corresponding expressions derived in the same reference.

We formulate now an optimization problem to find the posture of the SMG at which its GIM attains its minimum condition number $\kappa_F(\mathbf{I})$. Now, $\kappa_F(\mathbf{I})$ is the objective function to minimize, as in (10), with respect to a new design-variable vector \mathbf{y} , defined as

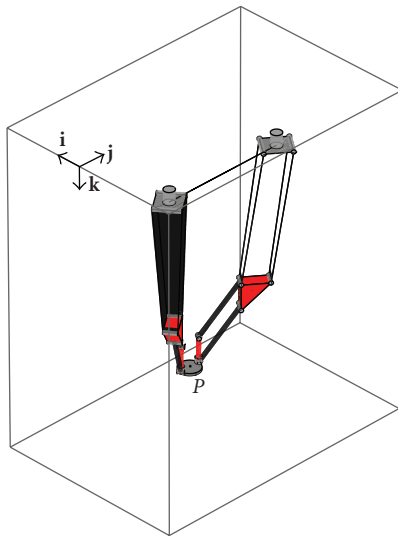
$$\mathbf{y} \equiv [\theta_{I1} \ \theta_{I2} \ \theta_{I3} \ \theta_{II1} \ \theta_{II2} \ \theta_{II3}]^T \quad (14)$$



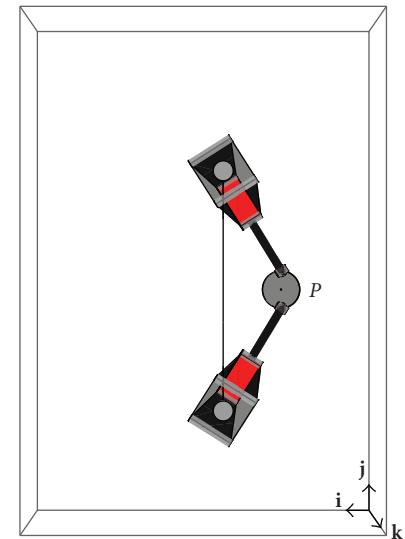
(a)



(a) 3D view



(b)



(b) Top view

FIGURE 4: Optimum symmetrical configurations for minimum condition number.

FIGURE 5: Configuration (a) of the minimum condition number $\kappa_F(\mathbf{I})$.

TABLE 3: Inertial conditioning at two minimum-condition-number postures symmetric with respect the vertical X - Z plane.

Solution	θ_{I1}	θ_{I2}	θ_{I3}	θ_{II1}	θ_{II2}	θ_{II3}	$\kappa_F(\mathbf{I})$
(a)	-0.5658	1.4433	1.0251	0.5659	1.6983	2.1165	1.0260
(b)	0.5658	1.4433	1.0251	-0.5659	1.6983	2.1165	1.0260

subject to the same constraints introduced in (11a)-(11b). It is noteworthy that the global GIM is a 4×4 matrix whose entries bear all units of kg m^2 . Figure 5 shows one of the two symmetrical minimum-condition-number postures, while Table 3 records the values of \mathbf{y} and $\kappa_F(\mathbf{I})$ for the said postures.

The GIM at the minimum-condition-number posture is close to isotropic, namely,

$$\mathbf{I} = \begin{bmatrix} 0.5814 & -0.0154 & -0.0676 & -0.0181 \\ -0.0154 & 0.5872 & -0.0181 & 0.0547 \\ -0.0676 & -0.0181 & 0.5814 & -0.0154 \\ -0.0181 & 0.0547 & -0.0154 & 0.5872 \end{bmatrix}. \quad (15)$$

Notice that matrix \mathbf{I} comes only two distinct blocks, which comes as no surprise, given the symmetries, geometric, and mechanical, of the robot.

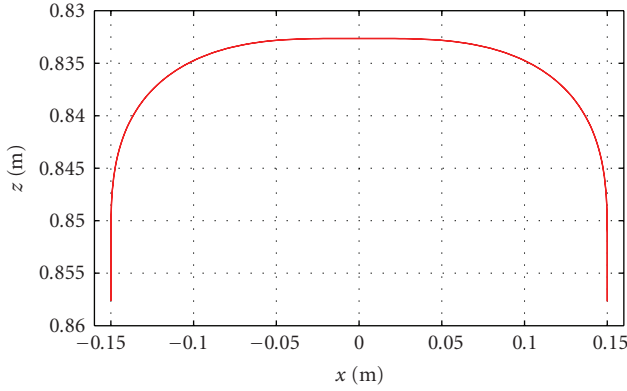


FIGURE 6: Path generated using a 4-5-6-7 polynomial displacement program, displayed with different x and z scales.

5. Test-Cycle Trajectory

In this section we apply the concepts of kinetostatic and inertial conditioning to optimize the pose—position and orientation—of a *test-cycle trajectory* in the X - Z plane. The test-cycle trajectory is a particular trajectory commonly adopted by the industry to represent the standard pick-and-place task performed by a SCARA robot. In our case, the test-cycle trajectory lies in the medium vertical plane of the robot. The SMG should pick an object, release it, and return to the initial MP pose in a given cycle of duration T . Shown in Figure 6 is the trajectory, projected into the X - Z plane, as generated using a 4-5-6-7 polynomial displacement program, which is reproduced here for quick reference [12]:

$$s(\tau) = -20\tau^7 + 70\tau^6 - 84\tau^5 + 35\tau^4, \quad (16)$$

where $s(\tau)$ is a nondimensional displacement function, with $\tau = t/T$ as a nondimensional time parameter, t is time, and T is the time elapsed between the ends of the trajectory. A characteristic of this polynomial is that it provides zero jerk at the start and the end of the motion, which means that the polynomial is C^3 -continuous [12]. The fourth dimension of the MP trajectory involves a rotation of 144° about a vertical axis, as the operation point P of Figure 2 moves horizontally, going back to the original MP orientation on the return part of this motion. In Figure 7 the X and Z coordinates of point P and the angle of rotation ϕ of the moving plate are separately shown over the whole trajectory.

5.1. Kinetostatic Conditioning along the Test-Cycle Trajectory.

The kinetostatic index is used here to compare different locations, on the vertical plane of symmetry of the robot, of the same test-cycle trajectory. Hence, the kinetostatic conditioning index has been evaluated on the test-cycle trajectory (in solid line) and on two other trajectories shifted along the Z -axis by 0.05 m and 0.10 m, but lying in the same XZ -plane, as shown in Figure 8. We can notice that the condition number worsens when the test-cycle trajectory is translated closer to the base.

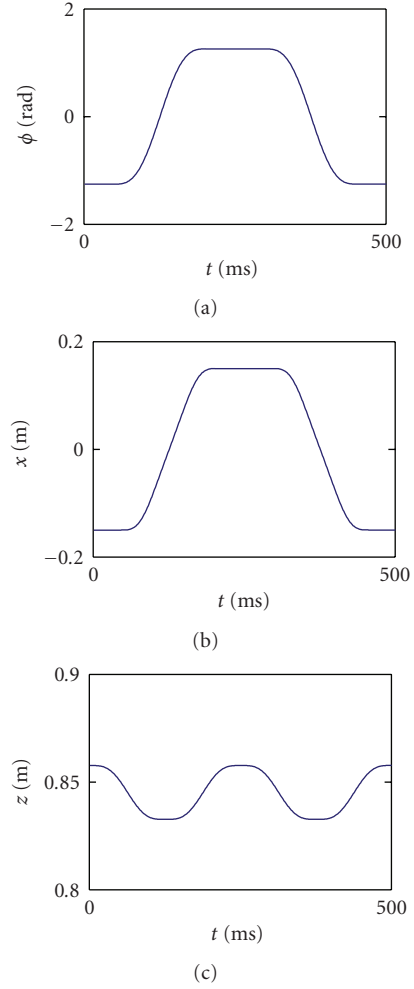


FIGURE 7: Cartesian variables along the test-cycle trajectory.

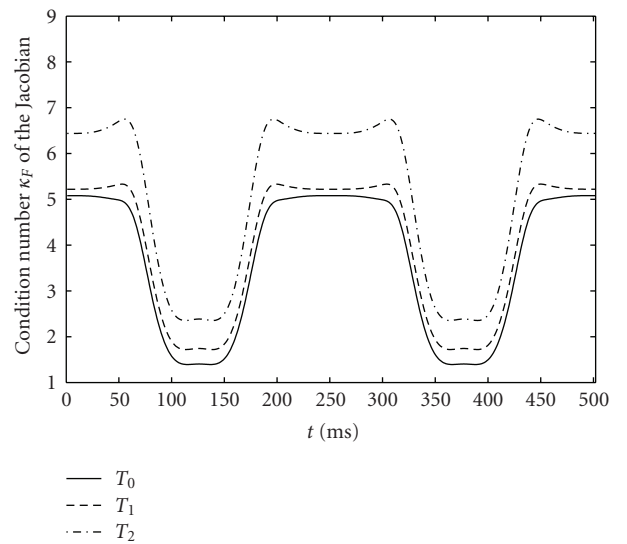


FIGURE 8: Condition number of the Jacobian J along the three trajectories lying in the X - Z plane: T_0 : the test trajectory; T_1 : shifted 0.05 m, along Z , from T_0 ; T_2 : shifted 0.10 m, along Z , from T_0 .

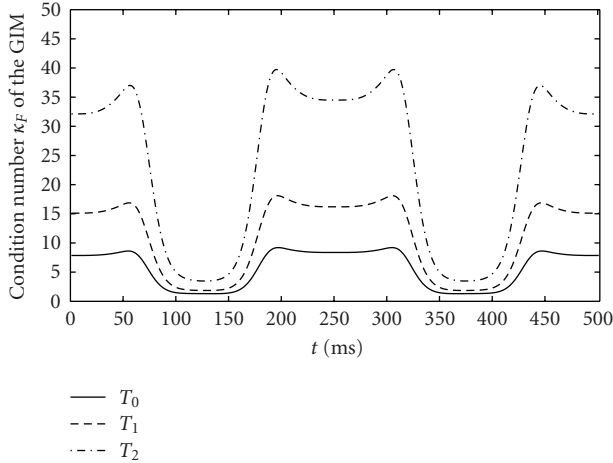


FIGURE 9: GIM condition number along three distinctly located trajectories lying in the X - Z plane: T_0 : the test-trajectory; T_1 : shifted 0.05 m, along Z , from T_0 ; T_2 : shifted 0.10 m, along Z , from T_0 .

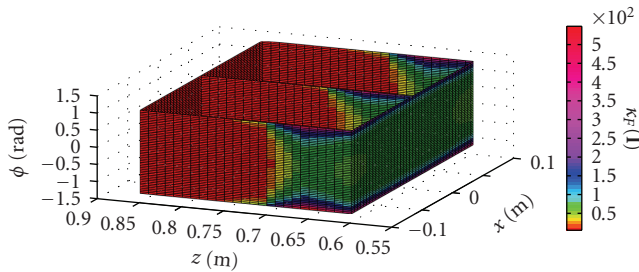


FIGURE 10: GIM condition-number distribution on a constant- y volume.

5.2. Inertial Conditioning along the Test-Cycle Trajectory. Figure 9 shows how $\kappa_F(\mathbf{I})$ varies on the test-trajectory plane, increasing when the operation point of the moving platform \mathcal{M} approaches the base. Comparing Figures 8 and 9 we realize that the inertial conditioning index follows the same trend of its kinetostatic counterpart, but the values seem to be amplified and distorted in their scale and maximum peaks.

Finally, in Figure 10 we plot the condition number of \mathbf{I} on the x - y - ϕ space. A volume of size (0.2 m, 0.25 m, 2.4 rad) has been considered, while the y coordinate has been held fixed to 0.3 m, the value at the XZ -plane of symmetry of the robot. Some slicing planes have been introduced to better visualize results. Following the said figure we can observe how $\kappa_F(\mathbf{I})$ worsens rapidly as the robot moves towards lower values of z . This means that it will be more convenient to move the test-cycle trajectory, onto the XZ -plane of symmetry of the robot, as far as possible from the base.

Summarizing results we can conclude that the kinetostatic and inertial conditioning indices seem to have similar trends, the latter being a stretched and scaled version of the former. Therefore, one might consider only one of the two optimization problems to observe the robot behaviour on a quality level. Sometimes, as in the case of the McGill SMG, it might be easier to work with the inertial conditioning index

rather than with its kinetostatic counterpart, for the latter does not require a characteristic length as a further design-variable. On the contrary, the kinetostatic index is usually simpler to calculate than the inertial index, for the latter needs the complete dynamics model.

6. Conclusions

The kinematic and dynamic conditioning of the McGill SMG were studied. Firstly, a constrained optimization problem was set to find the robot characteristic length and the minimum condition number of the robot Jacobian. Then, a similar constrained optimization problem was set to find the optimum robot posture of minimum condition number of the generalized inertia matrix. The kinetostatic and inertial conditioning indices were evaluated on a particular trajectory, the test-cycle, to be tracked by the MP. The evaluation has revealed similar behaviors between kinetostatic and dynamic indices. Particularly, the inertial effects seem to amplify and distort the values of the kinetostatic index, thereby modifying both the scale and the maximum peaks. Finally, the inertial conditioning index was plotted over a constant- y volume to better understand the effects of a displacement of the test-cycle trajectory on the XZ -plane of symmetry of the robot.

References

- [1] M. Callegari, M. Palpacelli, and M. Scarponi, "Kinematics of the 3-CPU parallel manipulator assembled for motions of pure translation," in *Proceedings of the IEEE International Conference on Robotics and Automation*, pp. 4020–4025, Barcelona, Spain, April 2005.
- [2] X.-J. Liu, J. Wang, F. Gao, and L.-P. Wang, "On the analysis of a new spatial three-degrees-of-freedom parallel manipulator," *IEEE Transactions on Robotics and Automation*, vol. 17, no. 6, pp. 959–968, 2001.
- [3] W. Li, F. Gao, and J. Zhang, "R-CUBE, a decoupled parallel manipulator only with revolute joints," *Mechanism and Machine Theory*, vol. 40, no. 4, pp. 467–473, 2005.
- [4] M. Carricato and V. Parenti-Castelli, "On the topological and geometrical synthesis and classification of translational parallel mechanisms," in *Proceeding of the 11th World Congress in Mechanism and Machine Science*, pp. 1624–1628, Tianjin, China, April 2004.
- [5] X.-J. Liu, J. Wang, and G. Pritschow, "A new family of spatial 3-DoF fully-parallel manipulators with high rotational capability," *Mechanism and Machine Theory*, vol. 40, no. 4, pp. 475–494, 2005.
- [6] X. Kong and C. Gosselin, *Type Synthesis of Parallel Mechanisms*, vol. 33 of *Springer Tracts in Advanced Robotics*, Springer, Berlin, Germany, 2007.
- [7] D. C. Yang and Z. C. Lai, "On the conditioning of robotic manipulators-service angle," *ASME Journal of Mechanisms, Transmissions, and Automation in Design*, vol. 107, pp. 262–270, 1985.
- [8] X.-J. Liu, Z.-L. Jin, and F. Gao, "Optimum design of 3-DOF spherical parallel manipulators with respect to the conditioning and stiffness indices," *Mechanism and Machine Theory*, vol. 35, no. 9, pp. 1257–1267, 2000.

- [9] T. Huang, Z. Li, M. Li, D. G. Chetwynd, and C. M. Gosselin, "Conceptual design and dimensional synthesis of a novel 2-DOF translational parallel robot for pick-and-place operations," *ASME Journal of Mechanical Design*, vol. 126, no. 3, pp. 449–455, 2004.
- [10] T. Yoshikawa, "Manipulability of robotic mechanisms," *International Journal of Robotics Research*, vol. 4, no. 2, pp. 3–9, 1985.
- [11] J. K. Salisbury and J. J. Craig, "Articulated hands: force and kinematic issues," *International Journal of Robotics Research*, vol. 1, no. 1, pp. 4–17, 1982.
- [12] J. Angeles, *Fundamentals of Robotic Mechanical Systems*, Springer, New York, NY, USA, 3rd edition, 2007.
- [13] J. P. Merlet, "Jacobian, manipulability, condition number, and accuracy of parallel robots," *ASME Journal of Mechanical Design*, vol. 128, no. 1, pp. 199–206, 2006.
- [14] G. Gogu, *Structural Synthesis of Parallel Robots—Part 1: Methodology*, Springer, Berlin, Germany, 2007.
- [15] T. Yoshikawa, "Dynamic manipulability of robot manipulators," in *Proceedings of the International Conference on Robotics and Automation*, pp. 1033–1038, St. Louis, Mo, USA, 1985.
- [16] G. J. Wiens, R. A. Scott, and M. Y. Zarrugh, "The role of inertia sensitivity in the evaluation of manipulator performance," *ASME Journal of Dynamic Systems, Measurement and Control*, vol. 111, no. 2, pp. 194–199, 1989.
- [17] O. Khatib and J. Burdick, "Optimization of dynamics in manipulator design: the operational space formulation," *The International Journal of Robotics and Automation*, vol. 2, pp. 90–98, 1987.
- [18] O. Ma and J. Angeles, "The concept of dynamic isotropy and its applications to inverse kinematics and trajectory planning," in *Proceedings of the IEEE International Conference on Robotics and Automation (ICRA '90)*, pp. 481–486, Cincinnati, Ohio, USA, 1990.
- [19] R. Di Gregorio and V. Parenti-Castelli, "Dynamic performance indices for 3-DOF parallel manipulators," in *Advances in Robot Kinematics: Theory and Applications*, J. Lenarcic and F. Thomas, Eds., pp. 11–20, Kluwer Academic Publishers, Dordrecht, The Netherlands, 2002.
- [20] R. Di Gregorio, "Dynamic model and performances of 2-dof mechanisms," in *Proceedings of the ASME Design Engineering Technical Conferences and Computers and Information in Engineering Conference*, Salt Lake City, Utah, USA, September–October 2004, paper no. DETC2004-57129.
- [21] A. Cammarata, J. Angeles, and R. Sinatra, "The dynamics of parallel Schönflies motion generators: the case of a two-limb system," *Proceedings of the Institution of Mechanical Engineers I*, vol. 223, no. 1, pp. 29–52, 2009.
- [22] G. H. Golub and C. F. Van Loan, *Matrix Computations*, The Johns Hopkins University Press, Baltimore, Md, USA, 1989.
- [23] W. A. Khan and J. Angeles, "The kinetostatic optimization of robotic manipulators: the inverse and the direct problems," *ASME Journal of Mechanical Design*, vol. 128, no. 1, pp. 168–178, 2006.

Research Article

Kinetostatic Analysis of 4-R(CRR) Parallel Manipulator with Overconstraints via Reciprocal-Screw Theory

Zhen Huang, Yan Zhao, and Jingfang Liu

Robotics Research Center, Yanshan University, Qinhuangdao, 066004, China

Correspondence should be addressed to Zhen Huang, huangz@ysu.edu.cn

Received 22 December 2008; Revised 29 May 2009; Accepted 18 September 2009

Academic Editor: Fengfeng Xi

Copyright © 2010 Zhen Huang et al. This is an open access article distributed under the Creative Commons Attribution License, which permits unrestricted use, distribution, and reproduction in any medium, provided the original work is properly cited.

The paper proposes a new approach based on reciprocal screw theory to analyze kinetostatics of lower-mobility parallel mechanisms with overconstraints and static indeterminacy. For force analysis of parallel mechanisms, the main reactions should be solved firstly, and then all other constraint reactions are easy to be obtained. The approach can remarkably reduce the number of unknowns and keep the number of simultaneous equilibrium equations not more than six each time. For static indeterminacy, it also needs to set some complementary equations. All active forces and constraint reactions of the kinematic pairs can be simultaneously obtained by analyzing the equilibrium of everybody one by one. A 4-R(CRR) parallel manipulator with collinear-force static indeterminacy is taken to introduce the method, which indicates that the method is simple and effective.

1. Introduction

Force analysis of lower-mobility parallel manipulators (PMs) is one of the important steps for mechanism design, simulation, and control. It generally needs to solve for active forces and constraint reactions of all kinematic pairs. Force analysis contains statics and dynamics. Only the statics analysis is needed when the device moves at low speed. However, when it moves at high speed, the inertia forces of links cannot be neglected, and it needs dynamics analysis.

The issue has attracted huge attention in the community. Tsai [1] presented the statics and dynamics of parallel mechanisms; Merlet [2] discussed the dynamics of PMs. Zhang and Gosselin [3, 4] discussed a general kinetostatic model of PMs. Gallardo et al. [5] solved the dynamics of PMs by screw theory and the principle of virtual work. Ider [6] developed a method for the inverse dynamic solution of PMs in the presence of drive singularities. Li et al. [7] presented a method for the inverse dynamic formulation of the 3-DOF modules of two PMs. Russo et al. [8] discussed the static balancing of parallel robots. Sokolov and Xirouchakis [9] presented a dynamics analysis of a 3-DOF PM. Lu et al. [10] solved active and passive forces of some PMs. Callegari and Cammarata [11] discussed the dynamics of a 3-CRU

parallel robot. Jaime et al. [12] approached the dynamic analysis of 2(3-RPS) manipulator via screw theory and the principle of virtual work. Zhou et al. [13] studied the static solving of a 3-DOF 3-RRR parallel mechanism. The statics of spatial mechanisms can be traded by various methods, such as the vector method [14], the dual vector and dual number quaternions [15], the screw calculus [16], and the principle of virtual work [17]. For dynamics analysis, the principle of d'Alembert is one of the common methods.

Most of the above-mentioned literatures only analyzed the actuator forces of lower-mobility PMs, but few discussed constraint reactions of kinematic pairs. The reaction analysis is very useful; however, it is quite complicated. Tsai [1] successfully analyzed constraint reactions of all the pairs for a serial robot by static equilibrium of free-body diagrams. Recently, we note that Lu [10] only discussed parts of constraint reactions of a mechanism, which is not overconstrained. In many applications, PMs not only have lots of kinematic pairs and unknowns but also are overconstrained and statically indeterminate, which increase the complexity and difficulty of reaction analysis. Particularly, the unknowns are correlative, and they oblige us to set high-order matrices. For example the number of the unknowns of a 5-DOF 5-5R PM is 130. However, the number of

its available equilibrium equations is only 126. Especially, for the simple 3-RRR spherical PM, the order of its static indeterminacy is up to six. For the static indeterminacy, it needs to set some complementary equations. Note that the static indeterminacy of the lower-DOF PMs can be classified into two cases: collinear forces and coaxial couples, and their analyses are also different. From this point of view, the issue is a completely new problem in the community.

This paper proposes a new simple and effective approach to analyze both the active forces and constraint reactions based on reciprocal screw theory. For this method, the main reactions should be solved firstly, and then all other constraint reactions are easy to be obtained. The method is able to remarkably reduce the number of unknowns and keep the number of simultaneous equations not more than six each time. All the constraint reactions are easy to be simultaneously obtained by analyzing the equilibrium of each body one by one. We name this case as force decoupling (see Section 3). Another merit of this method is the actual axes acted about by reaction forces and moments can be clearly determined from screw theory before the numerical calculation, and it is useful for other mechanism analyses and designs including singularity research.

A 4-DOF 4-R(CRR) parallel mechanism [18] is analyzed as an example. This manipulator is symmetrical [19], and the moving platform has two translations and two rotations. The 4-R(CRR) PM, which belongs to the case of collinear constraint forces, is of overconstraints and static indeterminacy.

2. Structure Description

2.1. A 4-R(CRR) Parallel Mechanism. The 4-R(CRR) parallel mechanism, as shown in Figure 1(a), consists of a moving platform, a fixed platform, and four identical branches with four kinematic pairs, R, C, R, and R. R indicates the revolute pair; C, the cylindrical pair, is equivalent to two single-DOF pairs, R and P (prismatic pair). The axis of the first pair R in each branch is normal to the base, and the axis of the second pair C is parallel to the base. The axes of the last three pairs intersect at a center point. The four branches have two center points, m and e .

The moving platform and the base are both square. The global coordinate system $O-XYZ$, moving system $o-xyz$, and limb systems $e-x_iy_iz_i$ and $m-x_iy_iz_i$ are all shown in Figure 1(a).

2.2. Mobility Analysis. In order to analyze the mobility, the Modified Grübler-Kutzbach Criterion [20, 21] based on screw theory [22, 23] is used. For the method, overconstraints are divided into two parts: common constraints and parallel constraints. They are named as the common constraint factor d and the parallel constraint factor ν , respectively. The Modified G-K Criterion is written as

$$M = d(n - g - 1) + \sum_{i=1}^g f_i + \nu, \quad (1)$$

where M denotes the mobility; n is the number of links including frame; g is the number of kinematic joints; f_i is the number of freedoms of the i th joint. d is the common constraint factor:

$$d = 6 - \lambda, \quad (2)$$

λ is the number of the common constraints of the mechanism. The common constraint is defined as a screw reciprocal to all the kinematic screws in the mechanism. ν is the number of the redundant constraints of the whole mechanism subtracting the number of the common constraints having been accounted. The redundant constraints of the whole mechanism can be obtained by screw analysis.

For 4-R(CRR), one of its limbs, say i , is shown in Figure 1(b). Its five single-DOF pairs are expressed into screw Plücker coordinates in $e-x_iy_iz_i$ or $m-x_iy_iz_i$ as follows

$$\begin{aligned} \mathcal{S}_1^i &= (0 \ 0 \ 1; \ 0 \ -x_{Ai} \ 0), \\ \mathcal{S}_2^i &= (1 \ 0 \ 0; \ 0 \ 0 \ 0), \\ \mathcal{S}_3^i &= (0 \ 0 \ 0; \ 1 \ 0 \ 0), \quad i = 1, 2, \dots, 4 \\ \mathcal{S}_4^i &= (l_{i4} \ m_{i4} \ n_{i4}; \ 0 \ 0 \ 0), \\ \mathcal{S}_5^i &= (l_{i5} \ m_{i5} \ n_{i5}; \ 0 \ 0 \ 0), \end{aligned} \quad (3)$$

where x_{Ai} relates a geometrical parameter and l_{ij} , m_{ij} , and n_{ij} are direction cosines, where j indicates the serial number of the kinematic pair in limb i . However, the values of x_{Ai} , l_{ij} , m_{ij} , and n_{ij} are not important for mobility analysis.

The five-screw system, Equation (3), has one reciprocal screw:

$$\mathcal{S}_1^{r1} = (0 \ 0 \ 1; \ 0 \ 0 \ 0), \quad (4)$$

where \mathcal{S}_1^{r1} is a constraint force applied to the platform by limb i , which is normal to the base and passes its center point, m or e .

Then four identical limbs exert four constraint forces in total on the same platform but passing through two different points, e and m . In the global system $O-XYZ$, they are

$$\begin{aligned} \mathcal{S}^{r1} &= (0 \ 0 \ 1; \ y_m \ -x_m \ 0), \\ \mathcal{S}^{r2} &= (0 \ 0 \ 1; \ y_e \ -x_e \ 0), \\ \mathcal{S}^{r3} &= (0 \ 0 \ 1; \ y_e \ -x_e \ 0), \\ \mathcal{S}^{r4} &= (0 \ 0 \ 1; \ y_m \ -x_m \ 0), \end{aligned} \quad (5)$$

where x_m , y_m and x_e , y_e relate to the geometrical parameters of the mechanism.

The four screws compose a constraint screw system $\widehat{\mathcal{S}}^R$, which is

$$\widehat{\mathcal{S}}^R = (\mathcal{S}^{r1}, \mathcal{S}^{r2}, \mathcal{S}^{r3}, \mathcal{S}^{r4})^T. \quad (6)$$

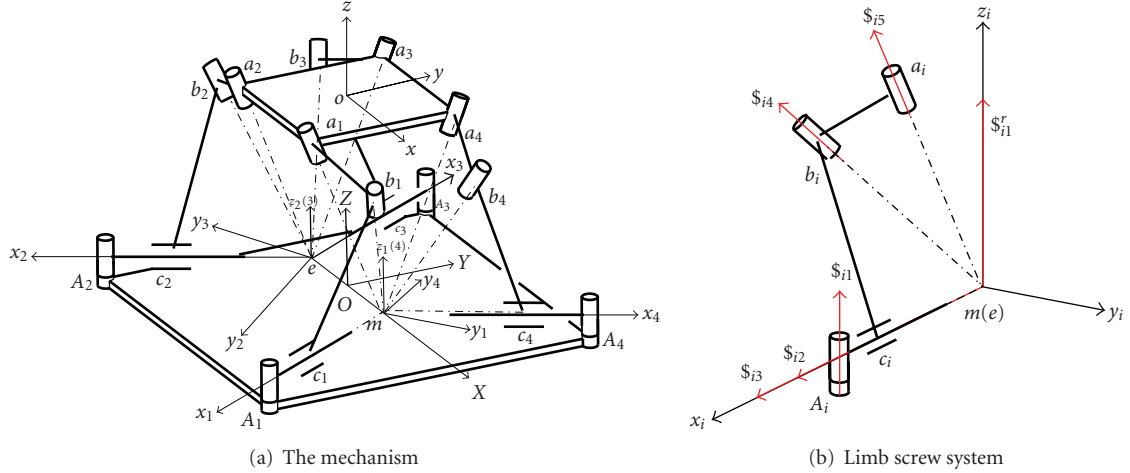


FIGURE 1: The 4-R(CRR) mechanism.

From $\widehat{\mathcal{S}}^R$, we find that the rank of system $\widehat{\mathcal{S}}^R$ is only two. That means that there is no common constraints and the common constraint factor is six. The number of the redundant constraints of the whole mechanism is two and then the parallel constraint factor is two. Then from the Modified G-K Criterion, Equation (1), the mobility of the mechanism is

$$M = 6(14 - 16 - 1) + 20 + 2 = 4. \quad (7)$$

Therefore, the mechanism has four degrees of freedom.

- (1) From the analysis we know that the platform is simultaneously acted upon by two linearly independent parallel constraint forces, which constrain one translational motion along Z-axis and one rotational motion about the normal direction of the plane determined by the two forces. Therefore, the mechanism is able to translate along two directions, X and Y, and rotate about two axes, X and Z.
- (2) After any possible motion including translation or rotation of the platform, the screw systems and the Modified G-K Formula denoted by (3)–(7) are all invariable. Therefore, the mobility is global.

2.3. Selection of Active Pairs. For the 4-DOF mechanism it needs four inputs. The input selection principle is that after locking all the selected inputs, if the platform is subjected to six linearly independent constraints in total and has no remnant freedom, the selection is correct; otherwise, it is wrong. From this point of view, there are many different selections. Here, the first revolute pairs of limbs 1, 2, and 3 and the single-freedom revolute pair of the cylindrical pair in limb 4 are selected as the four inputs. To prove the correctness of the selection, the selected four pairs need to be locked, and then the following analysis is carried out.

For limbs 1, 2, and 3, each limb-screw system has only four screws, that is the last four screws in (3). With respect to the limb coordinate system, the four screws are

$$\begin{aligned} \mathcal{S}_2^i &= (1 \ 0 \ 0; 0 \ 0 \ 0), \\ \mathcal{S}_3^i &= (0 \ 0 \ 0; 1 \ 0 \ 0), \\ \mathcal{S}_4^i &= (l_{i4} \ m_{i4} \ n_{i4}; 0 \ 0 \ 0), \\ \mathcal{S}_5^i &= (l_{i5} \ m_{i5} \ n_{i5}; 0 \ 0 \ 0), \end{aligned} \quad i = 1, 2, 3. \quad (8)$$

Two reciprocal screws of (8) are

$$\begin{aligned} \mathcal{S}_1^{ri} &= (0 \ 0 \ 1; 0 \ 0 \ 0), \\ \mathcal{S}_2^{ri} &= (0 \ 1 \ 0; 0 \ 0 \ 0), \end{aligned} \quad i = 1, 2, 3. \quad (9)$$

For limb 4, when the revolute part of the cylindrical pair is locked, the limb screw system becomes

$$\begin{aligned} \mathcal{S}_1^4 &= (0 \ 0 \ 1; 0 \ -x_{A_i} \ 0), \\ \mathcal{S}_3^4 &= (0 \ 0 \ 0; 1 \ 0 \ 0), \\ \mathcal{S}_4^4 &= (l_{44} \ m_{44} \ n_{44}; 0 \ 0 \ 0), \\ \mathcal{S}_5^4 &= (l_{45} \ m_{45} \ n_{45}; 0 \ 0 \ 0). \end{aligned} \quad (10)$$

Reciprocal screws of (10) are as follows:

$$\begin{aligned} \mathcal{S}_1^{r4} &= (0 \ 0 \ 1; 0 \ 0 \ 0), \\ \mathcal{S}_2^{r4} &= \left(0 \ 1 \ 0; \frac{x_{A_i}(m_{44}n_{45} - n_{44}m_{45})}{m_{45}l_{44} - l_{45}m_{44}} \quad \frac{-x_{A_i}(n_{45}l_{44} - l_{45}n_{44})}{m_{45}l_{44} - l_{45}m_{44}} \quad x_{A_i} \right), \end{aligned} \quad (11)$$

where the first one is a constraint force and the second one is a constraint wrench with pitch $h \neq 0$.

Since $\$1^2 = \1^3 , $\$1^1 = \1^4 , and the rank of the eight screws in (9) and (11) is six, the input selection is correct.

3. Force Analysis

The position, velocity, acceleration, and inertia force/moment of the mechanism should be determined before further force analysis, for which we can refer to [20, 24] or many other literatures.

The kinematic pairs connecting the platform and the limbs are named as the main kinematic pairs or main pairs, and the reaction in the main pair is named as the main-pair reaction or main reaction. For force analysis, the main reactions should be solved firstly, and then all other constraint reactions are easy to be obtained. In order to analyze the main reactions, it needs to calculate the main reactions brought about by all the external forces acting on the platform and on different limbs one by one, respectively and then summate them by superposition principle.

In general, everybody is acted upon by gravity, inertial force, and other external forces/moments, and all the forces can be vectorially summated as one 6D external force acting on the body. Our method is based on the principle of d'Alembert and the steps are as follows:

- (i) Analyze the mobility and select all the input pairs;
- (ii) Analyze the inertia force of each body based on [20, 24], if necessary, and then summate the inertia force, gravity and other external forces of each body to get the 6D resultant external force of that body.
- (iii) Analyze the reactions of main pairs produced by the external forces only exerted on the moving platform.
- (iv) Analyze the reactions of main pairs produced by the external forces only exerted on the links of limbs one by one.
- (v) Respectively, summate the main reactions obtained in steps (iii) and (iv), by the superposition principle to get the final main reactions.
- (vi) All the active couples and constraint reactions of other kinematic pairs can be directly obtained by setting corresponding equilibrium equations of the limb links one by one.

Since the 4-R(CRR) has thirteen movable bodies, twelve R-pairs, four C-pairs, and four unknown inputs, the number of unknowns is $12 \times 5 + 4 \times 4 + 4 = 80$ and the number of equations is $13 \times 6 = 78$. Then, two redundant unknowns are necessary. Therefore, it needs to set not only the equilibrium equations but also the complementary equations to solve the issue.

3.1. Force Expression. Generally, every body may be subject to forces including external forces, inertia force and gravity, and so forth, and then the 2nd step of the last Section is needed for every link. Nevertheless, without loss of generality, for brief introduction, we only consider that the 2nd step has been completed and the given forces are only the resultant

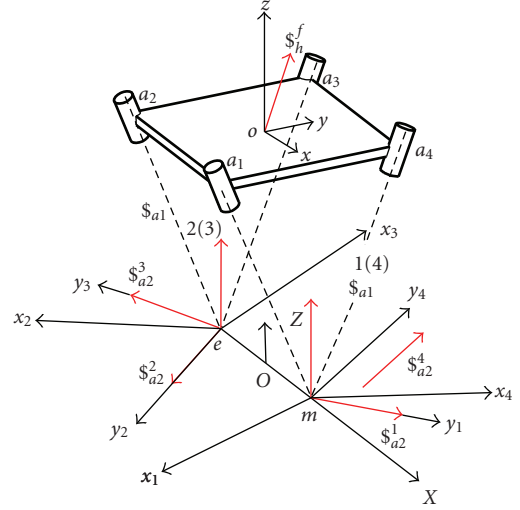


FIGURE 2: Free-body diagram of the platform (1).

external forces acting on the platform as well as on link a_1b_1 , that is, t in limb 1. Forces $\mathbf{f}_h = (f_{hx}, f_{hy}, f_{hz})^T$ and $\mathbf{f}_t^1 = (f_{tx}^1, f_{ty}^1, f_{tz}^1)^T$ and moments $\mathbf{m}_h = (m_{hx}, m_{hy}, m_{hz})^T$ and $\mathbf{m}_t^1 = (m_{tx}^1, m_{ty}^1, m_{tz}^1)^T$ are the external forces/moments including the inertia force/moment and the gravity in the global system and act on the mass centers of platform h and link t of limb 1, respectively.

Let $F_h \$h^f$ and $F_t^1 \$t^1$ denote the corresponding resultant external force screws with intensities, respectively. Then

$$\begin{aligned} F_h \$h^f &= \mathbf{f}_h + \in \mathbf{m}_h, \\ F_t^1 \$t^1 &= \mathbf{f}_t^1 + \in \mathbf{r}_{ct}^c \times \mathbf{f}_t^1 + \mathbf{m}_t^1, \end{aligned} \quad (12)$$

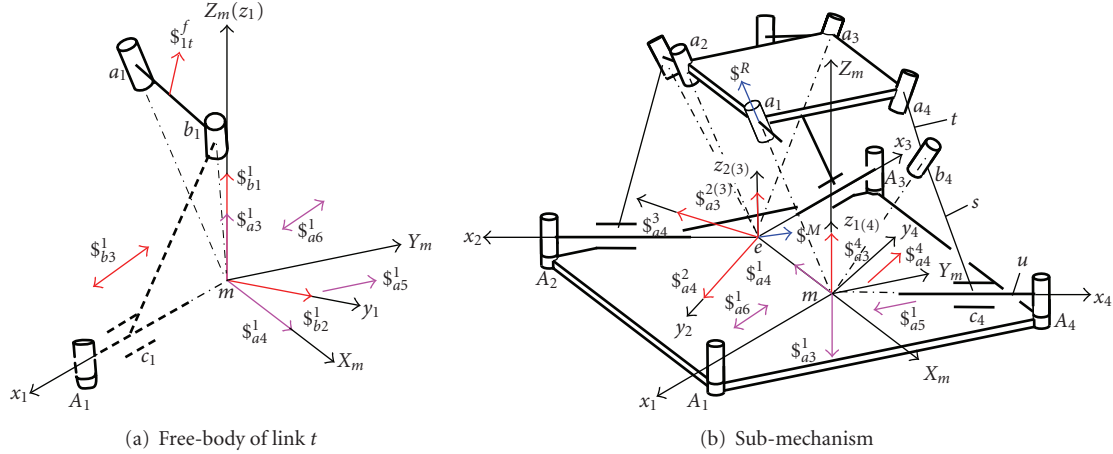
where \mathbf{r}_{ct}^c is the radius vector from the origin of the global system to the mass center point of link t ; \in is the Clifford factor.

3.2. Main-Pair Reaction

3.2.1. Main-Pair Reactions Produced by Platform Force. Equations (9) and (11) denote main reactions, and each main pair contains two reactions. $\$i_1^r$ and $\$i_2^r$ in (9) are unit constraint screws along z_i - and y_i -axes, respectively. In (11), $\$4_1^r$ is also a unit screw along z_i -axis, and $\$4_2^r$ is a screw with $h \neq 0$. All the eight screws are denoted in Figure 2. Their intensities are unknown.

However, the maximum linearly independent number of the eight constraints is six. From this point of view, there are only six independent unknowns and the issue is solvable.

Here, we use $\$i_{a1}^i$ and $\$i_{a2}^i$, $i = 1 \sim 4$, to denote $\$1^i$ and $\$2^i$, in the global system. The corresponding intensities of the reactions are f_{a1}^i and f_{a2}^i . f_{a1}^{14} and f_{a1}^{23} are the resultant forces of f_{a1}^1 , f_{a1}^4 and f_{a1}^2 , f_{a1}^3 , respectively. The free-body diagram of the moving platform is shown in Figure 2.

FIGURE 3: The sub-mechanism and link t in branch 1.

Considering the equilibrium of the platform, we have

$$\sum_{i=1}^4 f_{a2}^i \mathcal{S}_{a2}^i + f_{a1}^{14} \mathcal{S}_{a1}^1 + f_{a1}^{23} \mathcal{S}_{a1}^2 + F_h \mathcal{S}_h^f = 0. \quad (13)$$

Equation (13) is a screw equation and it is equivalent to six linear equations. The six unknowns can be solved.

If we use the traditional approach, each R pair has five unknown reactions and there are twenty unknowns corresponding six equilibrium equations of the moving platform. It is insolvable directly. Therefore, for solvability, it has to consider the equilibrium of other bodies, even all other bodies simultaneously. Considering the situation, this may be named as *force coupling*. Obviously, the new method described here is able to reduce unknowns and makes the solution decoupled and easy.

From (13), we can solve the six unknowns including f_{a1}^{14} and f_{a1}^{23} . In order to get f_{a1}^1 , f_{a1}^2 , f_{a1}^3 , and f_{a1}^4 , it needs to resolve f_{a1}^{14} into limbs 1 and 4 as well as f_{a1}^{23} into limbs 2 and 3. Here it is just the “static indeterminacy.” This resolution can be carried out through analyzing the stiffnesses of two corresponding parts. The two forces are in direct proportion to two corresponding stiffnesses.

However, in order to simplify the analysis and considering our core object not for stiffness analysis, here a hypothesis is given; that is, the stiffness proportion of the two parts is η . Therefore, the complementary equations are as follows [25]:

$$\begin{aligned} f_{a1}^1 &= \eta_1 f_{a1}^4, \\ f_{a1}^2 &= \eta_2 f_{a1}^3. \end{aligned} \quad (14)$$

3.2.2. Main-Pair Reactions Produced by Limb Force. Suppose that link a_1b_1 in limb 1 is subject to an external force $F_t^1 \mathcal{S}_{1t}^f$, and the force will also bring about main reactions. Main-pair reactions at a_1 can be obtained by solving the equilibrium equations of link a_1b_1 under the applied force $F_t^1 \mathcal{S}_{1t}^f$. A free-body diagram of link a_1b_1 is shown in Figure 3(a). We should analyze the property of the reactions of R pairs at a_1 and b_1 , respectively. If there is not any external forces in limbs,

Sections 3.2.2 and 3.2.3 are not necessary and the steps are simple.

- (1) *Reactions of revolute pair at a_1 .* The R pair at a_1 connects link a_1b_1 and a submechanism, 3-R(CRR), Figure 3(b). First, it needs to calculate the mobility of the 3-R(CRR) mechanism. From (1), we also have

$$M = 6 \times (11 - 12 - 1) + 15 + 1 = 4. \quad (15)$$

It is still a 4-DOF mechanism. There are only three input pairs in the subchain. After the three input pairs are locked, it has one freedom. Respectively, the platform of the submechanism is subjected to five constraints. From (9) and (11), the five linearly independent reactions include \mathcal{S}_1^i , $i = 2, 4$, which are upward and pass through the corresponding two origins, \mathcal{S}_2^i , $i = 2, 3$, which are along the corresponding y_i -axes, respectively, and \mathcal{S}_4^r , which is a screw with $h \neq 0$ (bi-directional arrow) and parallel to y -axis.

In the system m - $X_m Y_m Z_m$, Figure 3(b), the five constraint screws red can be expressed as

$$\begin{aligned} \mathcal{S}_1^2 &= (0 \ 0 \ 1; 0 \ l_a \ 0), \\ \mathcal{S}_1^4 &= (0 \ 0 \ 1; 0 \ 0 \ 0), \\ \mathcal{S}_2^2 &= (l_{22}^{mr} \ m_{22}^{mr} \ 0; 0 \ 0 \ -l_a m_{22}^{mr}), \\ \mathcal{S}_2^3 &= (l_{32}^{mr} \ m_{32}^{mr} \ 0; 0 \ 0 \ -l_a m_{32}^{mr}), \\ \mathcal{S}_2^4 &= (l_{42}^{mr} \ m_{42}^{mr} \ n_{42}^{mr}; p_{42}^{mr} \ q_{42}^{mr} \ r_{42}^{mr}), \end{aligned} \quad (16)$$

where \mathcal{S}_j^i denotes the j th constraint screw in the i th limb. $(\begin{smallmatrix} m_{ij}^{mr} & m_{ij}^{mr} & n_{ij}^{mr} \end{smallmatrix})^T$ is the direction cosine. l_a is the distance between points e and m .

The five-system is denoted as $\hat{\mathcal{S}}^c = (\mathcal{S}_1^2, \mathcal{S}_1^4, \mathcal{S}_2^2, \mathcal{S}_2^3, \mathcal{S}_2^4)^T$. The reciprocal screw of $\hat{\mathcal{S}}^c$ is \mathcal{S}^M . From $\hat{\mathcal{S}}^c \circ \mathcal{S}^M = 0$ [23], \mathcal{S}^M can be obtained as

$$\mathcal{S}^M = \left(-\frac{r_{42}^{mr} + l_a m_{42}^{mr}}{p_{42}^{mr}} \ 0 \ 1; 0 \ l_a \ 0 \right), \quad (17)$$

where $\M is a twist screw of the platform of the 3-R(CRR) mechanism and it is a line vector in plane $X_m Z_m$ and passing through point e . Meanwhile, the subchain uses another revolute pair R at a_1 to connect link t . Its screw $\m_R in $m-X_m Y_m Z_m$ is

$$\$^m_R = (l^m_R \quad m^m_R \quad n^m_R; \quad 0 \quad 0 \quad 0). \quad (18)$$

Therefore the twist system of the sub-chain is a two-screw system including the screws in (17) and (18). Reciprocal screws of the system are four main reactions (pink) acting on link $a_1 b_1$ at point a_1 . They are

$$\begin{aligned} \$^1_{a3} &= (0 \quad 0 \quad 1; \quad 0 \quad 0 \quad 0), \\ \$^1_{a4} &= (1 \quad 0 \quad 0; \quad 0 \quad 0 \quad 0), \\ \$^1_{a5} &= \left(0 \quad 1 \quad 0; \quad \frac{p_{42}^{mr} l_a}{r_{42}^{mr} + l_a m_{42}^{mr}} \quad \frac{-p_{42}^{mr} l_a l^m_R}{m^m_R (r_{42}^{mr} + l_a m_{42}^{mr})} \quad 0 \right), \\ \$^1_{a6} &= \left(0 \quad 0 \quad 0; \quad \frac{p_{42}^{mr}}{A} \quad \frac{p_{42}^{mr} l^m_R + n^m_R r_{42}^{mr} + n^m_R l_a m_{42}^{mr}}{A m^m_R} \quad \frac{(r_{42}^{mr} + l_a m_{42}^{mr})}{A} \right), \end{aligned} \quad (19)$$

where $\$^1_{a3}$ and $\$^1_{a4}$ are reactions passing point m and along axes Z_m and X_m , respectively; $\$^1_{a5}$ is a constraint force screw, $h \neq 0$, along Y_m ; $\$^1_{a6}$ is a couple normal to $\M and $\m_R ;

A

$$= \sqrt{(p_{42}^{mr})^2 + \frac{(p_{42}^{mr} l^m_R + n^m_R r_{42}^{mr} + n^m_R l_a m_{42}^{mr})^2}{(m^m_R)^2} + (r_{42}^{mr} + l_a m_{42}^{mr})^2}. \quad (20)$$

Suppose that the four screws with their intensities are expressed as $f_{a3}^1 \$^1_{a3}$, $f_{a4}^1 \$^1_{a4}$, $f_{a5}^1 \$^1_{a5}$, and $m_{a6}^1 \$^1_{a6}$ in the global system. In addition, there are only four unknowns, f_{a3}^1 , f_{a4}^1 , f_{a5}^1 , and m_{a6}^1 , for the R pair.

(2) *Reactions of revolute pair at b_1 .* Reactions of the revolute pair at b_1 are determined by analyzing the subchain RCR in limb 1. When the input pair is locked, there are only three basic pairs, whose screws are just the three screws in the middle of (3). Their three reciprocal screws, constraints, in the limb system are written as follows:

$$\begin{aligned} \$^1_{b1} &= (0 \quad 0 \quad 1; \quad 0 \quad 0 \quad 0), \\ \$^1_{b2} &= (0 \quad 1 \quad 0; \quad 0 \quad 0 \quad 0), \\ \$^1_{b3} &= (0 \quad 0 \quad 0; \quad 0 \quad -n_9 \quad m_9), \end{aligned} \quad (21)$$

where $\$^1_{b1}$ is a reaction force at b_1 , acting on link $a_1 b_1$, normal to the base and passing through the limb origin point; $\$^1_{b2}$ is also a reaction force passing through the origin and along y_1 -axis; $\$^1_{b3}$ is a reaction couple in plane $Y-Z$.

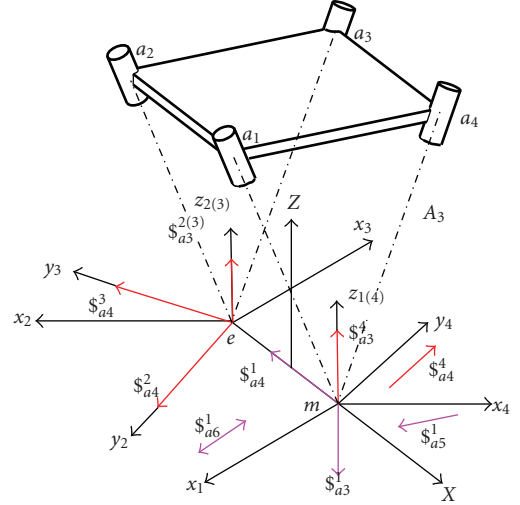


FIGURE 4: Free-body diagram of the platform (2) (Red denotes unknowns).

Suppose that we use f_{b1}^{1t} , f_{b2}^{1t} , and m_{b3}^{1t} to denote their intensities only caused by external force $F_t^1 \$^f_{1t}$ in the global system. Then the three reactions at b_1 pair acting on link $a_1 b_1$ are $f_{b1}^{1t} \$^1_{b1}$, $f_{b2}^{1t} \$^1_{b2}$, and $m_{b3}^{1t} \$^1_{b3}$. Since $\$^1_{a3}$ and $\$^1_{b1}$ are collinear, use f_{a3b1}^{1t} to denote the resultant intensity of $\$^1_{a3}$ and $\$^1_{b1}$.

(3) *Equilibrium of link $a_1 b_1$.* As shown in Figure 3(a), the reactions of the revolute pairs at a_1 and b_1 of limb 1 can be obtained. The equilibrium equation with six unknowns of link $a_1 b_1$ is

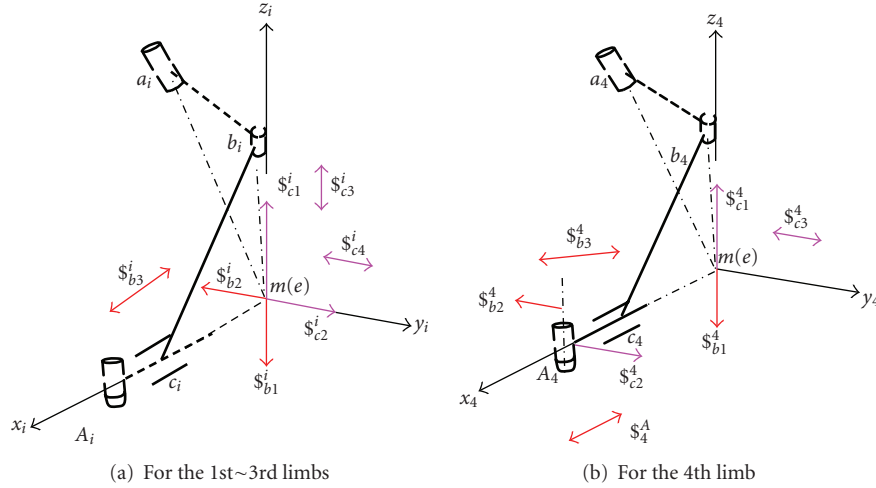
$$\begin{aligned} f_{a3b1}^{1t} \$^1_{a3} + f_{a4}^{1t} \$^1_{a4} + f_{a5}^{1t} \$^1_{a5} + m_{a6}^1 \$^1_{a6} \\ + f_{b2}^{1t} \$^1_{b2} + m_{b3}^{1t} \$^1_{b3} + F_t^1 \$^f_{1t} = 0. \end{aligned} \quad (22)$$

In the equation, there are six linearly independent unknowns and the main-reactions are solvable. From (22) f_{a3b1}^{1t} is obtained, but it still needs to separate f_{a3b1}^{1t} into f_{a3}^{1t} and f_{b1}^{1t} . The new issue in the mechanism analysis is also the “static indeterminacy,” but a special one with collinear forces. This can be solved by stiffness analysis. Similar to (14), we have

$$f_{a3}^1 = \eta_3 f_{b1}^{1t}. \quad (23)$$

(4) The external force acting on link $a_1 b_1$ also brings about the main reactions in limbs 2, 3, and 4. In order to further analyze the main reactions in limbs 2, 3, and 4, we can consider the equilibrium of the platform once again; Figure 4. Here f_{a3}^{23} denotes the resultant force of f_{a3}^2 and f_{a3}^3 . Four forces acting on the platform have been solved from (22). Considering the equilibrium equation with five unknowns of the platform, we have

$$-\sum_{i=3}^5 f_{ai}^1 \$^1_{ai} - m_{a6}^1 \$^1_{a6} + f_{a3}^{23} \$^2_{a3} + f_{a3}^4 \$^4_{a3} + \sum_{i=2}^4 f_{a4}^i \$^i_{a4} = 0. \quad (24)$$


 FIGURE 5: Free body diagram of link $b_i c_i$ in limbs.

How to obtain f_{a3}^2 and f_{a3}^3 from f_{a3}^{23} is similar to be obtained by similar stiffness analysis:

$$f_{a3}^2 = \eta_4 f_{a3}^3. \quad (25)$$

Nevertheless, comparing with (14), it is clear that $\eta_4 = \eta_2$, as they correspond to the same situations and have the same proportion.

3.2.3. Resultant Main-Pair Reactions by Superposition Principle. In Sections 3.2.1 and 3.2.2, main reactions brought about by the platform force and limb force have been solved by (13), (22), and (24). From superposition principle the resultant reaction at point a_1 is

$$f^1 \mathbf{s}_1^R = - \sum_{i=1}^2 f_{ai}^1 \mathbf{s}_{ai}^1 + \sum_{i=3}^5 f_{ai}^1 \mathbf{s}_{ai}^1 + m_{a6}^1 \mathbf{s}_{a6}^1. \quad (26)$$

The resultant main reaction at point a_i , $i = 2, 3, 4$ is

$$f^i \mathbf{s}_i^R = - \sum_{j=1}^4 f_{aj}^i \mathbf{s}_{aj}^j \quad j = 2, 3, 4. \quad (27)$$

3.3. Active Moments and Reactions of Other Pairs in Limbs. When the constraint reactions of the four main pairs are obtained, the four active moments and reactions of other pairs can be easily obtained by solving the equilibrium equations of the links in every limb from up to down one by one. If it does not need to calculate the constraint reactions of pairs in limbs, the active forces can be directly obtained by the principle of virtual work. Actually, when the forces of the main joints are solved, each limb becomes a serial-chain, and its dynamics analysis would be much simple by directly setting equilibrium of each body. However, here we want to show the number of equilibrium equation can be less than six by this method.

3.3.1. Reactions of Revolute Pair at b_i . Resultant main-reactions of the revolute pair at a_i have been got by (13), (22), and (24), then for obtaining the total unknown reactions at b_i we have to set the equilibrium equation of link $a_i b_i$ once again.

For limb 1, there are ten forces acting on link $a_1 b_1$ including a known external force $F_t^1 \mathbf{s}_{1t}^f$ and six main-reactions at point a_1 , (13) and (22), and three unknown reactions at b_1 , (21). Then the equilibrium equation of $a_1 b_1$ is as follow:

$$- \sum_{i=1}^2 f_{ai}^1 \mathbf{s}_{ai}^1 + \sum_{i=3}^5 f_{ai}^1 \mathbf{s}_{ai}^1 + m_{a6}^1 \mathbf{s}_{a6}^1 + \sum_{j=1}^2 f_{bj}^1 \mathbf{s}_{bj}^1 + m_{b3}^1 \mathbf{s}_{b3}^1 + F_t^1 \mathbf{s}_{1t}^f = 0, \quad (28)$$

where f_{bj}^1 , $j = 1, 2$, and m_{b3}^1 are caused by both $F_h \mathbf{s}_h^f$ and $F_t^1 \mathbf{s}_{1t}^f$.

For limbs 2, 3, and 4, considering (13) and (24), the balancing equation with three unknown reactions of link $a_i b_i$ is

$$- \sum_{j=1}^4 f_{aj}^i \mathbf{s}_{aj}^j + \sum_{j=1}^2 f_{bj}^i \mathbf{s}_{bj}^j + m_{b3}^i \mathbf{s}_{b3}^i = 0 \quad i = 2 \sim 4. \quad (29)$$

3.3.2. Reactions of Cylindrical Pair at c_i . For analyzing the reactions of the cylindrical pair at c_i , it needs to consider the kinematic chain RC in each limb.

Limbs 1, 2, and 3. The 1st pair at A_i is the active pair; Figure 5(a). When the actuated joint is locked, there are only

two single-freedom pairs, R and P in chain RC. The twist system includes the 2nd and 3rd screws in (3), and their four unknown reciprocal screws (pink) are

$$\begin{aligned} \mathcal{S}_{i1}^{Cr} &= (0 \ 0 \ 1; \ 0 \ 0 \ 0), \\ \mathcal{S}_{i2}^{Cr} &= (0 \ 1 \ 0; \ 0 \ 0 \ 0), \\ \mathcal{S}_{i3}^{Cr} &= (0 \ 0 \ 0; \ 0 \ 0 \ 1), \\ \mathcal{S}_{i4}^{Cr} &= (0 \ 0 \ 0; \ 0 \ 1 \ 0), \end{aligned} \quad i = 1, 2, 3, \quad (30)$$

where \mathcal{S}_{i1}^{Cr} and \mathcal{S}_{i2}^{Cr} are two reaction forces passing through the origin of the limb system along z_i and y_i , respectively; \mathcal{S}_{i3}^{Cr} and \mathcal{S}_{i4}^{Cr} are constraint couples also about axes z_i and y_i .

Assume that the four reaction screws of the cylindrical pair at c_i in (30) are denoted as \mathcal{S}_{cj}^i , $i = 1 \sim 3$, $j = 1 \sim 4$, in the global system and their intensities are f_{cj}^i , $i = 1 \sim 3$, $j = 1, 2$, and m_{cj}^i , $i = 1 \sim 3$, $j = 3, 4$. Considering the equilibrium of link $b_i c_i$, Figure 5(a), the four unknown reactions of pair C can be obtained by

$$\begin{aligned} - \sum_{j=1}^2 f_{bj}^i \mathcal{S}_{bj}^i - m_{b3}^i \mathcal{S}_{b3}^i + \sum_{j=1}^2 f_{cj}^i \mathcal{S}_{cj}^i \\ + \sum_{j=3}^4 m_{cj}^i \mathcal{S}_{cj}^i = 0, \quad i = 1 \sim 3. \end{aligned} \quad (31)$$

Limb 4. The single-freedom revolute pair of the cylindrical pair is the actuated joint and can be locked similarly like the section above. However, here we prefer not to lock the input and consider that there is an unknown applied force, $m_4^A \mathcal{S}_4^A$. Then the three-system twist of RC chain consists of the first three screws in (3), and the C pair has three unknown reciprocal screws (pink), Figure 5(b), as follows:

$$\begin{aligned} \mathcal{S}_{41}^{Cr} &= (0 \ 0 \ 1; \ 0 \ 0 \ 0), \\ \mathcal{S}_{42}^{Cr} &= (0 \ 1 \ 0; \ 0 \ 0 \ x_{Ai}), \\ \mathcal{S}_{43}^{Cr} &= (0 \ 0 \ 0; \ 0 \ 1 \ 0). \end{aligned} \quad (32)$$

Considering the equilibrium of link $b_4 c_4$, the four unknowns, one active couple and three reactions, in pair C can be obtained as follows:

$$- \sum_{j=1}^2 f_{bj}^4 \mathcal{S}_{bj}^4 - m_{b3}^4 \mathcal{S}_{b3}^4 + \sum_{j=1}^2 f_{cj}^4 \mathcal{S}_{cj}^4 + m_{c3}^4 \mathcal{S}_{c3}^4 + m_4^A \mathcal{S}_4^A = 0, \quad (33)$$

where $m_4^A \mathcal{S}_4^A$ is the active moment of limb 4. \mathcal{S}_{cj}^4 , $j = 1 \sim 3$, denote three reaction screws of the cylindrical pair at c_4 in the global system and their intensities are f_{cj}^4 , $j = 1, 2$, and m_{c3}^4 .

3.3.3. *Active Moments and Reactions of Revolute Pair at A_i .* In the limb system, the R pair has five constraints, such as

$$\begin{aligned} \mathcal{S}_{i1}^R &= (0 \ 0 \ 1; \ 0 \ 0 \ 0), \\ \mathcal{S}_{i2}^R &= (1 \ 0 \ 0; \ 0 \ 0 \ 0), \\ \mathcal{S}_{i3}^R &= (0 \ 1 \ 0; \ 0 \ 0 \ 0), \quad i = 1, 2, 3, 4, \\ \mathcal{S}_{i4}^R &= (0 \ 0 \ 0; \ 1 \ 0 \ 0), \\ \mathcal{S}_{i5}^R &= (0 \ 0 \ 0; \ 0 \ 1 \ 0), \end{aligned} \quad (34)$$

where \mathcal{S}_{i1}^R , \mathcal{S}_{i2}^R , and \mathcal{S}_{i3}^R are reaction forces passing point A_i and along three coordinate axes, respectively. \mathcal{S}_{i4}^R and \mathcal{S}_{i5}^R are couples about axes x_i and y_i , respectively.

Assume \mathcal{S}_{Aj}^i , $i = 1 \sim 4$, $j = 1 \sim 5$, denote \mathcal{S}_{ij}^R , $i = 1 \sim 4$, $j = 1 \sim 5$, and their intensities are f_{Aj}^i , $i = 1 \sim 4$, $j = 1, 2, 3$, and m_{Aj}^i , $i = 1 \sim 4$, $j = 4, 5$, in the global system. The active couple is $m_i^A \mathcal{S}_i^A$, $i = 1 \sim 4$.

For limbs 1, 2, and 3, Figure 6(a), the equilibrium equation with six unknowns including input couple of link $A_i c_i$ is

$$\begin{aligned} \sum_{j=1}^3 f_{Aj}^i \mathcal{S}_{Aj}^i + \sum_{j=4}^5 m_{Aj}^i \mathcal{S}_{Aj}^i - \sum_{j=1}^2 f_{cj}^i \mathcal{S}_{cj}^i \\ - \sum_{j=3}^4 m_{cj}^i \mathcal{S}_{cj}^i + m_i^A \mathcal{S}_i^A = 0, \quad i = 1 \sim 3. \end{aligned} \quad (35)$$

For limb 4, Figure 6(b), the equilibrium equation with five unknowns of link $A_4 c_4$ is

$$\sum_{j=1}^3 f_{Aj}^4 \mathcal{S}_{Aj}^4 + \sum_{j=4}^5 m_{Aj}^4 \mathcal{S}_{Aj}^4 - \sum_{j=1}^2 f_{cj}^4 \mathcal{S}_{cj}^4 - m_{c3}^4 \mathcal{S}_{c3}^4 - m_4^A \mathcal{S}_4^A = 0, \quad (36)$$

where $m_4^A \mathcal{S}_4^A$ is an unknown input couple exerted on link $A_4 c_4$ by the active device.

4. Numerical Example

Assume that the distance Oo is 0.55 m; $l_a=0.4$ m, $l_A=0.9$ m; vector mb_4 is $(l_{44}^O, m_{44}^O, n_{44}^O)^T$, vector ma_4 is $(0, m_{45}^O, n_{45}^O)^T$, and their values are $(22.95/50, 13.91/50, 42.19/50)^T$ and $(0, 20/\sqrt{20^2 + 50^2}, 50/\sqrt{20^2 + 50^2})^T$, and $F_h \mathcal{S}_h^f = (40, 50, 55, 30, 40, 45)^T$ (N and N·m). a is the distance between point A_i $i = 1, 4$ and origin point m , or point A_i $i = 2, 3$ and origin n :

$$a = \sqrt{\left(\frac{l_A - l_a}{2}\right)^2 + \left(\frac{l_A}{2}\right)^2}. \quad (37)$$

The constraint screws in (13) are as follows:

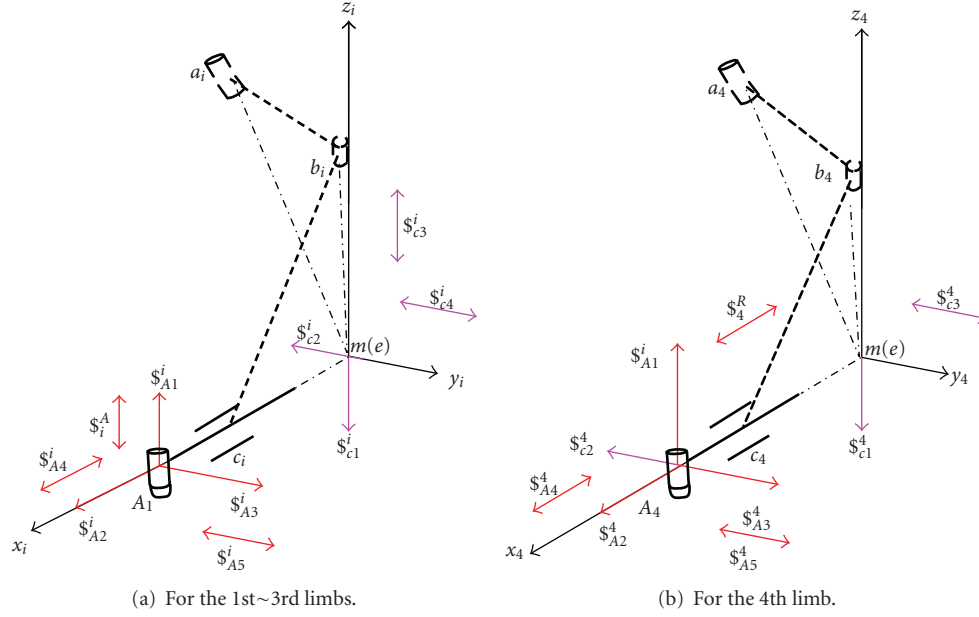
FIGURE 6: Free body diagram of link i in limbs.

TABLE 1: The results of active moments and constraint reactions of the kinematic pairs.

Wrench	Limb 1	Limb 2	Limb 3	Limb 4
f_{a1}^i/N	-16.152	-11.348	-11.348	-16.152
f_{a2}^i/N	-60.378	30.403	13.979	1.804
f_{b1}^i/N	-16.152	-11.348	-11.348	-16.152
f_{b2}^i/N	-60.378	-30.403	-13.979	1.804
$m_{b3}^i/N \cdot m$	-22.036	-11.096	-5.102	1.981
f_{c1}^i/N	-16.152	-11.348	-11.348	-16.152
f_{c2}^i/N	-60.378	-30.403	-13.979	1.804
$m_{c3}^i/N \cdot m$	-5.865	2.953	1.358	5.787
$m_{c4}^i/N \cdot m$	6.665	-4.655	-4.674	—
f_{A1}^i/N	-16.152	-11.348	-11.348	-16.152
f_{A2}^i/N	0	0	0	0
f_{A3}^i/N	-60.378	30.403	13.979	1.804
$m_{A4}^i/N \cdot m$	0	0	0	-2.175
$m_{A5}^i/N \cdot m$	-8.346	-5.816	-5.842	-9.180
$m_i^A/N \cdot m$	31.095	-15.649	-7.196	-2.175

$$\begin{aligned}
 \mathcal{S}_{a1}^{1(4)} &= \left(0 \ 0 \ 1; \ 0 \ -\frac{l_a}{2} \ 0 \right), & \mathcal{S}_{a1}^{2(3)} &= \left(0 \ 0 \ 1; \ 0 \ \frac{l_a}{2} \ 0 \right), \\
 \mathcal{S}_{a2}^1 &= \left(\frac{l_A}{2a} \ \frac{l_A - l_a}{2a} \ 0; \ 0 \ 0 \ 0 \ \frac{l_A l_a - l_a^2}{4a} \right), & \mathcal{S}_{a2}^2 &= \left(\frac{l_A}{2a} \ -\frac{l_A - l_a}{2a} \ 0; \ 0 \ 0 \ 0 \ \frac{l_A l_a - l_a^2}{4a} \right), \\
 \mathcal{S}_{a2}^3 &= \left(-\frac{l_A}{2a} \ -\frac{l_A - l_a}{2a} \ 0; \ 0 \ 0 \ 0 \ \frac{l_A l_a - l_a^2}{4a} \right), \\
 \mathcal{S}_{a2}^4 &= \left(-\frac{l_A}{2a} \ \frac{l_A - l_a}{2a} \ 0; \ -\frac{(m_{45}^O n_{44}^O - m_{44}^O n_{45}^O)(2l_A^2 - 2l_A l_a + l_a^2)}{4am_{45}^O l_{44}^O} \ \frac{-n_{45}^O(2l_A^2 - 2l_A l_a + l_a^2)}{4am_{45}^O} \ \frac{l_A(2l_A - l_a)}{4a} \right).
 \end{aligned} \tag{38}$$

The results of the active moments and reactions are listed in Table 1.

5. Discussion

Based on the mobility analysis, Equation (2), the number of overconstraints of the 4-R(CRR) mechanism is two. As the mechanism has 13 links including the frame, 12 revolute pairs and 4 cylindrical pairs, as well as 4 unknown active moments, the number of its unknowns, u , and the number of equilibrium equations, e , are as follows

$$\begin{aligned} u &= 12 \times 5 + 4 \times 4 + 4 = 80, \\ e &= 13 \times 6 = 78. \end{aligned} \quad (39)$$

It means there is a static indeterminacy, and we need two extra complementary equations, which could be set based on the theory of elastic mechanics. If so, the problem is solvable theoretically. However, in this case we should set a system of 80 equations including two complementary equations and solve the matrix with the rank up to 80. Evidently, it is very difficult.

In order to avoid the high-rank matrix and reducing the unknowns the new method is proposed. Firstly, based on screw theory the unknowns could be reduced. Secondly, when there are two external forces acting on two different bodies, the force analysis should carry through one by one. As shown in 4-R(CRR) example, first, we only consider the force acting on the platform, and two complementary equations, Equation (14), are needed. Then, consider the external force acting on link 1, another two complementary equations are needed, too, as (23) and (25). Therefore it needs four (actually three) complementary equations in total for this example. That means that the force analysis needs two complementary equations each time. Therefore, the total number of complementary equations may be more than the difference between the numbers of unknowns and equilibrium equations.

6. Conclusion

Based on reciprocal screw theory, the kinetostatic analysis method of parallel mechanisms with special static indeterminacy containing collinear forces has been investigated in the paper. Our method can remarkably reduce the number of unknowns and the number of simultaneous equilibrium equations is not more than six each time. All active forces and constraint reactions of kinematic pairs are easy to be simultaneously obtained by analyzing the equilibrium of everybody one by one. The solution steps are also very clear.

The typical 4-DOF 4-R(CRR) parallel manipulator with special static indeterminacy containing collinear forces has been taken as an example to introduce this strategy. After analyzing screw systems, determining main-reactions and setting complementary equations, all the active forces and constraint reactions of the kinematic pairs are simultaneously solvable. Evidently, the forces are decoupled by the method. Therefore, the method can avoid setting complex high-order matrices.

The complex special static indeterminacy of lower-DOF parallel mechanisms still calls for further research as an open problem.

Acknowledgments

This research is supported by NSFC (50875227). The authors would like to express their gratitude to Professor X. Z. Bai for valuable discussions.

References

- [1] L. W. Tsai, *Robot Analysis, the Mechanics of Serial and Parallel Manipulators*, John Wiley & Sons, New York, NY, USA, 1999.
- [2] J. P. Merlet, *Parallel Robots*, Springer, Paris, France, 2nd edition, 2006.
- [3] D. Zhang and C. M. Gosselin, "Kinetostatic modeling of N-DOF parallel mechanisms with a passive constraining leg and prismatic actuators," *ASME Journal of Mechanical Design*, vol. 123, no. 3, pp. 375–381, 2001.
- [4] D. Zhang and C. M. Gosselin, "Kinetostatic modeling of parallel mechanisms with a passive constraining leg and revolute actuators," *Mechanism and Machine Theory*, vol. 37, no. 6, pp. 599–617, 2002.
- [5] J. Gallardo, J. M. Rico, A. Frisoli, D. Checcacci, and M. Bergamasco, "Dynamics of parallel manipulators by means of screw theory," *Mechanism and Machine Theory*, vol. 38, no. 11, pp. 1113–1131, 2003.
- [6] S. K. Ider, "Inverse dynamics of parallel manipulators in the presence of drive singularities," *Mechanism and Machine Theory*, vol. 40, no. 1, pp. 33–44, 2005.
- [7] M. Li, T. Huang, J. Mei, X. Zhao, D. G. Chetwynd, and S. J. Hu, "Dynamic formulation and performance comparison of the 3-DOF modules of two reconfigurable PKM—the Tricept and the TriVariant," *ASME Journal of Mechanical Design*, vol. 127, pp. 1129–1136, 2005.
- [8] A. Russo, R. Sinatra, and F. Xi, "Static balancing of parallel robots," *Mechanism and Machine Theory*, vol. 40, no. 2, pp. 191–202, 2005.
- [9] A. Sokolov and P. Xirouchakis, "Dynamics analysis of a 3-DOF parallel manipulator with R-P-S joint structure," *Mechanism and Machine Theory*, vol. 42, no. 5, pp. 541–557, 2007.
- [10] Y. Lu, "Using Virtual Work Theory and CAD functionalities for solving active and passive force of spatial parallel manipulators," *Mechanism and Machine Theory*, vol. 42, no. 7, pp. 839–858, 2007.
- [11] M. Callegari and A. Cammarata, "Kinematics and dynamics of a 3-CRU spherical parallel robot," in *Proceedings of the ASME International Design Engineering Technical Conferences and Computers and Information in Engineering Conference*, Las Vegas, Nev, USA, September 2007, paper no. DETC2007-35894.
- [12] G. Jaime, R. A. Carlos, C. Luis, J. M. Rico, and Md. N. Islam, "Kinematics and dynamics of 2(3-RPS) manipulators by means of screw theory and the principle of virtual work," *Mechanism and Machine Theory*, vol. 43, no. 10, pp. 1281–1294, 2008.
- [13] Y. L. Zhou, L. Liu, and F. Gao, "Full static solving of 3-DOF spherical parallel mechanism 3-RRR," *Chinese Journal of Mechanical Engineering*, vol. 44, no. 6, pp. 169–176, 2008.
- [14] R. Beyer, "Statics and dynamics in 3-D mechanisms," in *Proceedings of the Transactions of the 6th Conference on*

- Mechanisms*, pp. 94–112, Purdue University, West Lafayette, Ind, USA, 1960.
- [15] A. T. Yang, “Static force and torque analysis of spherical four-bar mechanisms,” *ASME Journal of Engineering for Industry-Transactions*, vol. 87, no. 2, pp. 221–227, 1965.
- [16] S. K. Agrawal and B. Roth, “Statics of in-parallel manipulator systems,” *ASME Journal of Mechanical Design*, vol. 114, pp. 564–568, 1992.
- [17] H. Asada and J. J. E. Slotine, *Robot Analysis and Control*, John Wiley & Sons, New York, NY, USA, 1986.
- [18] Z. Huang and Q. C. Li, “Type synthesis of symmetrical lower-mobility parallel mechanisms using the constraint-synthesis method,” *International Journal of Robotics Research*, vol. 22, no. 1, pp. 59–79, 2003.
- [19] M. G. Mohamed and J. Duffy, “A direct determination of the instantaneous kinematics of fully-parallel robot manipulators,” *ASME Journal of Mechanisms, Transmissions, and Automation in Design*, vol. 107, no. 2, pp. 226–229, 1985.
- [20] Z. Huang, L. F. Kong, and Y. F. Fang, *Mechanism Theory and Control of Parallel Manipulators*, China Machine Press, Beijing, China, 1997.
- [21] Z. Huang, J. F. Liu, and Q. C. Li, “Unified methodology for mobility analysis based on screw theory,” in *Smart Devices and Machines for Advanced Manufacturing*, L. Wang and J. Xi, Eds., pp. 49–78, Springer, Berlin, Germany, 2008.
- [22] R. Ball, *A Treatise on the Theory of Screws*, Cambridge University Press, Cambridge, UK, 1990.
- [23] K. H. Hunt, *Kinematic Geometry of Mechanisms*, Oxford University Press, Oxford, UK, 1978.
- [24] Z. Huang and H. B. Wang, “Dynamic force analysis of n-DOF multi-loop complex spatial mechanisms,” *Mechanism and Machine Theory*, vol. 27, no. 1, pp. 97–105, 1992.
- [25] S. P. Timoshenko and J. M. Gere, *Theory of Elastic Stability*, McGraw-Hill, New York, NY, USA, 2nd edition, 1961.

Research Article

A Compliant PKM Mesomanipulator: Kinematic and Dynamic Analyses

C. Amici, A. Borboni, and R. Faglia

Dipartimento di Ingegneria Meccanica e Industriale, Università degli Studi di Brescia, Via Branze 38, 25123 Brescia, Italy

Correspondence should be addressed to C. Amici, cinzia.amici@ing.unibs.it

Received 1 April 2009; Revised 10 July 2009; Accepted 30 September 2009

Academic Editor: Rosario Sinatra

Copyright © 2010 C. Amici et al. This is an open access article distributed under the Creative Commons Attribution License, which permits unrestricted use, distribution, and reproduction in any medium, provided the original work is properly cited.

The kinematic and dynamic analyses of a PKM mesomanipulator are addressed in this paper: the proposed robot architecture allows only pure translations for the mobile platform, while the presence of flexure hinges introduces compliance into the structure. The analytical solutions to direct and inverse kinematic problems are evaluated after a brief introduction of the basic adopted nomenclature, the manipulator workspace and the robot singularity configurations are then described, and the analytical solution to the inverse dynamic problem is presented. Thereafter, an overview on some of the simulations results obtained through a software implementation of the described algorithms is addressed, and the most salient aspects of this topic are summarized in the final conclusions.

1. Introduction

Parallel manipulators assure high accuracy and high accelerations but a limited workspace [1]. The mesomanipulator herein concerned, as shown in Figure 1, results characterized by a parallel architecture, and by the presence of flexural hinges joints between the links, that introduce compliances into the structure [2].

A peculiar characteristic of the robot is the possibility to generate the final configuration from an original planar structure, through opportune plastic deformations in the proper flexure hinges.

In this paper, the kinematic analysis of the mesomanipulator will be addressed: forward and inverse analytical solutions will be presented, then the singular configurations and the robot workspace will be taken into account; once the dynamic analysis is described, the main elements of the mesomanipulator analysis will be finally presented.

The robot frame presents a strong symmetry, involving three kinematic chains (in the following leg 1, leg 2, and leg 3, as presented in the model scheme of Figure 2) that link each fixed element, called feet (P_i with $i = 1, 2, 3$ in agreement with the respective leg number), with the central mobile platform [3].

As shown in Figure 2, two four-bar mechanisms in cascade can be identified in every leg, and these are determined

by the so-called B_i , C_i , E_i , F_i and E_i , F_i , M_i , N_i points, while, on the other hand, an isostatic triangle can be defined by the A_i , D_i , and L_i points of every leg: the first structure allows the platform just pure translation movements [4], while the presence of the isostatic element nothing adds to the kinematic structure functionality and can therefore be neglected in a functional analysis [5].

Particular attention is paid to the evaluation of the structure degrees of freedom (dof): the model presented in Figure 3 illustrates the basic hypotheses that lead to assume 132 dof and 129 doc (degrees of constraint), in agreement with the total 3 dof of the functional structure [6]. As a matter of fact, the structural scheme in Figure 2 introduces fictitious functional multiple joints, due to the geometrical simplified connections adopted between the links and the mobile platform or between each leg and its foot; for this reason the functional scheme in Figure 3 does not prevent from the assumption of multiple and coinciding flexural joints.

2. Kinematic Analysis

The robot symmetry simplifies the kinematic problem allowing the identification of an analytical solution [7]: once defined the foot position into an absolute and fixed reference

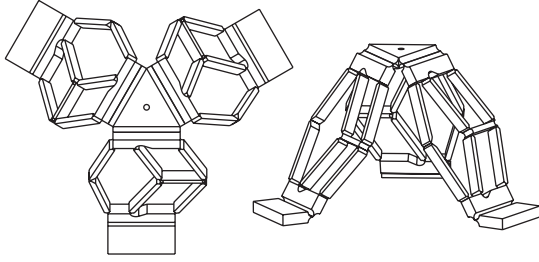


FIGURE 1: The PKM mesomanipulator.

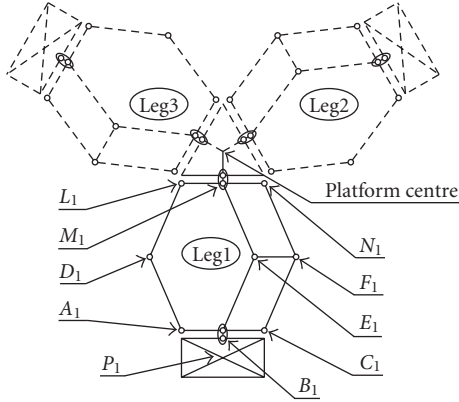


FIGURE 2: The manipulator planar structure: basic adopted nomenclature.

system, the position of the mobile platform centre, indicated by the column vector S as presented into the relation (1), results univocally identified by a tern of variable distances, whose expressions result strictly related to the actuators positioning:

$$S = \begin{bmatrix} x_s & y_s & z_s \end{bmatrix}'. \quad (1)$$

In particular, four different configurations have been identified for the three required actuators, as Figure 4 shows; all of them are referable to the first one presented, through the simple geometrical transformations described in Table 1, where Q indicates the column vector (2) collecting the joints parameters and R is the column vector (3) of the $B_i M_i$ distances (once again $i = 1, 2, 3$ in agreement with the leg number), while b and c identify, respectively, the links and the rocker arms lengths:

$$Q = \begin{bmatrix} q_1 & q_2 & q_3 \end{bmatrix}', \quad (2)$$

$$R = \begin{bmatrix} r_1 & r_2 & r_3 \end{bmatrix}'. \quad (3)$$

Observing that the geometrical constant values of the foot (the a lengths) and of the platform (the d lengths) do not influence the platform centre position, the equivalent and simplified model shown in Figure 5 can be considered [8]: the general kinematic relation (4) for the positions becomes therefore the system (5) of three equations, each of whom representing a sphere, with r_i radius (function of q_i) and

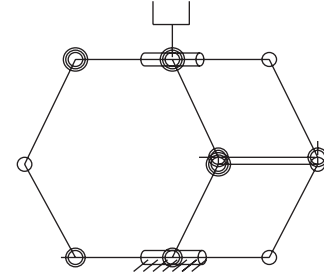


FIGURE 3: Functional leg scheme. From the top of the legend: F the frame, S the Spherical joints, U the Universal joints, and R the Rotoidal ones, with the rotational axis parallel or orthogonal respectively to the sheet plain.

TABLE 1: Joints parameters and characteristic distances: geometrical relations.

Configuration	Geometrical relations (with $i = 1, 2, 3$)
(A)	$r_i = 2 \cdot b \cdot \cos(q_i)$
(B)	$r_i = q_i$
(C)	$r_i = 2 \cdot \sqrt{b^2 - \left(\frac{q_i - c}{2}\right)^2}$
(D)	$r_i = 2 \cdot \sqrt{q_i^2 - c^2}$

centre in the i -feet in the simplified equivalent kinematic model, where $i = 1, 2, 3$:

$$S = F(Q), \quad (4)$$

$$(x_s - x_i)^2 + (y_s - y_i)^2 + (z_s - z_i)^2 = r_i^2. \quad (5)$$

For the sake of simplicity, the (B) configuration will be taken into account in the current analysis, even if the presented procedure could be adopted to analyze also the other configurations.

Under these hypotheses, the inverse kinematics can be easily reduced to the system (6), generating two solution vectors: the negative one has been neglected as unreachable for physical considerations:

$$q_i^2 = (x_s - x_i)^2 + (y_s - y_i)^2 + (z_s - z_i)^2. \quad (6)$$

Also the direct kinematics can be easily evaluated, as the system (7) describes; once again, the negative solution has been discarded:

$$\begin{aligned} x_s &= \frac{q_3^2 + q_2^2 - 2 \cdot q_1^2 - 2 \cdot x_2^2 - 2 \cdot y_2^2 + 2 \cdot x_1^2}{4 \cdot x_1 - x_2}, \\ y_s &= \frac{q_3^2 - q_2^2}{4 \cdot y_2}, \\ z_s &= \pm \sqrt{q_1^2 - y_s^2 - (x_s - x_1)^2}. \end{aligned} \quad (7)$$

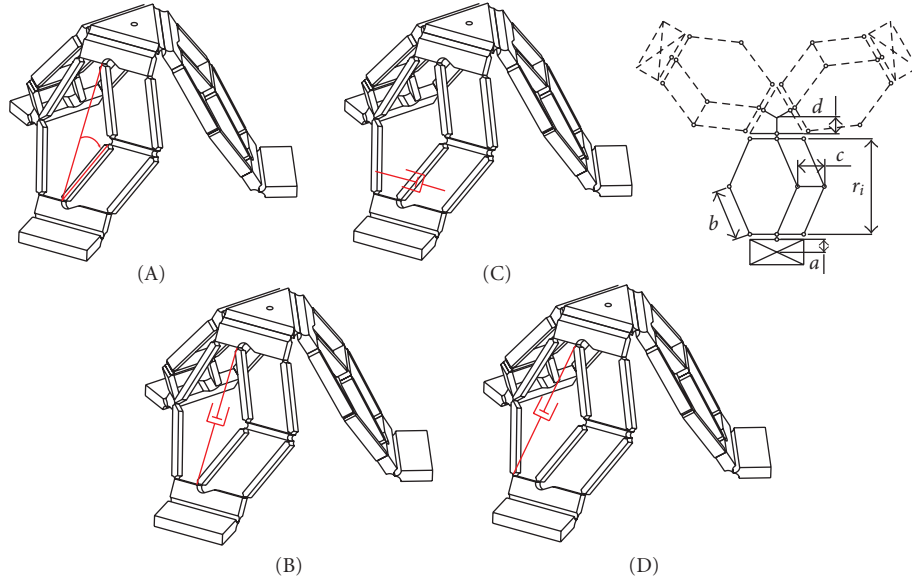


FIGURE 4: Manipulator actuation: the four identified configurations.

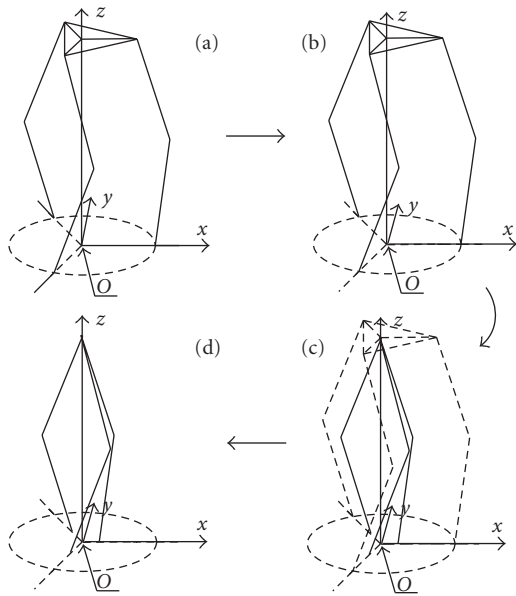


FIGURE 5: Consecutive geometrical simplifications allow to reach the simplified equivalent kinematic model (d) starting from the original configuration (a); in (b) the first translation removes the a lengths, while in (c) the second translation removes the d lengths.

The direct kinematic analysis for velocity \dot{S} and acceleration \ddot{S} requires the introduction of the Jacobian matrix J and its time derivate [9].

The velocity and acceleration inverse kinematics consists in the solution of the matrix relations (8) and (9), where the mathematical constraints to the inversion of the Jacobian matrix identify the robot singularities, as presented in the

followings:

$$\dot{Q} = J^{-1} \cdot \dot{S}, \quad (8)$$

$$\ddot{Q} = J^{-1} \cdot \ddot{S} + \dot{J}^{-1} \cdot \dot{S}. \quad (9)$$

3. Singularity Configurations and Robot Workspace

As previously introduced, not all the ideally reachable positions can be supported by the analytical algorithm chosen to solve the kinematics: in fact, the adopted actuators configuration directly influence the Jacobian matrix definition.

Considering, for instance, the (B) configuration, the Jacobian determinant becomes equal to zero when at least one of the relations (10), (11), or (12) is verified, that is, when the platform centre belongs to the plain identified by the three feet:

$$q_1 = \{0\}, \quad (10)$$

$$q_2 = \{0\}, \quad (11)$$

$$q_3 = \{0\}. \quad (12)$$

Changing the actuator configuration, the Jacobian matrix assumes different singularity conditions, as Table 2 presents.

Two observations are worth to be underlined, related to the actuators configuration.

First of all, it is to note how the (B) configuration, here chosen as the basic one, not only represents, from a computational viewpoint, the easiest adoptable solution but also avoids physically reachable singularities; then, choosing another actuators configuration the number of singularities

TABLE 2: Robot singularities.

Conf.	Singularity Conditions
(A)	$q_1 = \{0, \pi/2\}; q_2 = \{0, \pi/2\}; q_3 = \{0, \pi/2\};$
(C)	$q_1 = \{c\}; q_2 = \{c\}; q_3 = \{c\};$
(D)	$q_1 = \{0\}; q_2 = \{0\}; q_3 = \{0\};$

TABLE 3: Adopted parameters value for the PTFE-simplified hinge model.

Parameters	Value
E (Young modulus)	$500 \cdot 10^3$ [MPa]
σ_{Yield}	50 [MPa]
h	0.2 [mm]
L	3 [mm]

or their functional relevance could increase, as the (A) and (C) demonstrate, respectively.

All the other positions, physically reachable by the platform centre, contribute to define the robot workspace (WS), qualitatively shown in Figure 6 [10].

In particular, the planar view, more than the others, allows to appreciate how the WS represents the intersection of the three spheres, each of them centered in one of the foot.

This ideal WS should actually be reduced, because of the flexure hinges adopted as joints. For instance, under the hypothesis of the simplified hinge model shown in Figure 7, and the use of homogeneous PTFE material (Table 3 for the characteristics), the maximum deflection angle can be easily evaluated as expressed by the relation (13); if considering the maximum radius of curvature that the beam can bear before yielding, under a pure bending moment, it can be determined through the relation (14):

$$\Theta_{\text{Yield}} = \frac{L}{\rho_{\text{Yield}}}, \quad (13)$$

$$\frac{1}{\rho_{\text{Yield}}} = \frac{2 \cdot \sigma_{\text{Yield}}}{h \cdot E}. \quad (14)$$

Once defined the generic deflection angle Θ_n ($n = 1, \dots, N$, with N the total hinges number) that the n th hinge assumes at the generic instant t and forcing simultaneously all the hinges to verify the reachability condition (15), the reduced WS qualitatively can be identified as shown in Figure 8:

$$\Theta_n \leq \Theta_{\text{Yield}}. \quad (15)$$

4. Dynamic Analysis

Further elements need to be introduced to analyze the robot dynamic behavior: a column vector F_s of all the generalized forces (forces and torques) applied to the platform centre, the column vector F_q of the generalized forces applied to the actuated joints, and the diagonal mass matrix \mathcal{M} containing the mass property of all the ‘‘interesting’’ points, that is, the generalized forces act along those coordinates (joints and platform centre for this treatment) [11].

For this reason, the S and Q vectors need to be rewritten as S_d and Q_d , accordingly to the identification of the new interesting coordinates, and also J will change consequently its form.

The further step requires to distinguish, into the definition of F_s , between externally imposed forces and inertial ones, as the relations (16) and (17) present:

$$F_s = F_{se} + F_{si}, \quad (16)$$

$$F_{si} = -\mathcal{M}\ddot{S}_d. \quad (17)$$

All these elements are combined into the expression (18), representing the dynamic problem in the classical formulation [12], with $\overline{\mathcal{M}}$, \mathcal{V} , and \mathcal{G} defined as the relations (19), (20), and (21) describe:

$$\overline{\mathcal{M}}(Q_d)\ddot{Q}_d + \mathcal{V}(Q_d, \dot{Q}_d) + \mathcal{G}(Q_d, F) = 0, \quad (18)$$

$$\overline{\mathcal{M}}(Q_d) = J^T \mathcal{M} J, \quad (19)$$

$$\mathcal{V}(Q_d, \dot{Q}_d) = (J^T \mathcal{M} \dot{J}) \dot{Q}_d, \quad (20)$$

$$\mathcal{G}(Q_d, F) = -(J^T F_{se} + F_q). \quad (21)$$

Also the contribute of the material flexibility should be considered for a correct evaluation of the external forces acting on the structure: thus, two different lumped elasticity models have been evaluated, under the hypothesis of idealized flexure hinges, in which all the elastic phenomena can be concentrated [13].

With reference to Figures 9 and 10, an approximated value of compliance can be determined for these two models, by considering the expressions (22) and (23); once determined, at every iteration, the angular incremental displacement $\Delta\Theta$ introduced in every hinge, the elasticity force $F_{\text{elasticity}}$ can be estimated step by step as the relation (24) presents [14]:

$$C_{\text{type1}} = \frac{9\pi\sqrt{R}}{2Es\sqrt{h^5}}, \quad (22)$$

$$C_{\text{type2}} = \frac{9\pi\sqrt{R}}{\sqrt{2}Es\sqrt{h^5}}, \quad (23)$$

$$F_{\text{elasticity}} = C \cdot \Delta\Theta. \quad (24)$$

This contribute can be added, as a further external force, to the F_{se} vector previously defined for the totally rigid body model, as presented by the expression (25), where F_{se}^* represents the complete external force vector implemented into the dynamic analysis:

$$F_{se}^* = F_{se} + F_{\text{elasticity}}. \quad (25)$$

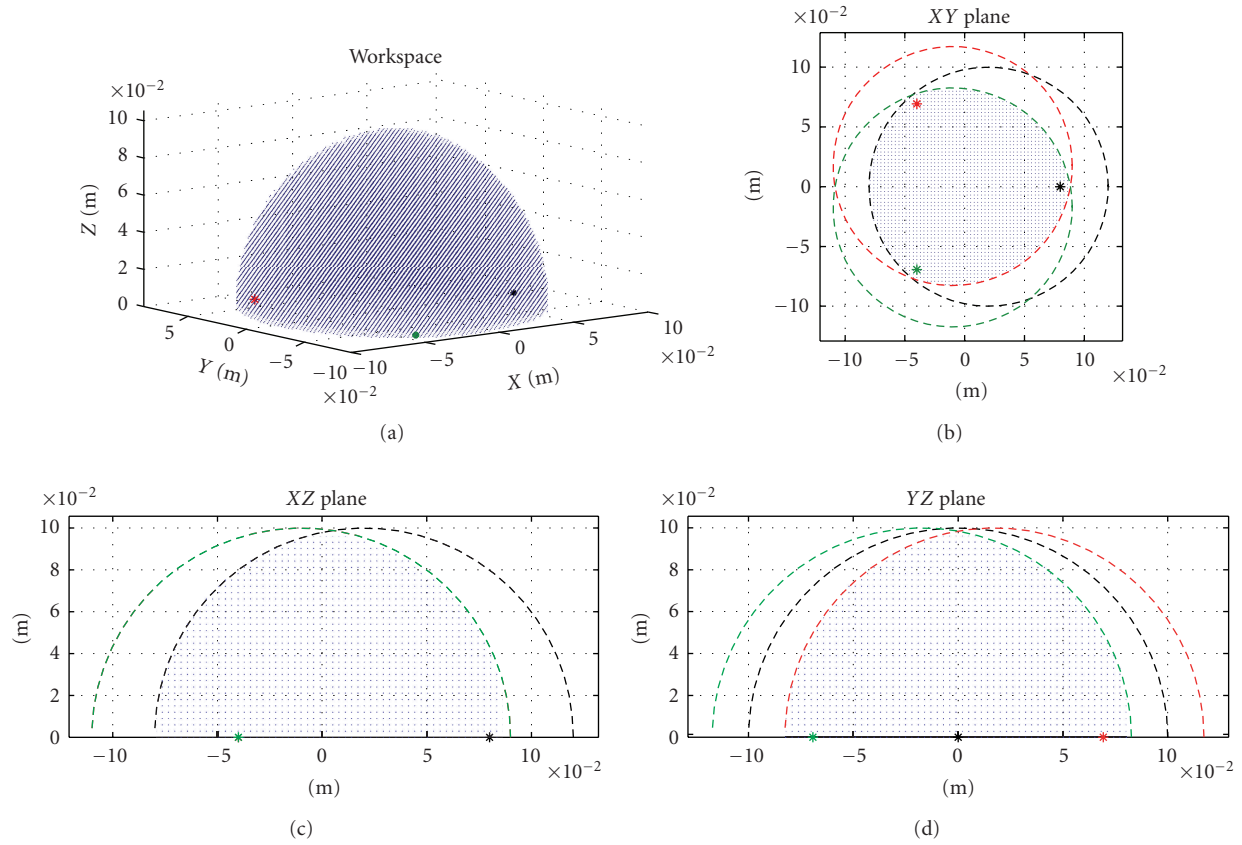


FIGURE 6: The robot workspace: black: the feet of the first leg; red the feet of the second and green of the third one.

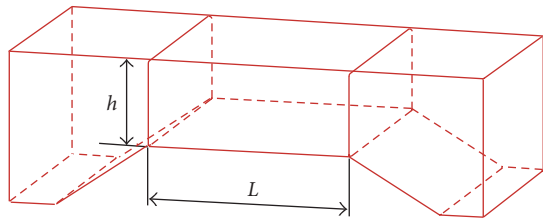


FIGURE 7: Simplified hinge model.

5. Simulations Results

Once analyzed the manipulator kinematics and dynamics, the identified algorithms have been implemented through MATLAB R2008a and Maple 9.5, respectively.

For the F_{se} vector, three different profiles have been considered, as Table 4 synthesizes, even if the random profile has not been considered for the comparison of the simulation results, because of the not repeatability of the initial conditions.

Table 5 presents the implemented motion profiles shown in Figures 11, 12, and 13 [15].

Imposing the point-to-point trajectories that Table 6 describes, the data presented in Table 7 generate the torques profiles shown in Figures 14–16.

TABLE 4: External forces profiles: i, j , and k denote the versors of the X, Y, and Z axes in the absolute reference system.

Type	F_{se}^* profile [N]
Constant	$-100 \cdot \vec{i}$
Random	$(0 \div 100) \cdot \vec{i}$
Function of the time	$3t \cdot \vec{i} + 2(t - 3) \cdot \vec{j} + 6t \cdot \vec{k}$

TABLE 5: Implemented motion profiles.

Type	Motion profile
(a)	Constant accelerated symmetric profile
(b)	Trapezoidal symmetric profile, with linear connectors
(c)	Trapezoidal symmetric profile, with linear connectors and random noise (changing at every instant without overtaking the 2% of the maximum acceleration value)

Figure 14 describes how the torques change by applying constant external forces but different motion profiles: the presence of random noise, in the right diagram, does not

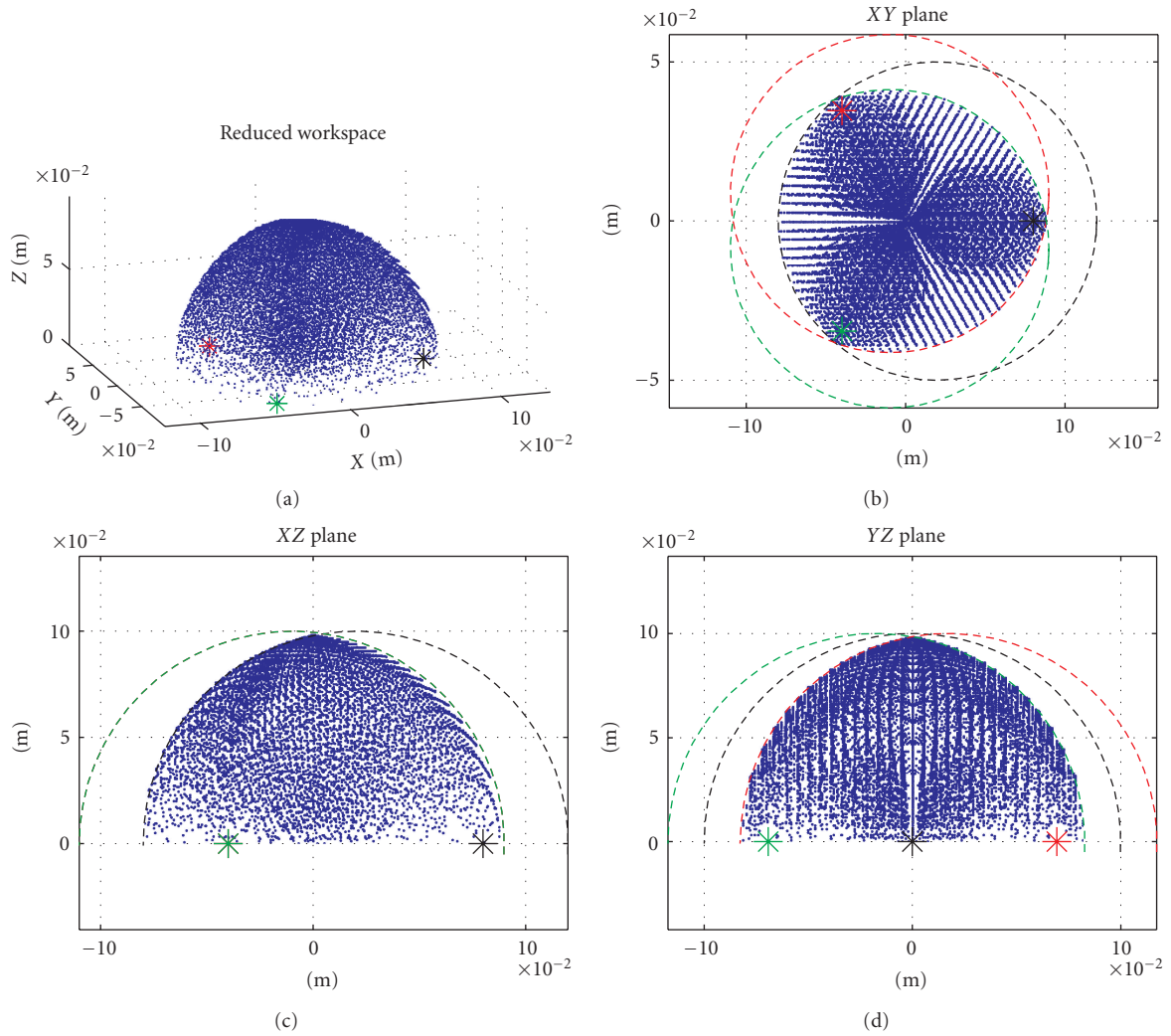


FIGURE 8: The robot reduced workspace [m]: black: the feet of the first leg; red the feet of the second and green of the third one.

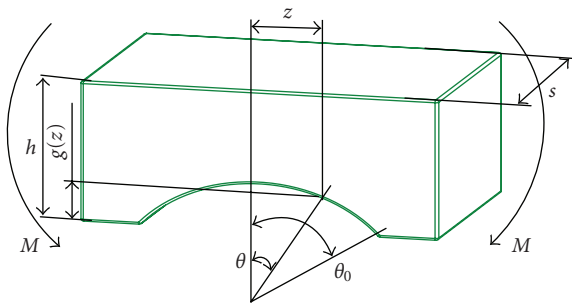


FIGURE 9: Type 1 flexure hinge model.

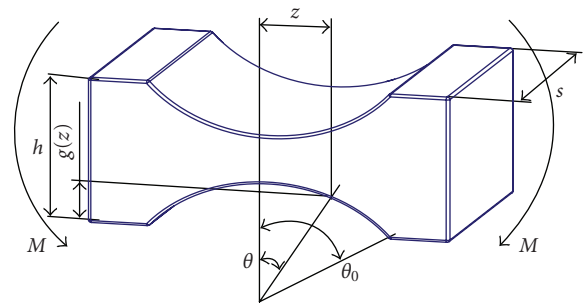


FIGURE 10: Type 2 flexure hinge model.

TABLE 6: Imposed point-to-point trajectory.

Parameters	Value
Starting point	[0.02 0.01 0.06 1]' [m]
Ending point	[-0.02 -0.01 0.06 1]' [m]
Motion time	1 [s]

introduce rough behavior unlike the (a) profile of the left graph.

The hinges compliance is analyzed in Figure 15: on the left, the simulations results obtained implementing the type 1 model present higher torques values required to the actuators, confirming the stiffer behavior that this kind of

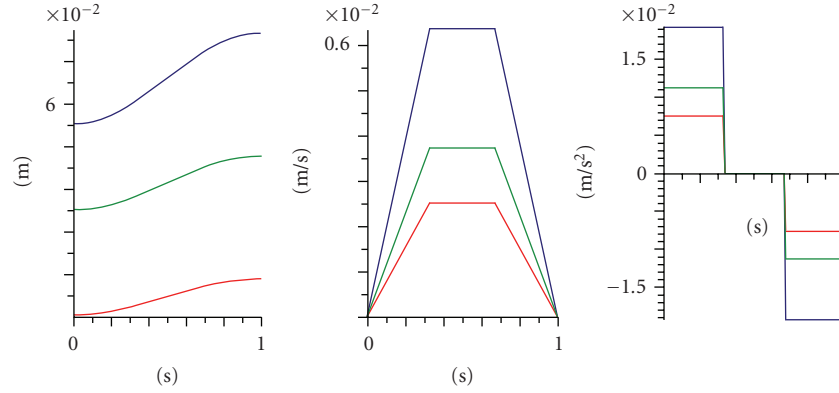


FIGURE 11: Constant acceleration motion profile. From the left, displacement, velocity, and acceleration; blue: the first leg; red: the second; green: the third one.

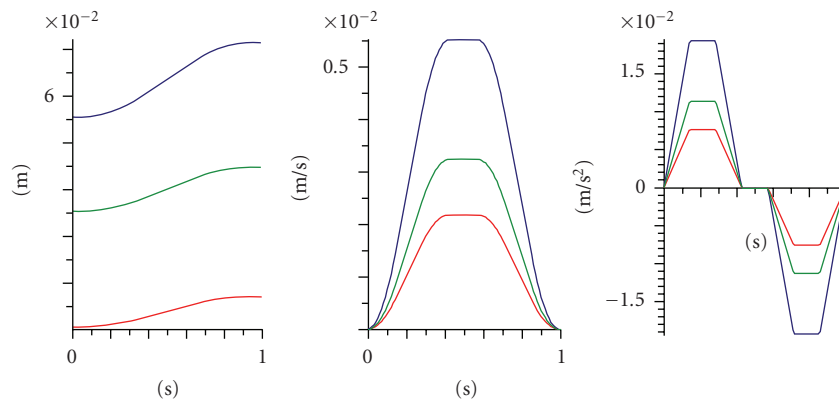


FIGURE 12: Trapezoidal symmetric profile, with linear connectors. From the left, displacement, velocity, and acceleration; blue: the first leg; red: the second; green: the third one.

hinge offers to the motion, under the same work conditions and geometrical parameters.

Figure 16 shows finally the torques profiles obtained imposing on the left a constant external force and depending on the time on right.

6. Conclusions

The kinematic and dynamic analyses of a compliant PKM mesomanipulator have been described in this paper.

The functional model of the robot has been presented in the brief introduction, and then forward and inverse analytical kinematics have been detailed. In the following paragraph the singularities and the manipulator workspace have been addressed, with particular attention to the physical reachability of the singularity conditions.

Once defined the kinematics, the dynamic problem has been delineated, under the hypothesis of lumped elasticity into the flexure hinges.

Finally, some simulations results have been presented, to compare how the actuators torque profile changes with the external imposed conditions: various motion profiles, different flexure hinges models, or a particular external force profile.

TABLE 7: Geometrical dimensions and mass properties of the system.

System properties	Value
b	0.05 [m]
Links width	0.004 [m]
Links thickness	0.002 [m]
c	0.03 [m]
a	0.02 [m]
d	0.04 [m]
Distance between foot and reference system	0.07 [m]
Young modulus	0.3 [GN/m ²]
Link mass	0.005 [kg]

To complete the mesomanipulator analysis, an optimization of the robot scale and dimensions could be performed; the simulations results underline also the significant influence of the flexure hinges on the manipulator performance, so that particular attention should be paid to the material properties of such elements and their design. Once implemented these considerations, the manipulator analysis could be improved by considering also vibrations to evaluate the realism of the results until now obtained.

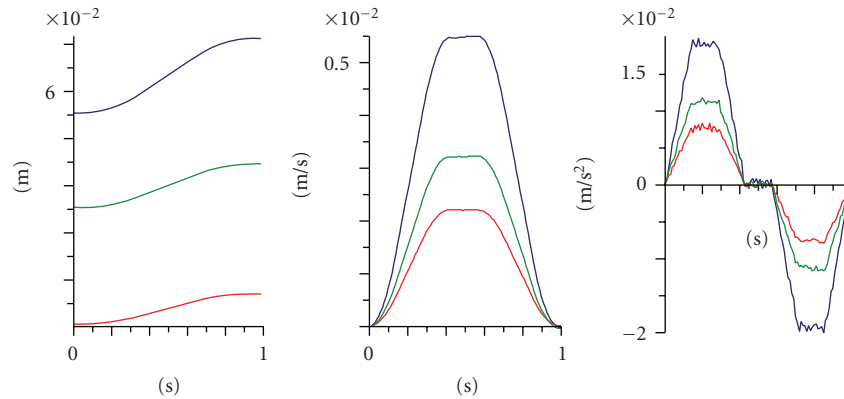


FIGURE 13: Trapezoidal symmetric profile, with linear connectors and random noise (changing at every instant without overtaking the 2% of the maximum acceleration value). From the left, displacement, velocity, and acceleration; blue: the first leg; red: the second; green: the third one.

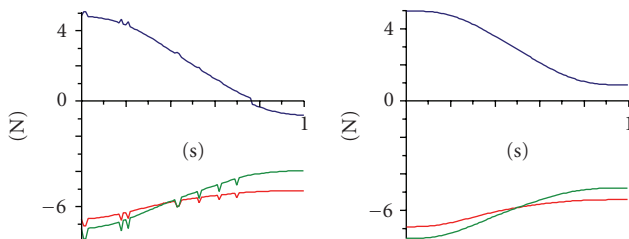


FIGURE 14: Torques values to the actuators with the (a) profile on the left and the (c) profile on the right; blue: the first leg; red: the second; green: the third one.

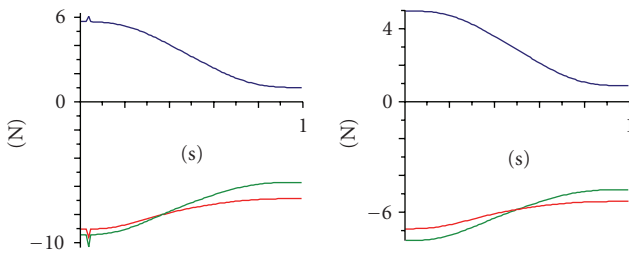


FIGURE 15: Torques values to the actuators. From the left, type 1 and type 2 flexure hinge model; blue: the first leg; red: the second; green: the third one.

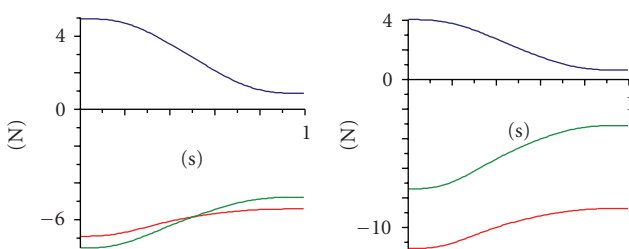


FIGURE 16: Torques values to the actuators, with constant external forces on the left and function of the time on the right; blue: the first leg; red: the second; green: the third one.

Acknowledgments

The authors are grateful to Diego De Santis for the interesting discussion and the contribution on the flexure hinges behavior and to the anonymous reviewers for their kind suggestions.

References

- [1] B. S. El-Khasawneh and P. M. Ferreira, "Computation of stiffness and stiffness bounds for parallel link manipulators," *International Journal of Machine Tools & Manufacture*, vol. 39, no. 2, pp. 321–342, 1999.
- [2] L. L. Howell, *Compliant Mechanisms*, John Wiley & Sons, New York, NY, USA, 2001.
- [3] J. J. Craig, *Robotics. Mechanics and Control*, Addison Wesley, Reading, Mass, USA, 1986.
- [4] M. Hebesacker, T. Treib, O. Zirn, and M. Honegger, "Hexaglide 6 dof and triaglide 3 dof parallel manipulators," in *Parallel Kinematic Machines: Theoretical Aspects and Industrial Requirements*, pp. 345–355, Springer, Berlin, Germany, 1999.
- [5] C. Amici, A. Borboni, P. L. Magnani, and D. Pomi, "Kinematic analysis of a compliant, parallel and three-dimensional meso-manipulator generated from a planar structure," in *Proceedings of the 2nd European Conference on Mechanism Science (EUCOMES '08)*, pp. 479–485, Cassino, Italy, November 2008.
- [6] A. G. Erdman and G. N. Sandor, *Mechanism Design: Analysis and Synthesis*, Prentice Hall, Englewood Cliffs, NJ, USA, 1991.
- [7] G. Legnani and R. Riva, "Kinematics of modular robots," in *Proceedings of the 7th World Congress on Theory of Machines and Mechanisms (IFTOMM '87)*, Seville, Spain, 1987.
- [8] X. Kong and C. M. Gosselin, "Type synthesis of 3-DOF PPR-equivalent parallel manipulators based on screw theory and the concept of virtual chain," *Journal of Mechanical Design*, vol. 127, no. 6, pp. 1113–1121, 2005.
- [9] R. Featherstone, "Position and velocity transformations between robot end-effector coordinates and joint angles," *International Journal of Robotics Research*, vol. 2, no. 2, pp. 35–45, 1983.
- [10] J.-S. Zhao, M. Chen, K. Zhou, J.-X. Dong, and Z.-J. Feng, "Workspace of parallel manipulators with symmetric identical kinematic chains," *Mechanism and Machine Theory*, vol. 41, no. 6, pp. 632–645, 2006.

- [11] F. Xi, O. Angelico, and R. Sinatra, "Tripod dynamics and its inertia effect," *Journal of Mechanical Design*, vol. 127, no. 1, pp. 144–149, 2005.
- [12] J. Gallardo, J. M. Rico, A. Frisoli, D. Checcacci, and M. Bergamasco, "Dynamics of parallel manipulators by means of screw theory," *Mechanism and Machine Theory*, vol. 38, no. 11, pp. 1113–1131, 2003.
- [13] S.-C. Wang, H. Hikita, H. Kubo, Y.-S. Zhao, Z. Huang, and T. Ifukube, "Kinematics and dynamics of a 6 degree-of-freedom fully parallel manipulator with elastic joints," *Mechanism and Machine Theory*, vol. 38, no. 5, pp. 439–461, 2003.
- [14] L. Dassa, *Mechanisms based on flexure articulations*, Ph.D. thesis, University of Brescia, Brescia, Italy, March 2009.
- [15] M. Antonini, A. Borboni, R. Bussola, and R. Faglia, "A genetic algorithm as support in the movement optimisation of a redundant serial robot," in *Proceedings of the 8th Biennial ASME Conference on Engineering Systems Design and Analysis (ESDA '06)*, Torino, Italy, July 2006.

Research Article

Application of the Rotation Matrix Natural Invariants to Impedance Control of Rotational Parallel Robots

L. Bruzzone¹ and M. Callegari²

¹Dipartimento di Meccanica e Costruzione delle Macchine, Università di Genova, Via Opera Pia 15A, 16145 Genova, Italy

²Dipartimento di Meccanica, Università Politecnica delle Marche, Via Brecce Bianche 12, 60131 Ancona, Italy

Correspondence should be addressed to L. Bruzzone, bruzzone@dimcc.unige.it

Received 17 June 2009; Accepted 10 November 2009

Academic Editor: Zhen Huang

Copyright © 2010 L. Bruzzone and M. Callegari. This is an open access article distributed under the Creative Commons Attribution License, which permits unrestricted use, distribution, and reproduction in any medium, provided the original work is properly cited.

Force control of parallel robots with rotational degrees of freedom through impedance algorithms is considerably influenced by the representation method of the end-effector orientation. Using the natural invariants of the rotation matrix and the angular velocity vector in the impedance control law has some theoretical advantages, which derive from the Euclidean-geometric meaning of these entities. These benefits are particularly evident in case of robotic architectures with three rotational degrees of freedom (serial or parallel wrists with spherical motion). The behaviour of a 3-CPU parallel robot controlled by an impedance algorithm based on this concepts is assessed through multibody simulations, and the results confirm the effectiveness of the proposed approach.

1. Introduction

Several robotic applications involve the control of the interaction forces between end-effector and external environment; the control laws that can fulfil this requirement can be divided into two families: hybrid position/force control algorithms and impedance control algorithms. These two approaches have been widely discussed and compared in the scientific literature during the last decades, in particular with reference to serial kinematics [1–7].

In the last years the industrial interest about parallel robots (parallel kinematics machines, PKMs) is growing; mass-produced parallel manipulators are widely used especially in two categories of applications:

- (i) fast speed pick-and-place tasks with small payloads; in this case high-speed, lightweight parallel robots are adopted for their excellent dynamic performances, due to the low moving masses (e.g., the FlexPicker IRB340 by ABB based on the Delta kinematics [8]);
- (ii) machining or assembly tasks characterized by high forces, which requires high structural stiffness and

positioning accuracy; in this case high-stiffness PKMs (e.g., the F-200iB by Fanuc based on the Gough-Stewart kinematics [9, 10] or the Tricept by Neos Robotics AB) [11]) offer a high ratio between maximum payload/force and robot mass.

In most cases, parallel robots are position-controlled; nevertheless, the scientific and industrial interest about force-controlled PKMs is growing, even if only a few works on the subject are presently available, probably due to the fact that PKMs are relatively new architectures, characterised by quite complex kinematic and dynamic models [12–14]. In particular, the use of impedance-controlled parallel robots [15–18] is an effective solution: the moving masses of PKMs are limited, because the actuators are usually fixed to the ground, and then it is possible to realise the desired stiffness-damping behaviour neglecting the compensations of the inertial terms.

One of the major problems in the synthesis of a suitable impedance control law (both for serial and parallel robots) is the definition of the rotational stiffness, which is strictly related to the representation method for the end-effector

orientation [19]. While the position of a point in space can be easily defined by a three-dimensional vector, there are many mathematical tools to represent the orientation of a rigid body in space [20, 21] and this influences the resulting impedance control law. In the following of the paper this aspect will be discussed with reference to simulation results involving an impedance-controlled 3-CPU parallel robotic wrist.

2. Representation of the End-Effector Orientation

Probably, the most common method to describe the orientation of a rigid body is the use of the Euler angles; nevertheless, this method has many drawbacks [22, 23]:

- (i) there are 12 different sets of Euler angles, and the choice of a set influences arbitrarily the control algorithm;
- (ii) there are representation singularities (configurations defined by nonunique values of Euler angles), and in these singularity loci it is impossible to describe an arbitrary angular velocity as function of the Euler angles time derivatives.

Some researchers tried to overcome these limitations by using a modified set of Euler angles that avoid singularities [24] or the so-called Euler parameters, a 4-dimensional vector of invariants that are not geometric entities [25].

Another possible representation of the orientation is the 3×3 rotation matrix, but its nine elements are not independent and an impedance algorithm based on three independent rotation matrix elements is poor of geometrical meaning.

An arbitrary rigid body rotation is uniquely defined by the *axis of rotation* (represented by the unit vector \mathbf{e}) and the *angle of rotation* θ , which is the amount of rotation according to the right-hand rule; the unit vector \mathbf{e} and the angle θ are the *natural invariants* of the rotation matrix, independent from the reference frame [20].

In [26] the use of the frame-invariant vector $\mathbf{E} = \theta \mathbf{e}$ in the impedance control law is proposed. The main advantage of the use of this vector is related to its geometrical meaning and strict relation to the angular velocity vector $\boldsymbol{\omega}$:

$$\boldsymbol{\omega} = \sin \theta \dot{\mathbf{e}} + (1 - \cos \theta) \mathbf{e} \times \dot{\mathbf{e}} + \dot{\theta} \mathbf{e}. \quad (1)$$

In an impedance algorithm the vector \mathbf{E} can be used to represent the rotation between the actual end-effector orientation and the reference orientation; in this case the maximum values of θ are limited. It is easy to demonstrate that if θ tends to zero, the angular velocity vector tends to the time derivative of \mathbf{E} :

$$\lim_{\theta \rightarrow 0} \boldsymbol{\omega} = \dot{\theta} \mathbf{e} + \dot{\theta} \mathbf{e} = \frac{d}{dt} \mathbf{E}. \quad (2)$$

This is a very important propriety of the vector \mathbf{E} , because an impedance control law based on the vector \mathbf{E} for the stiffness term and on the angular velocity vector $\boldsymbol{\omega}$ for the

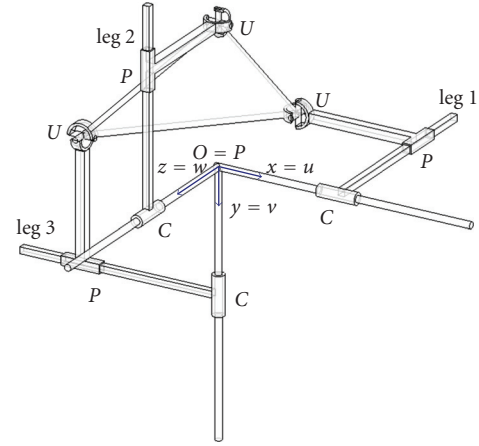


FIGURE 1: The 3-CPU parallel architecture.

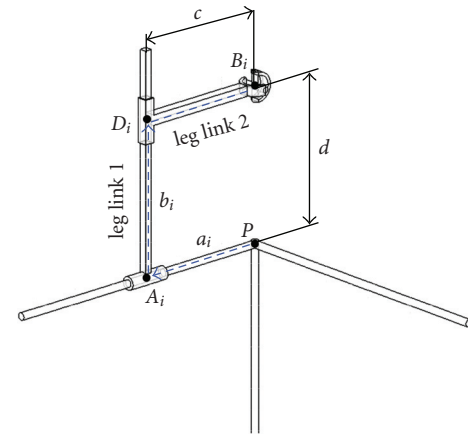


FIGURE 2: Leg of the CPU parallel architecture.

damping term uses two vectors that are nearly in relation of time derivative. This important propriety is not shared by the other orientation representation methods, and it leads to a more natural and intuitive robot behaviour. The advantages of such an approach in case of a six-degree-of-freedom parallel robot are shown in [26]; in case of a purely rotational three-degree-of-freedom parallel robot the benefits are even more evident, and this will be shown in the following of the paper.

3. The 3-CPU Parallel Architecture

In the 3-CPU architecture [27] (Figure 1) three identical serial chains (legs) connect the fixed base and the rotating end-effector platform; each leg (Figure 2) is composed of two links; the first link is connected to the base by a cylindrical joint and to the second link by a prismatic joint; the second link is connected to the end-effector by a universal joint.

The axes of the cylindrical joints $\vec{\mathbf{a}}_i$, $i = 1, 2, 3$, intersect at the *centre of motion* O and are aligned to the x, y, z axes of the fixed reference frame, with its centre in O . The first link of i th leg is perpendicular to the axis $\vec{\mathbf{a}}_i$ and has a variable length b_i

thanks to the prismatic joint D_i ; the second link is parallel to \vec{a}_i . The first axis of the universal joint B_i is perpendicular to the plane of the i th leg, while the second axis intersects the corresponding axes of the other legs at the point P ; these three axes are coincident to the v, w, u axes of a cartesian frame located in P and attached to the end-effector. If proper *manufacturing* and *mounting conditions* are fulfilled, the centres of the fixed frame $O(x, y, z)$ and rotating frame $P(u, v, w)$ remain coincident during the motion, and the end-effector performs a spherical motion. In particular, in the initial configuration the three linear displacements a_i of the cylindrical joints are equal to c and the linear displacements b_i of the prismatic joints are equal to d (Figure 2). The spherical motion of the end-effector can be driven by actuating the linear displacements of the cylindrical joints; therefore, the vector of the internal coordinates is:

$$\mathbf{q} = \begin{bmatrix} a_1 \\ a_2 \\ a_3 \end{bmatrix}. \quad (3)$$

The direct and inverse kinematics of the robot make the forward and backward connections between the internal coordinates and the relative rotation of the frame $P(u, v, w)$ with respect to $O(x, y, z)$.

The choice of the three external coordinates influences the impedance control law; in the following, two possible sets of external coordinates are considered:

- (i) the set of Euler angles α, β, γ corresponding to three subsequent rotations along the axes u, v, w that represent the overall relative rotation between $O(x, y, z)$ and $P(u, v, w)$;
- (ii) the three components of the vector ${}^O_P\mathbf{E}$ that represent the overall relative rotation between $O(x, y, z)$ and $P(u, v, w)$.

Independently of the selected set of external coordinates, the direct kinematic problem admits up to 8 solutions, while the solution of the inverse kinematics is single [27]. The choice of the external coordinates determines the consequent Jacobian matrix: deriving the two possible sets of inverse kinematics equations, two alternative analytical Jacobian matrices can be found:

- (i) the analytical Jacobian matrix \mathbf{J}_A , which relates the time derivative of \mathbf{q} and the time derivatives of the Euler angles, collected in the vector $\boldsymbol{\alpha}_P$:

$$\frac{d}{dt}\mathbf{q} = \mathbf{J}_A \begin{bmatrix} \dot{\alpha} \\ \dot{\beta} \\ \dot{\gamma} \end{bmatrix} = \mathbf{J}_A \frac{d}{dt}\boldsymbol{\alpha}_P. \quad (4)$$

- (ii) the analytical Jacobian matrix \mathbf{J}_E , which relates the time derivative of \mathbf{q} and the time derivative of \mathbf{E} :

$$\frac{d}{dt}\mathbf{q} = \mathbf{J}_E \frac{d}{dt}{}^O_P\mathbf{E}. \quad (5)$$

The geometric Jacobian \mathbf{J}_G represents the relationship between the time derivative of \mathbf{q} and the end-effector angular velocity vector $\boldsymbol{\omega}_P$:

$$\frac{d}{dt}\mathbf{q} = \mathbf{J}_G\boldsymbol{\omega}_P. \quad (6)$$

It is easy to demonstrate, by using (2), (5), and (6), that if θ tend to zero, the Jacobian matrices \mathbf{J}_G and \mathbf{J}_E tends to be equal:

$$\lim_{\theta \rightarrow 0}\mathbf{J}_G = \lim_{\theta \rightarrow 0}\mathbf{J}_E. \quad (7)$$

4. Impedance Control Algorithm

The basic concept of impedance control is that the robot end-effector, subject to external forces, follows a trajectory with a predetermined spatial compliance [28, 29]; this compliance, which influences the end-effector dynamic behaviour, is defined by the *stiffness matrix* \mathbf{K} and the *damping matrix* \mathbf{C} ; the reference configuration of the end-effector is a *virtual equilibrium state* because it corresponds to an actual equilibrium only if no force is exerted by the environment.

The actual position of the end-effector can be represented alternatively by the external coordinates vectors $\boldsymbol{\alpha}_P$ or ${}^O_P\mathbf{E}$; similarly, the virtual equilibrium configuration, corresponding to the reference frame D , can be represented by the Euler angles $\boldsymbol{\alpha}_D$ or by the vector ${}^O_D\mathbf{E}$. Using the principle of the virtual work and considering (4), (5), and (7), the two impedance control laws (8) and (10) can be derived, the first based on the Euler angles and the analytical Jacobian matrix \mathbf{J}_A , and the second based on the vector \mathbf{E} and the geometric Jacobian matrix \mathbf{J}_G :

$$\mathbf{F} = \left(\mathbf{J}_A^T\right)^{-1} \left[\mathbf{K}_r(\boldsymbol{\alpha}_D - \boldsymbol{\alpha}_P) + \mathbf{C}_r(\dot{\boldsymbol{\alpha}}_D - \dot{\boldsymbol{\alpha}}_P)\right], \quad (8)$$

where [27]

$$\mathbf{J}_A = d \begin{bmatrix} 0 & -s\beta s\gamma & c\beta c\gamma \\ c\alpha c\beta & -s\alpha s\beta & 0 \\ -s\alpha s\beta c\gamma - c\alpha s\gamma & c\alpha c\beta c\gamma & -c\alpha s\beta s\gamma - s\alpha c\gamma \end{bmatrix}, \quad (9)$$

$$\mathbf{F} = \left(\mathbf{J}_G^T\right)^{-1} \left[\mathbf{K}_r\left({}^O_D\mathbf{E} - {}^O_P\mathbf{E}\right) + \mathbf{C}_r(\boldsymbol{\omega}_D - \boldsymbol{\omega}_P)\right], \quad (10)$$

where [27]:

$$\mathbf{J}_G = d \begin{bmatrix} 0 & -c\alpha s\beta s\gamma - s\alpha c\gamma & c\alpha c\gamma - s\alpha s\beta s\gamma \\ c\alpha c\beta & 0 & -s\beta \\ -s\alpha s\beta c\gamma - c\alpha c\beta s\gamma & c\beta c\gamma & 0 \end{bmatrix} \quad (11)$$

In the control laws (8) and (10) one has the following:

- (i) \mathbf{F} is the vector of the three actuation forces, acting along the axes of the cylindrical joints;
- (ii) \mathbf{K}_r is the *rotational stiffness matrix*, which expresses the relation between rotation and elastic torque in the desired impedance control behaviour;

TABLE 1: Geometric and inertial properties of the considered 3-CPU mechanism.

Geometric parameters	
c	93.5 mm
d	106.07 mm
Main inertial parameters	
End-effector mass	$3.893 \cdot 10^{-1}$ kg
End effector inertia matrix with respect to the coordinate frame $P(u, v, w)$	$\begin{bmatrix} 1.426 & -0.356 & -0.356 \\ -0.356 & 1.426 & -0.356 \\ -0.356 & -0.356 & 1.426 \end{bmatrix} \cdot 10^{-3}$ kgm ²
Mass of the leg link 1	$3.944 \cdot 10^{-2}$ kg
Moment of inertia of the leg link 1 about its cylindrical joint axis	$2.364 \cdot 10^{-4}$ kgm ²
Mass of the leg link 2	$3.928 \cdot 10^{-2}$ kg
Moment of inertia of the leg link 2 about its principal axis parallel to the cylindrical joint axis of the same leg	$8.447 \cdot 10^{-7}$ kgm ²
Mass of the universal joint cross	$3.59 \cdot 10^{-3}$ kg

(iii) \mathbf{C}_r is the *rotational damping matrix*, which expresses the relation between rate of rotation and viscous torque in the desired impedance control behaviour.

Let us note that in the control law (10) the damping term is not based on the derivatives of the external coordinates but on the angular velocity vector. The matrices \mathbf{K}_r and \mathbf{C}_r are in general nondiagonal; it is possible to define \mathbf{K}_r and \mathbf{C}_r using a principal reference frame (PR) in which they are diagonal; this principal reference frame can be selected on the basis of the task requirements; it is possible to obtain \mathbf{K}_r and \mathbf{C}_r in the world frame (O) by means of the rotation matrix ${}^O\mathbf{R}^{PR}$ [26]:

$$\begin{aligned} \mathbf{K}_r &= \left({}^O\mathbf{R}^{PR} \right)^T {}^{PR}\mathbf{K}_r {}^O\mathbf{R} = {}^O\mathbf{R}^{PR} {}^{PR}\mathbf{K}_r \left({}^O\mathbf{R}^{PR} \right)^T, \\ \mathbf{C}_r &= \left({}^O\mathbf{R}^{PR} \right)^T {}^{PR}\mathbf{C}_r {}^O\mathbf{R} = {}^O\mathbf{R}^{PR} {}^{PR}\mathbf{C}_r \left({}^O\mathbf{R}^{PR} \right)^T, \end{aligned} \quad (12)$$

where ${}^{PR}\mathbf{K}_r$ and ${}^{PR}\mathbf{C}_r$ are the stiffness and damping matrices expressed in the principal reference frame.

In the following section, the control laws (8) and (10) will be compared by means of multibody simulation, to show the advantages of the second control law, due to the geometric properties of the vector \mathbf{E} .

5. Simulation Results

The impedance control laws (8) and (10) have been applied to a 3-CPU parallel robot with the geometric and inertial parameters shown in Table 1. Since the two links of each leg rotate only about the corresponding cylindrical joint axis, only the moments of inertia with respect to this direction are reported; the universal joints crosses can be considered lumped masses concentrated in the corresponding universal joint centres.

Case Study A. In the case study A, starting from the initial condition with the coordinate frames P and O coincident, a moment ${}^O\mathbf{M}$ with direction $[-1, 1, 0.5]^T$ and magnitude 20 Nmm is applied to the end-effector. The control system

imposes an isotropic rotational behaviour, defined by the following diagonal stiffness and damping matrices:

$$\begin{aligned} {}^{PR}\mathbf{K}_r &= \mathbf{K}_r = \begin{bmatrix} 100 & 0 & 0 \\ 0 & 100 & 0 \\ 0 & 0 & 100 \end{bmatrix} \text{ Nmm/rad}, \\ {}^{PR}\mathbf{C}_r &= \mathbf{C}_r = \begin{bmatrix} 16.88 & 0 & 0 \\ 0 & 16.88 & 0 \\ 0 & 0 & 16.88 \end{bmatrix} \text{ Nmms/rad}. \end{aligned} \quad (13)$$

The value of the desired isotropic stiffness ($k = 100$ Nmm/rad) is arbitrary; the value of the isotropic damping coefficient is selected using an heuristic approach, considering each rotational direction as a linear inertia-torsional spring-torsional damper system with a damping coefficient $\xi = \sqrt{2}/2$. Therefore, the following well-known formula is used:

$$c = 2\xi\sqrt{kJ}, \quad (14)$$

where $J = 1.426 \cdot 10^{-3}$ kgm² = 1.426 Ns²mm is the end-effector moment of inertia (Table 1).

The rotational behaviour of the robot about the three directions can be compared with three decoupled second-order inertia-rotational spring-rotational damper systems, characterized by the following linear differential equations:

$$\begin{aligned} 3.10\ddot{\phi}_x + 16.88\dot{\phi}_x + 100\phi_x &= -13.33, \\ 3.10\ddot{\phi}_y + 16.88\dot{\phi}_y + 100\phi_y &= 13.33, \\ 3.10\ddot{\phi}_z + 16.88\dot{\phi}_z + 100\phi_z &= 6.67. \end{aligned} \quad (15)$$

For these three decoupled systems one has the following:

- (i) the inertia of $3.10 \cdot 10^{-3}$ kgm² = 3.10 Ns²mm derives from the end-effector moment of inertia increased considering approximately the leg links 1 and 2 as lumped masses placed, respectively, at a distance of $d/2$ and d from the point O ;

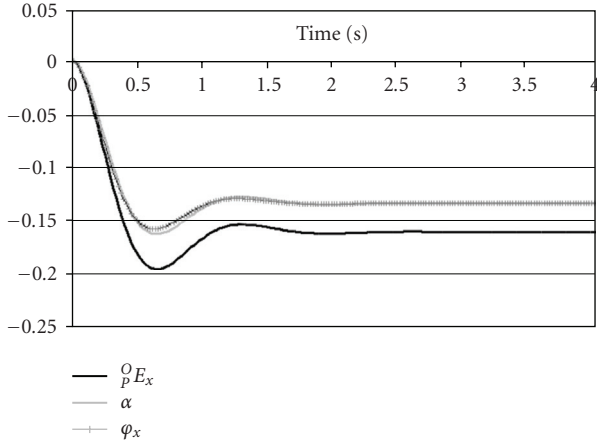


FIGURE 3: Comparison of ${}^0_P E_x$, α , and φ_x with the control law (8) in the case study A.

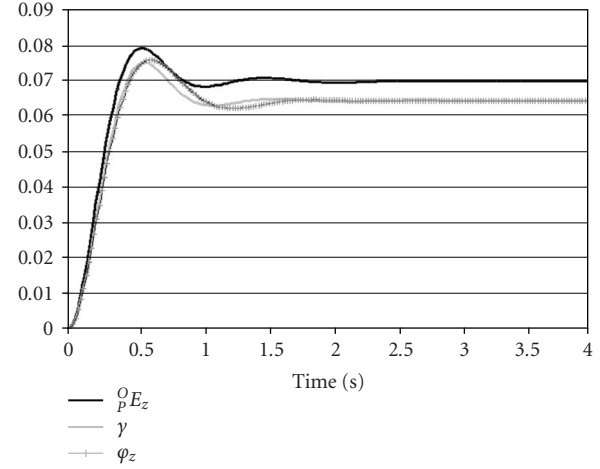


FIGURE 5: Comparison of ${}^0_P E_z$, γ , and φ_z with the control law (8) in the case study A.

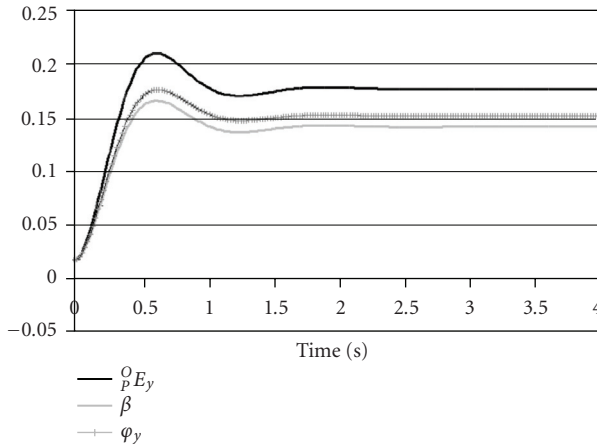


FIGURE 4: Comparison of ${}^0_P E_y$, β , and φ_y with the control law (8) in the case study A.

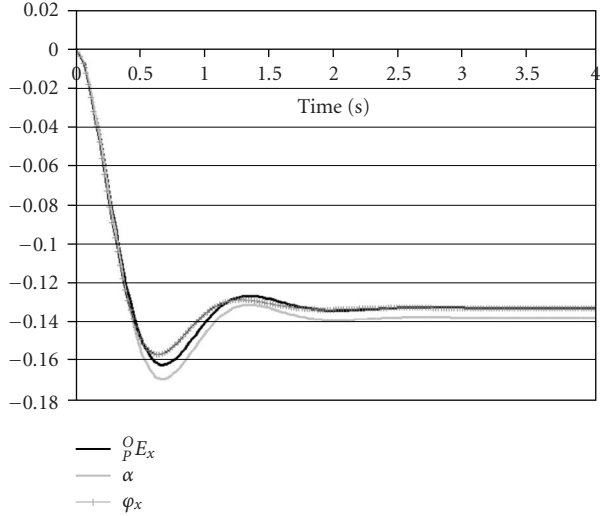


FIGURE 6: Comparison of ${}^0_P E_x$, α , and φ_x with the control law (10) in the case study A.

- (ii) the stiffness and damping coefficients are equal to the isotropic stiffness and damping coefficients k and c ;
- (iii) the applied moments are the three components of the moment ${}^0\mathbf{M}$.

Figures 3, 4 and 5 show the rotational behaviour of the robot controlled by the law (8), based on the analytical Jacobian matrix, in comparison with the three decoupled systems (15); in these graphs the end-effector orientation is represented both by the components of the vector ${}^0_P\mathbf{E}$ and by the Euler angles; Figures 6, 7 and 8 refer to the rotational behaviour of the robot controlled by the law (10), based on the geometric Jacobian matrix.

Both the control laws apply the isotropic stiffness and damping expressed by the matrices (13), but only the geometric control law (10) realizes an isotropic behaviour: in final steady state the end-effector rotation is ${}^0_P\mathbf{E} = [-0.1333, 0.1333, 0.0667]^T$ rad, that is a rotation with the same direction of the external moment ${}^0\mathbf{M}$ and magnitude equal to the magnitude of ${}^0\mathbf{M}$ divided by the isotropic

stiffness k . On the contrary, using the analytical control law (8) the final rotation is ${}^0_P\mathbf{E} = [-0.1601, 0.1582, 0.0724]^T$ rad.

Moreover, it is possible to note that using the geometric control law (10) the time histories of the three components of ${}^0_P\mathbf{E}$ are very similar to the ones of the three decoupled linear systems; this means that the rotational behaviour of the robot is very intuitive and almost decoupled in the three directions.

Case Study B. In the case study B, starting from the initial condition with the coordinate frames P and O coincident, a moment ${}^0\mathbf{M}$ with direction $[-1, 0, 1]^T$ and magnitude 20 Nmm is applied to the end-effector. Now the control system imposes a nonisotropic rotational behaviour; the stiffness and damping matrices are defined in a principal

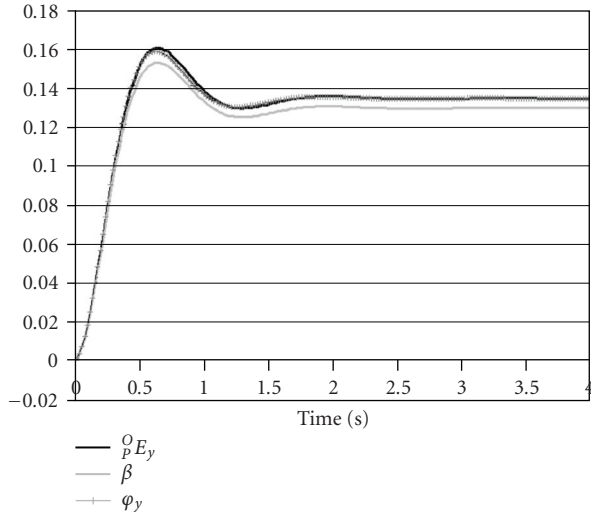


FIGURE 7: Comparison of ${}^O_p E_y$, β , and φ_y with the control law (10) in the case study A.

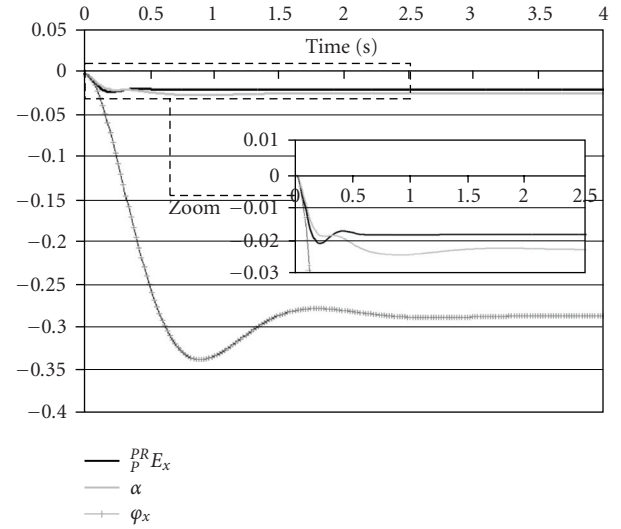


FIGURE 9: Comparison of ${}^{PR}_p E_x$, α , and φ_x with the control law (8) in the case study B.

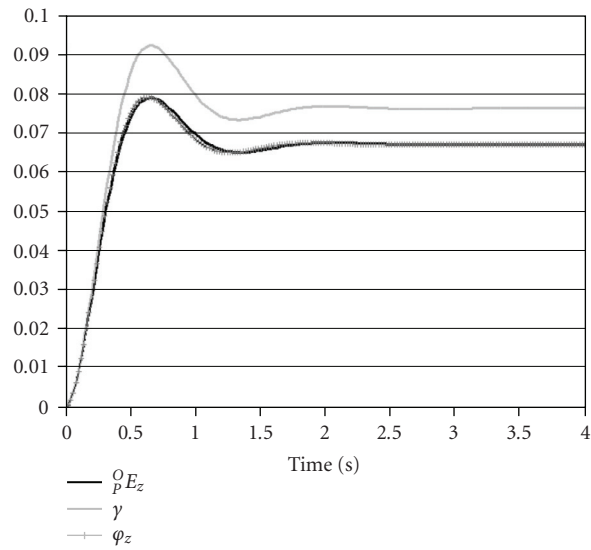


FIGURE 8: Comparison of ${}^O_p E_z$, γ , and φ_z with the control law (10) in the case study A.

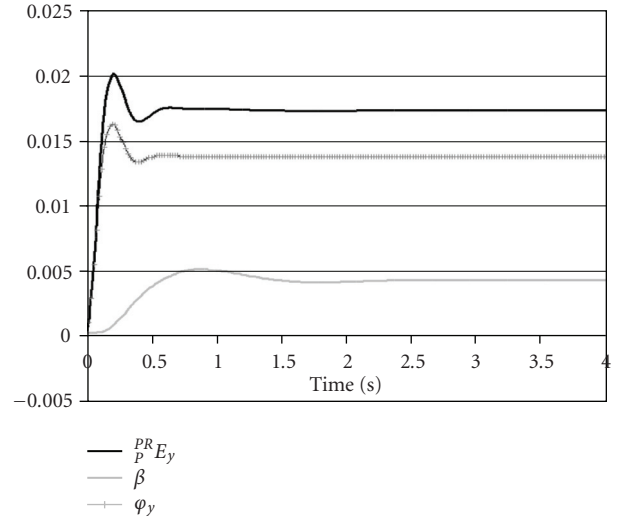


FIGURE 10: Comparison of ${}^O_p E_y$, β , and φ_y with the control law (8) in the case study B.

reference frame PR , which is rotated with respect to O according to the following vector \mathbf{E} :

$${}^{PR}_O \mathbf{E} = \left[\frac{1}{\sqrt{3}} \quad \frac{1}{\sqrt{3}} \quad \frac{1}{\sqrt{3}} \right]^T, \quad (16)$$

which corresponds to the rotation matrix:

$${}^O_{PR} \mathbf{R} = \begin{bmatrix} 0.6935 & -0.3326 & 0.6391 \\ 0.6391 & 0.6935 & -0.3326 \\ -0.3326 & 0.6391 & 0.6935 \end{bmatrix}. \quad (17)$$

The principal rotational stiffness and damping matrices are

$${}^{PR} \mathbf{K}_r = \begin{bmatrix} 50 & 0 & 0 \\ 0 & 1000 & 0 \\ 0 & 0 & 1000 \end{bmatrix} \text{ Nmm/rad}, \quad (18)$$

$${}^{PR} \mathbf{C}_r = \begin{bmatrix} 11.94 & 0 & 0 \\ 0 & 53.4 & 0 \\ 0 & 0 & 53.4 \end{bmatrix} \text{ Nmms/rad}.$$

The matrix ${}^{PR} \mathbf{K}_r$ imposes a rotational stiffness about the first principal axis much lower than about the other two axes, in

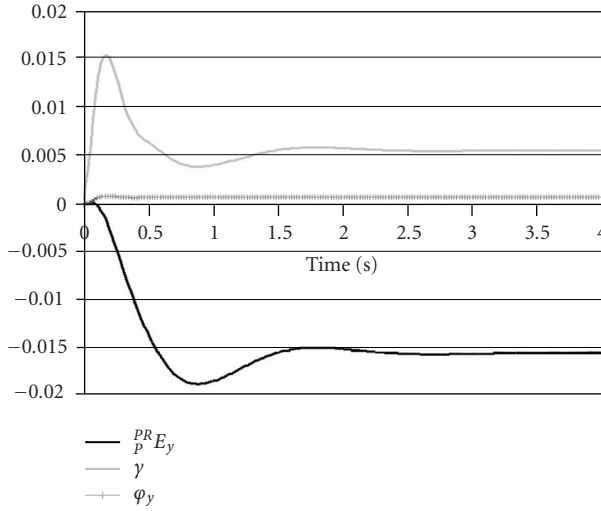


FIGURE 11: Comparison of ${}^O_P E_z$, γ , and φ_z with the control law (8) in the case study B.

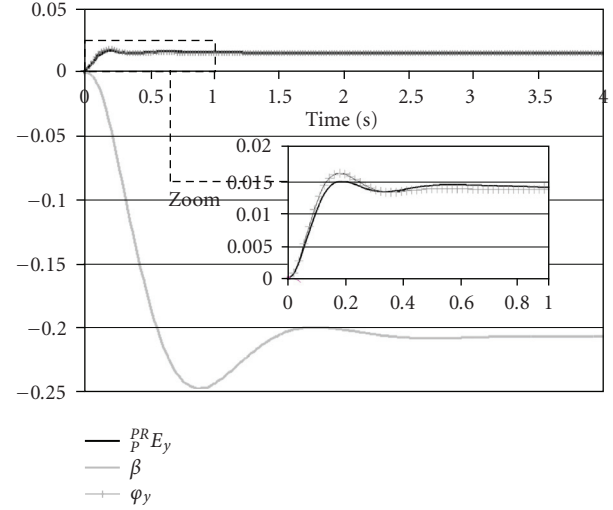


FIGURE 13: Comparison of ${}^P_P E_y$, β , and φ_y with the control law (10) in the case study B.

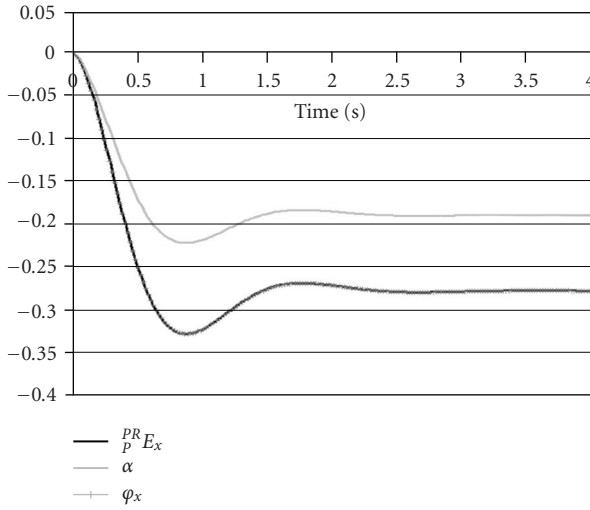


FIGURE 12: Comparison of ${}^P_P E_x$, α , and φ_x with the control law (10) in the case study B.

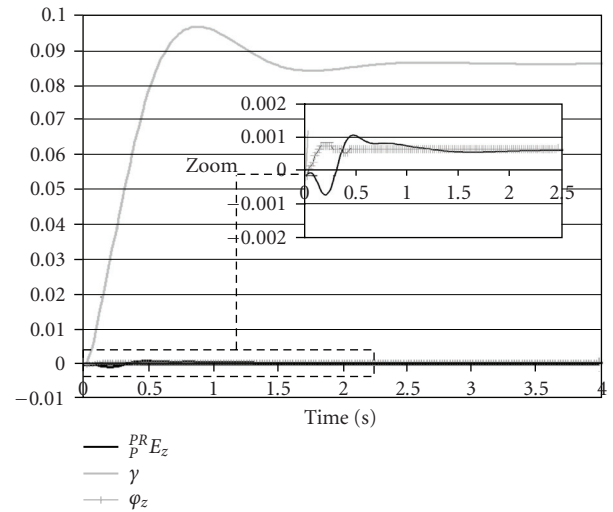


FIGURE 14: Comparison of ${}^P_P E_z$, γ , and φ_z with the control law (10) in the case study B.

order to have large rotations only in one direction and negligible rotations in the other two directions, independently of the direction of the applied moment; the diagonal values of ${}^{PR}C_r$ are obtained by the formula (14) as in the previous case study. The rotational stiffness and damping matrices in the reference frame O can be obtained by the equations (12).

The rotational behaviour of the robot about the three principal directions is compared with three decoupled second-order inertia-rotational spring-rotational damper systems loaded by the components of the external moment ${}^{PR}M = {}^O_P R^O M = [-14.51 \ 13.74 \ 0.769]^T$:

$$\begin{aligned} 3.10\ddot{\varphi}_x + 11.94\dot{\varphi}_x + 50\varphi_x &= -14.51, \\ 3.10\ddot{\varphi}_y + 53.4\dot{\varphi}_y + 1000\varphi_y &= 13.74, \\ 3.10\ddot{\varphi}_z + 53.4\dot{\varphi}_z + 1000\varphi_z &= 0.769. \end{aligned} \quad (19)$$

Figures 9, 10 and 11 show the behaviour of the robot controlled by the law (8), based on the analytical Jacobian matrix, in comparison with the three decoupled systems (19); Figures 12, 13 and 14 show the same comparison, but applying the law (10), based on the geometric Jacobian matrix. In these graphs the end-effector orientation with respect to the principal stiffness and damping reference frame is represented both by the components of the vector ${}^{PR}P E = {}^O_P R^O E$ and by the Euler angles.

It is possible to note that using the control law (8) the rotational behaviour of the robot is remarkably different from the decoupled systems; on the contrary, using the control law (10) the time histories of the three components of the vector ${}^{PR}P E$ are very close to the ones of the three decoupled systems:

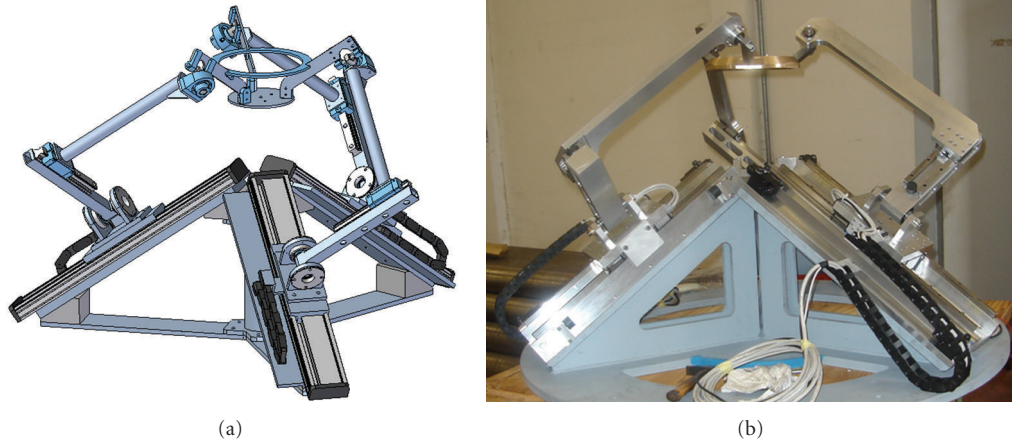


FIGURE 15: 3-CPU parallel robot prototype.

- (i) the relative difference between ${}^P E_x$ and φ_x , after 0.5s, remains lower than 0.15% (Figure 12); this rotation direction is the most significant because it is the one with higher compliance;
- (ii) the relative difference between ${}^P E_y$ and φ_y has a peak of 9.8% at 0.2s (zoom box of Figure 13) but rapidly decreases;
- (iii) the relative difference between ${}^P E_z$ and φ_z is high only in the first second (zoom box of Figure 14).

All the relative differences tend to zero in steady state. These results show that the control law (10) imposes successfully the rotational compliance about the three principal axes, and is capable of effectively constrain the rotation direction; the robot behaviour is almost decoupled in the three rotation directions and similar to a linear three-degree-of-freedom second-order system. Let us note that complete decoupling of the robot dynamic behaviour could be obtained by introducing the model-based compensation of the inertial terms [30], but this increases remarkably the computational burden without significant benefits.

6. Conclusions

The vector $\mathbf{E} = \theta \mathbf{e}$ is the product of the unit vector \mathbf{e} representing the *axis of rotation* and the *angle of rotation* θ , which are the natural invariants of the rotation matrix, independent from the reference frame; this frame-invariant vector has been applied to the impedance control of a three-degree-of-freedom purely rotational parallel robot (3-CPU).

If the Euler angles are used as external coordinates, the kinematics is characterized by the analytical Jacobian matrix \mathbf{J}_A ; on the contrary, using the components of the vector \mathbf{E} as external coordinates leads to the definition of the analytical Jacobian matrix \mathbf{J}_E , which tends to the geometric Jacobian matrix \mathbf{J}_G if θ tends to zero.

This important geometric property has relevant consequences on the behaviour of the resulting impedance control; to show that, the behaviours of the 3-CPU parallel robot

controlled by two different impedance algorithms, based on the Jacobian matrices \mathbf{J}_A and \mathbf{J}_G , have been compared.

The simulation results show that only the geometric Jacobian-based impedance control law allows to impose properly isotropic and nonisotropic end-effector stiffness and damping; moreover, the end-effector rotations along the three principal stiffness/damping directions are almost decoupled and similar to linear second-order systems, without the need of the model-based compensation of the inertial terms, which is computationally heavy.

For all of these reasons, using the components of the vector \mathbf{E} as external coordinates is suitable for all the applications in which a intuitive and decoupled control of the rotational compliance is required; for example, haptic human-machine interfaces for teleoperation of robots and control sticks of real or virtual aircrafts and helicopters; compliant tables for carrying parts in robotized assembly lines.

The dynamic performance of a robot controlled by the proposed algorithm depends on the inertial properties, on the features of the actuators, and on the stiffness and damping matrices; adopting a proper mechanical design in combination with actuators characterized by high force/torque it is possible to impose high values of control stiffness and consequently to perform high frequency motion.

Although the main objective of impedance control is to obtain rotational compliance in one or more directions, high rotational positioning accuracy can be obtained in the remaining directions by imposing high values of the corresponding elements of the stiffness matrix; obviously, in the real implementation the maximum accuracy is limited by the mechanical stiffness and by the accuracy of the sensors.

In the following of the research, the proposed control algorithms will be experimentally tested on the 3-CPU rotational parallel robot prototype shown in Figure 15 [31].

References

- [1] N. H. Raibert and J. J. Craig, "Hybrid position/force control of manipulators," *Journal of Dynamic Systems, Measurement, and Control*, vol. 103, pp. 126–133, 1981.

- [2] N. Hogan, "Impedance control: an approach to manipulation—part I: theory," *Journal of Dynamic Systems, Measurement, and Control*, vol. 107, no. 1, pp. 1–7, 1985.
- [3] N. Hogan, "Impedance control: an approach to manipulation—part II: implementation," *Journal of Dynamic Systems, Measurement, and Control*, vol. 107, no. 1, pp. 1–9, 1985.
- [4] N. Hogan, "Impedance control: an approach to manipulation—part III: applications," *Journal of Dynamic Systems, Measurement and Control, Transactions of the ASME*, vol. 107, no. 1, pp. 17–24, 1985.
- [5] D. E. Whitney, "Historical perspective and state of the art in robot force control," *International Journal of Robotics Research*, vol. 6, no. 1, pp. 3–14, 1987.
- [6] B. Siciliano and L. Villani, *Robot Force Control*, Kluwer Academic Publishers, Dordrecht, The Netherlands, 2000.
- [7] T. Yoshikawa, "Force control of robot manipulators," in *Proceedings of IEEE International Conference on Robotics and Automation*, pp. 220–226, San Francisco, Calif, USA, 2000.
- [8] L. Rey and R. Clavel, "The Delta robot: a position paper," *Annals of CIRP*, vol. 47, pp. 347–351, 1998.
- [9] V. E. Gough and S. G. Whitehall, "Universal tyre test machine," in *Proceedings of the FISITA 9th International Technical Congress*, pp. 117–137, May 1962.
- [10] D. Stewart, "A platform with six degrees of freedom," *Proceedings of the Institution of Mechanical Engineers*, vol. 180, part 1, no. 15, pp. 371–386, 1965.
- [11] K.-E. Neumann, "Robot," US patent no. 4 732 525, 1986.
- [12] J. P. Merlet, "Force-feedback control of parallel manipulators," in *Proceedings of IEEE International Conference on Robotics and Automation*, vol. 3, pp. 1484–1489, Philadelphia, Pa, USA, April 1988.
- [13] S. M. Satya, P. M. Ferriera, and M. W. Spong, "Hybrid control of a planar 3-Dof parallel manipulator for machining operations," *Transaction of the NAMRI/SME*, vol. 23, pp. 273–280, 1995.
- [14] M. Callegari and A. Suardi, "On the force-controlled assembly operations of a new parallel kinematics manipulator," in *Proceedings of IEEE Mediterranean Conference on Control and Automation*, Rhodes, Greece, June 2003, IV06-02.
- [15] F. Caccavale, B. Siciliano, and L. Villani, "The Tricept robot: dynamics and impedance control," *IEEE/ASME Transactions on Mechatronics*, vol. 8, no. 2, pp. 263–268, 2003.
- [16] G. M. Acaccia, L. Bruzzone, M. Callegari, R. C. Michelini, R. M. Molino, and R. P. Razzoli, "Functional assessment of the impedance controller of a parallelly actuated robotic six d.o.f. rig," in *Proceedings of the 6th IEEE Mediterranean Conference on Control and Systems (MCCS '98)*, pp. 397–402, Alghero, Italy, 1998.
- [17] E. D. Fasse and C. M. Gosselin, "On the spatial impedance control of Gough-Stewart platforms," in *Proceedings of IEEE International Conference on Robotics and Automation*, vol. 2, pp. 1749–1754, Leuven, Belgium, 1998.
- [18] E. D. Fasse and C. M. Gosselin, "Spatio-geometric impedance control of Gough-Stewart platforms," *IEEE Transactions on Robotics and Automation*, vol. 15, no. 2, pp. 281–288, 1999.
- [19] F. Caccavale, C. Natale, B. Siciliano, and L. Villani, "Six-DOF impedance control based on angle/axis representations," *IEEE Transactions on Robotics and Automation*, vol. 15, no. 2, pp. 289–300, 1999.
- [20] J. Angeles, *Rational Kinematics*, Springer, New York, NY, USA, 1988.
- [21] J. M. Selig, *Geometric Fundamentals of Robotics*, Springer, New York, NY, USA, 2005.
- [22] F. Caccavale, B. Siciliano, and L. Villani, "The role of Euler parameters in robot control," *Asian Journal of Control*, vol. 1, no. 1, pp. 25–34, 1999.
- [23] S. Chiaverini and B. Siciliano, "The unit quaternion: a useful tool for inverse kinematics of robot manipulators," *Systems Analysis, Modelling Simulation*, vol. 35, no. 1, pp. 45–60, 1999.
- [24] I. A. Bonev and J. Ryu, "A new approach to orientation workspace analysis of 6-DOF parallel manipulators," *Mechanism and Machine Theory*, vol. 36, no. 1, pp. 15–28, 2001.
- [25] R. L. Hollis, S. E. Salcudean, and A. P. Allan, "A six-degree-of-freedom magnetically levitated variable compliance fine-motion wrist: design, modeling, and control," *IEEE Transactions on Robotics and Automation*, vol. 7, no. 3, pp. 320–332, 1991.
- [26] L. E. Bruzzone and R. M. Molino, "A geometric definition of rotational stiffness and damping applied to impedance control of parallel robots," *International Journal of Robotics and Automation*, vol. 21, no. 3, pp. 197–205, 2006.
- [27] M. Callegari, P. Marzetti, and B. Olivieri, "Kinematics of a parallel mechanism for the generation of spherical motions," in *On Advances in Robot Kinematics*, J. Lenarcic and C. Galletti, Eds., pp. 449–458, Kluwer Academic Publishers, Dordrecht, The Netherlands, 2004.
- [28] T. Valency and M. Zacksenhouse, "Accuracy/robustness dilemma in impedance control," *Journal of Dynamic Systems, Measurement and Control*, vol. 125, no. 3, pp. 310–319, 2003.
- [29] F. Caccavale, B. Siciliano, and L. Villani, "Robot impedance control with nondiagonal stiffness," *IEEE Transactions on Automatic Control*, vol. 44, no. 10, pp. 1943–1946, 1999.
- [30] M. Callegari and P. Marzetti, "Inverse dynamics model of a parallel orienting device," in *Proceedings of the 8th International IFAC Symposium on Robot Control (SYROCO '06)*, Bologna, Italy, September 2006.
- [31] M. Callegari, "Design and prototyping of a SPM based on 3-CPU kinematics," in *Parallel Manipulators, New Developments*, A. Lazinic, Ed., pp. 171–198, ARS, Vienna, Austria, April 2008.